Millimeter-Wave and Terahertz Imaging Techniques

Author

Enrique Nova Lavado

Thesis Advisor

Jordi Romeu Robert

AntennaLab
Universitat Politècnica de Catalunya
Departament de Teoria del Senyal i Comunicacions

Submitted to the Universitat Politècnica de Catalunya (UPC) in partial
fulfillment of the requirements for the degree of

DOCTOR OF PHILOSOPHY

April 26, 2013

Acta de qualificació de tesi doctoral

Curs acadèmic:

Nom i cognoms

Programa de doctorat

Unitat estructural responsable del programa

Resolució del Tribunal

Reunit el Tribunal designat a l'efecte, el doctorand / la doctoranda exposa el tema de la seva tesi doctoral titulada

_____

_____.

Acabada la lectura i després de donar resposta a les qüestions formulades pels membres titulars del tribunal, aquest atorga la qualificació:

☐ APTA/E   ☐ NO APTA/E

(Nom, cognoms i signatura)		(Nom, cognoms i signatura)	
President/a		Secretari/ària	
(Nom, cognoms i signatura)	(Nom, cognoms i signatura)		(Nom, cognoms i signatura)
Vocal	Vocal		Vocal

_____, _____ d'/de _____ de _____

El resultat de l'escrutini dels vots emesos pels membres titulars del tribunal, efectuat per l'Escola de Doctorat, a instància de la Comissió de Doctorat de la UPC, atorga la MENCIÓ CUM LAUDE:

☐ SÍ   ☐ NO

(Nom, cognoms i signatura)	(Nom, cognoms i signatura)
Presidenta de la Comissió de Doctorat	Secretària de la Comissió de Doctorat

Barcelona, _____ d'/de _____ de _____

Dedicatoria

Abstract

This thesis presents the development and assessment of imaging techniques in the millimeter-wave (mmW) and terahertz frequency bands. In the first part of the thesis, the development of a $94\,\mathrm{GHz}$ passive screener based on a total-power radiometer (TPR) with mechanical beam-scanning is presented. Several images have been acquired with the TPR screener demonstrator, either in indoor and outdoor environments, serving as a testbed to acquire the know-how required to perform the research presented in the following parts of the thesis.

In the second part of the thesis, a theoretical research on the performance of near-field passive screeners is described. This part stands out the tradeoff between spatial and radiometric resolutions taking into account the image distortion produced by placing the scenario in the near-field range of the radiometer array. In addition, the impact of the decorrelation effect in the image has been also studied simulating the reconstruction technique of a synthetic aperture radiometer. Guidelines to choose the proper radiometer depending on the application, the scenario, the acquisition speed and the tolerated image distortion are given in this part.

In the third part of the thesis, the development of a correlation technique with optical processing applicable to millimeter-wave interferometric radiometers is described. The technique is capable of correlating wide-bandwidth signals in the optical domain with no loss of radiometric sensitivity. The theoretical development of the method as well as measurements validating the suitability to correlate radiometric signals are presented in this part.

In the final part of the thesis, the frequency band of the imaging problem is increased to frequencies beyond $100\,\mathrm{GHz}$, covering the THz band. In this case the research is centered in tomographic techniques that include spectral information of the samples in the reconstructed images. The tomographic algorithm can provide detection and identification of chemical compounds that present a certain spectral footprint in the THz frequency band.

Keywords: Aperture Synthesis, Optical Modulation, Passive Interferometry, W-band Radiometry, Near-Field Imaging, Radiometric Sensitivity, Passive Screeners, Terahertz Tomography, Terahertz Spectroscopy, Diffraction Tomography.

Contents

Close-Range Millimeter-Wave Passive Systems

Terahertz Imaging

Thesis Conclusions

Introduction

THE aim of this chapter is to introduce the context, the scope, the objectives and the structure of the research presented in this document. The first section is devoted to describe the framework in which the thesis has been developed: the TeraSense project. The second section contextualizes the research performed in this thesis by showing the current state of the art of the studied topics. The state of the art is followed by enumerating the objectives and the scope of this thesis. Finally the structure and organization of the work is described.

1.1 TeraSense project

The research presented in this thesis is part of an initiative to promote the development of the Terahertz technologies in Spain with the coordination of the Polytechnic University of Catalonia (UPC). This initiative is concentrated in the TeraSense project where 16 research groups of 11 Spanish universities work together to improve the knowledge related with Terahertz systems. The research groups participating in the project are specialized in electrodynamics, high frequency technology and design, numerical simulation and computer engineering. The diversity of expertise found in the research groups has been an advantage to face the scientific challenges that appear in the THz frequency range. The main objectives and ambitions of the project are:

1. To improve the existing knowledge on the interaction between the matter and the THz waves.

2. To build a terahertz laboratory infrastructure distributed among the different groups participating in the project.

3. To establish a joint international graduated program on THz electromagnetic sensing able to attract bright students from worldwide.

Figure 1.1: TeraSense project logo.

4. To coordinate a joint public-private effort at national level and improve the presence and projection of the Spanish technology at international levels.

5. To develop a real-time two-dimensional close-range camera for security applications working at W-band.

6. To develop a remote sensor radar system working at 300 GHz able to perform atmospheric and environmental scanning.

7. To develop a near-field scanner for imaging and sensing of bio-structures and pharmacology working from 0.5 THz to 2 THz.

The research described in this thesis is linked with objectives 5 and 7 of the TeraSense project. The first part of this document is devoted to the study of passive close-range Millimeter-Wave (mmW) imaging systems whereas the second part explains the research on THz tomographic imaging of pharmacological compounds, being both parts related with objectives 5 and 7 respectively.

1.2 State of the art

This section will place the work described in this thesis into the current research context in the areas of mmW and THz systems with special focus on W-band passive imaging and THz tomography.

1.2.1 Millimeter-wave technology and applications

The mmW frequency range is comprised from 30 GHz to 300 GHz. In such wide range, the applications and technologies that are found in the lower frequencies can be considerably different from the ones working close to 300 GHz. Figure 1.2 presents an schematic showing the distribution of the electromagnetic spectrum and some applications. As shown in the figure, the most significant commercial applications in the mmW range are the automotive radar and the Wireless Personal Area Network (WPAN) (standard IEEE 802.15.3c).

The application areas found in the mmW range are communications, active remote sensing and passive remote sensing. The technology and current research in each area is summarized in the following points:
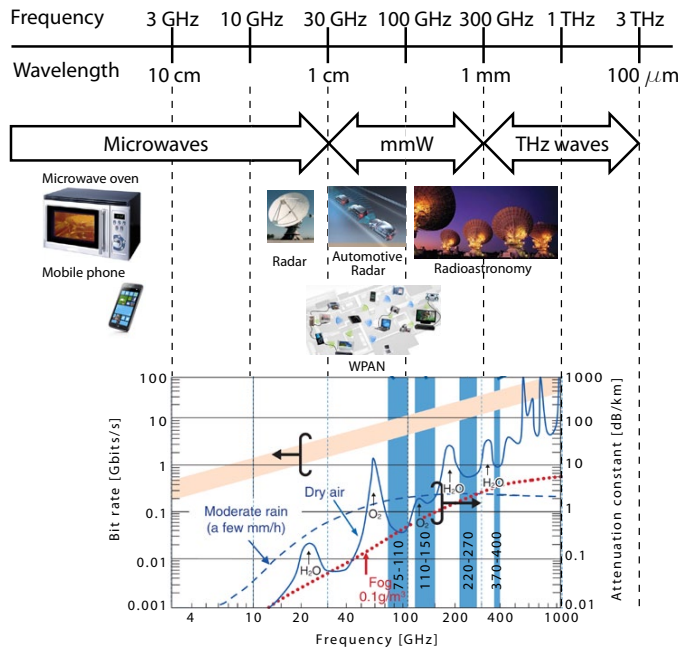
Figure 1.2: Schematic with the distribution of the electromagnetic spectrum depicting the main applications in each frequency range. The atmospheric attenuation level is also shown pointing out the available atmospheric windows.

- **mmW communications:** On the one hand, the $60\,\mathrm{GHz}$ mmW WPAN (IEEE 820.15.3c) is being developed to provide medium and short range wireless communications with a sort of advantages if compared with Bluetooth WPAN (IEEE 802.15.1) [1]. The spectrum of the $60\,\mathrm{GHz}$ WPAN is allocated from $57 - 66\,\mathrm{GHz}$ (in Europe) allowing a huge spectral capacity of the link. In addition, the $60\,\mathrm{GHz}$ presents higher atmospheric attenuation than the lower microwave frequencies due to an oxygen (O_2) absorption line placed at around $60\,\mathrm{GHz}$ [2]. The high path loss can be seen as an advantage for WPAN links since the interference between different systems or collocated networks is reduced. Moreover, the frequency reuse capabilities and the spatial efficiency are improved. An additional advantage is based on the size of the transceiver electronics. As the frequency is increased the size of the transceiver components can be reduced. Hence, the size of mobile or portable devices using $60\,\mathrm{GHz}$ WPAN can be shrunk. The current research is divided in three main aspects: 1) the channel analysis and modeling; 2) the modulation scheme; 3) the broadband circuit technologies and 4) the reconfigurability of the antennas.

  On the other hand, the Japanese government in collaboration with Nippon Telegraph and Telephone Corporation (NTT) has developed the technology to transmit uncompressed High Definition Television (HDTV) video through a wireless link with a central frequency of $120\,\mathrm{GHz}$. The link is capable of transmitting up to $10\,\mathrm{Gbits/s}$ and is expected to be used in the last mile of 10 Gigabit Ethernet as well as for multiplexed transmission of up to six channels of uncompressed HDTV video. In order to achieve

such large bandwidth, NTT has developed technology to convert an optical subcarrier data signal produced by photonics technology into electronic signals and radio waves using Uni-travelling Carrier Photodiode (UTC-PD) [3, 4]. It provides the photonics features such as wide bandwidth, good stability and ultrahigh frequency to generate electromagnetic waves in the mmW range. Current research has been performed using Amplitude Shift Keying (ASK) modulations, however it is expected that data rates up to $20\,\mathrm{Gbits/s}$ can be achieve if most sophisticated modulations schemes such as 16-state Quadrature Amplitude Modulation (16QAM) are used.

- **Active remote sensing:** The main application in the area of active remote sensing at mmW frequencies is the automotive radar sensor [5, 6]. The radar is used as a driver assistant for various functions such as adaptive cruise control, automatic emergency braking and parking aid. The first generation of automotive radar sensors working at $77\,\mathrm{GHz}$ was introduced in 1998 by Daimler. Since then, several new generations of sensors have appeared from a number of manufacturers all relying on the Frequency-Modulated Continuous-Wave (FMCW) modulation technique. In Europe a total of $4\,\mathrm{GHz}$ are available for this purpose from $77\,\mathrm{GHz}$ to $81\,\mathrm{GHz}$ allowing a range resolution of $10\,\mathrm{cm}$. The technology used to build the radar is usually based on Monolithic Microwave Integrated Circuit (MMIC) using GaAs semiconductor. Recently, implementations using $90\,\mathrm{nm}$ and $60\,\mathrm{nm}$ Complementary Metal-Oxide-Semiconductor (CMOS) technologies have been published [7].

Taking advantage of the wide bandwidth available for radar purposes in the mmW frequency region, other applications using radar techniques have appeared. As an example, in [8] a three-dimensional holographic imaging technique is shown to perform personnel screening for concealed weapon detection purposes. In [C7], an interferometric system is shown capable of detecting surface deformations on the order of tens of micrometers. Additionally, the W-band atmospheric window has been widely used to perform active remote sensing of the atmospheric properties such as the cloud formation and composition [9] [10].

- **Passive remote sensing:** Radioastronomy is the application concentrating the main efforts of the scientific community in the area of passive remote sensing. This effort is translated in examples like the Atacama Large Millimeter/Submillimeter Array (ALMA) international telescope [11]. It is situated on a dry place at $5000\,\mathrm{m}$ of elevation, allowing an excellent atmospheric transmission over the instrument frequency range from $30\,\mathrm{GHz}$ to $1\,\mathrm{THz}$. The radio telescope consists of two antenna arrays: one of 64 antennas with $12\,\mathrm{m}$ diameter each being reconfigurable in multiple patterns ranging from $150\,\mathrm{m}$ to $15\,\mathrm{km}$; and a second array consisting of a set of 4 antennas with $12\,\mathrm{m}$ diameter and 12 antennas with $7\,\mathrm{m}$ diameter working in packed configurations of $50\,\mathrm{m}$ diameter [12]. ALMA will provide total power and interferometric information on molecular, atomic, ionized gas and dust in the solar system.

A second example of a mmW instrument developed by the radioastronomy community the Planck radio telescope [13]. This instrument was launched in 2009 together with the Herschel radio telescope. Planck covers a frequency range from $30\,\mathrm{GHz}$ to $857\,\mathrm{GHz}$ and its objective is to map the entire sky by strip scanning with a spin rate of $1\,\mathrm{rpm}$.

The mmW frequency range is also used to retrieve environmental parameters such as

Figure 1.3: Artist view of a passive scanner portal that is capable to detect objects concealed beneath the clothes. The working principle of this portal is to distribute in a vertical disposition a group of horizontal passive arrays in such a way that a 2D image is obtained.

temperature, humidity and liquid water of the soil. In [14], total-power measurements at mmW are used to retrieve the aforementioned parameters. Additionally, passive remote sensing combined with image formation techniques is applied to solve several security issues: aircraft landing and guidance; low-visibility navigation and situational awareness; reconnaissance and surveillance; search and rescue and drug interdiction among others. An example can be found in a W-band radiometric imager that helps in the landing process of an helicopter. It provides real time imaging through the dust cloud when the helicopter is landing, thus reducing the probability of accident [15]. An additional application of the passive imaging is the personnel screening for concealed object detection. This application concentrates the research on mmW passive imaging presented in this thesis. The research undergoing in this area is described in the following section.

1.2.2 Millimeter-wave passive imaging for personnel screening

Several companies have developed proprietary systems for concealed threat detection. These systems are designed either in a walkthrough portal configuration as the one shown in Fig. 1.3 or for stand-off operation. Portal systems are usually designed to detect small threats at short distances ($< 3\,\text{m}$), achieving spatial resolutions around $1\,\text{cm}$ whereas stand-off systems are conceived for larger distances and larger threads. There are three different operating frequency ranges in use for personnel screening purposes: 1) 25 to $35\,\text{GHz}$; 2) $94\,\text{GHz}$; and 3) 200 to $300\,\text{GHz}$. Each corresponds to one of the windows that exist in atmospheric propa-

(a) ThruVision T4000 passive scanning system

(b) Brijot MobileScanPS passive scanning system
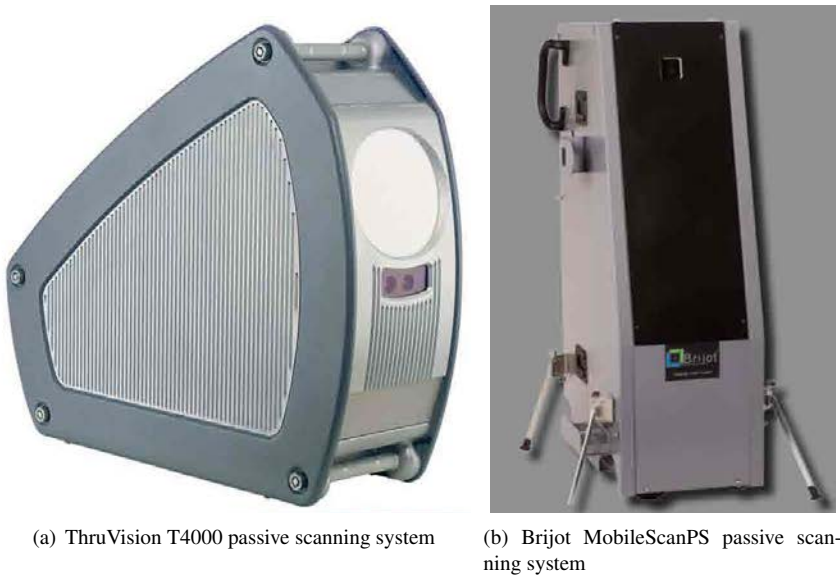
Figure 1.4: Two examples of commercial passive scanning systems.

gation. Atmospheric absorption is not a significant issue for the relatively modest distances used in people-screening applications, nevertheless by working in the same frequency ranges as some of the longer distance applications it is possible to benefit from more readily available and lower cost components. At the lower frequencies, equipment needs to be relatively large, or resolution is sacrificed. Higher frequencies enable more compact systems such as those developed by ThruVision [16]. Also, specially for passive systems, it is easier to detect dielectric threat materials at higher frequencies since their higher refractive indices at these frequencies makes them appear more metal-like and reflective. Another compact system, operating at $94\,\mathrm{GHz}$ for modest stand-off distances has been developed by Brijot. Figure 1.4 shows two photographs of the systems commented in this paragraph.

A number of different scanning systems are in use with mechanical, electronic and hybrid configurations. The Smiths Detection system uses a pair of spinning tilted mirrors to scan in the x-axis and a third mirror to raster scan in the y-axis on to the detectors. The Qinetiq [17] system uses a different arrangement with a single rotating mirror to produce a conical scan on to a complete line array. It also exploits polarizers and a quarter-wave plate to enable a folded optic reducing the dimensions of the scanning system.

The Trex Sago [18] approach is to create an azimuthal line scan through a frequency dependent coupling into an antenna. In the ST150, the second axis is provided by panning the main reflecting mirror. In their real-time imager, a phased array of some 230 receivers is deployed. The L-3 SafeView [19] system is an active system based on developments from PNNL using a holographic reconstruction from a fan-beam source and line array of detector antennas which rotate around the subject being scanned. This system measures both amplitude and phase of the reflected signal for use in the FFT-based holographic image reconstruction.

A novel approach has been developed by Agilent [20] and demonstrated in prototype form. This employs a confocal arrangement of a single source and detector. The source is reflected from a configurable mirror made up of a 2-dimensional array of several thousand dipole reflectors. Each dipole is connected to a large, fast switching array which can place either a short or open circuit at the feed point of each dipole. This forms a programmable, reflecting Fresnel zone plate which can be used to focus the millimeter wave source and detector onto a chosen point in space in front of the mirror. The antennas can be switched so as to scan over 10^7 pixels per second, leading to a solid state imaging system with a 15 Hz refresh rate or higher. Although the frequency employed is relatively low, 24 GHz in the prototype system, the programmable mirror is only a few centimeter thick, leading to relatively compact system.

Development directions in mmW systems focus largely on methods to reduce the cost of systems, without sacrificing neither sensitivity nor resolution. Since most of these systems use a number of detectors in order to be able to capture moving images, the cost of multiple receivers dominates the total cost of the system.

1.2.3   Terahertz systems and applications

The THz frequency range is comprised between 300 GHz and 3 THz as shown in Fig. 1.2, placed between the Radiofrequency (RF) spectrum and the infrared and optical spectrum. Either photonic or electronic techniques are used to generate THz electromagnetic waves depending on the type application.

There are mainly 4 ways of generating radiation in the THz range:

- In order to generate a local oscillator for a THz transceiver in the range between 300 GHz and 1 THz usually electronic techniques are used. In this case, a mmW phase-locked oscillator is upconverted to the desired frequency by a multiplier chain [21].

- If a broadband pulsed radiation is required (e.g to perform spectroscopy) usually a Photoconductive Antenna (PCA) is used [22]. By exciting the PCA using a femtosecond laser pulse, a broadband THz pulse radiation is emitted [23]. The duration and therefore the spectral content of the emitted pulse depends basically on the duration of the laser pulse and on the relaxation-time of the photocarriers created by the laser pulse on the antenna semiconductor.

- To generate a Continuous Wave (CW) signal beyond 1 THz usually a Photoconductive Switch (PCS) is used [24, 25]. The signals coming from two lasers are mixed in the PCS, giving an output frequency equal to the frequency difference between both lasers. This technique usually gives a power with a order of magnitude lower than the electronic generation, however it is suitable for higher frequencies.

- If a CW high-power source (around 30 mW) is required, the solution is given by a Quantum Cascaded Laser (QCL) [26, 27]. This laser is a semiconductor device where the light emission is obtained through intersubband transitions in the quantum wells. This allows to radiate at lower frequencies than a typical optical laser. However the output frequency range is restricted to frequencies greater than 1.5 THz.

Depending on the power requirements, the frequency and the application one among the aforementioned THz generation techniques should be chosen. The applications in the THz range can be distributed in the following areas: 1) Communications; 2) Remote sensing; 3) Spectroscopy and 4) Imaging

- **Terahertz communications:** The THz frequency range is very attractive for communications due to the huge available bandwidth [28]. However, the signal path loss is a disadvantage. Figure 1.2 shows that atmospheric attenuation increases drastically beyond 100 GHz. Therefore, the research is focused on short-range Wireless Local Area Network (WLAN) and WPAN systems applied to wireless displays, HDTV distribution, backhaul traffic, etc. In addition, THz communications may interfere with the classical application of this frequency band: the radioastronomy [29]. This issue has been recently investigated and is concluded that the transmitter should be kept 55 km away from any radio telescope. Nevertheless, the research is still in an initial stage, and no relevant transceiver demonstrators working beyond 300 GHz have been published.

- **Active and passive remote sensing:** As in the mmW frequency range, the main application for passive remote sensing in the THz range is the radioastronomy. An example is the Herschel radio telescope launched to the space in 2009 [30, 31]. The HIFI instrument carried by Herschel can retrieve a total power information of the sky in two polarizations over seven frequency bands between 480 GHz and 1.91 THz. Herschel has a cassegrain reflector antenna system with a main reflector of 3.5 m diameter and the instruments are cooled down to 80 K. The measurements are used by the scientific community to discern the weak signals from distant galaxies and to resolve among multiple forming stars and galactic clouds.

  On the other hand, the THz range is not widely used in passive remote sensing for security applications since the sensitivity of the available receivers beyond 300 GHz does not allow the acquisition of images in real-time. In order to improve the acquisition time, active approaches have been developed. An example is a FMCW radar developed by the Jet Propulsion Laboratory (JPL) of the National Aeronautics and Space Administration (NASA) [32] [33]. The system can acquire three-dimensional images at a standoff distances of 25 m in five seconds operating at 675 GHz. It relies on a 1 m diameter ellipsoidal main reflector to achieve an spatial resolution of around a centimeter at 25 m range.

- **Spectroscopy:** Many materials presents vibrational or rotational modes at molecular level in the THz frequency range. This is translated in an absorption of the electromagnetic energy at the resonance frequency. In order to measure absorption frequencies, a broadband THz emission is produced and directed to the material. The absorption spectra of the received signal is analyzed to find absorption peaks. An absorption spectrum can completely characterize a material, therefore a certain material can be detected and its concentration can be calculated from an spectroscopic analysis [34, 35].

  The most extended THz spectroscopy system is the Terahertz Time-Domain Spectroscopy (THz-TDS). It relies on PCA to emit and receive the THz radiation and a femtosecond laser is used to excite the PCA. The amplitude and phase of the emitted pulse can be measured by sampling the THz pulse by using a delay stage that controls
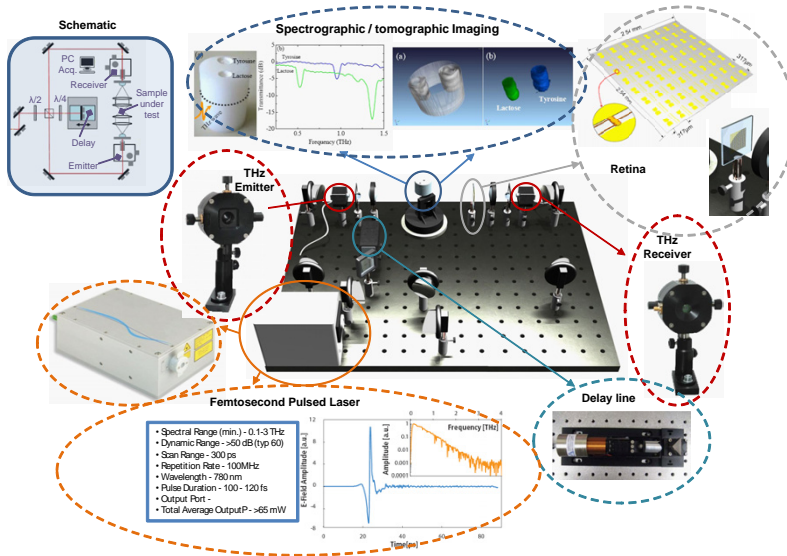
Figure 1.5: Schematics of a THz-TDS system with accessories to perform tomographic imaging (e.g. a rotor used to rotate the sample and a retina used to multiplex multiple points of view without necessity of mechanical movements). The main parts that intervene in the emission and reception of the THz pulse are depicted.

the delay of the laser pulse. With this measurement system, the refractive index and the absorption coefficient of the material sample can be retrieved.

- **Imaging:** Recently, a real-time CMOS camera has been published [36] [37] [38]. It consists on a $1\,$kPixel THz detector fully integrated in a $65\,$nm CMOS technology and it is capable of capture real-time video with up to $500\,$fps. The design achieves a bandwidth from $790\,$GHz to $960\,$GHz. This camera presents a great advance in the THz technology since it represents a cheap, compact and reliable instrument to acquire images in the THz range.

  Terahertz microscopy is also being developed and has been already applied to image semiconductor devices achieving down to $150\,$nm of spatial resolution [39]. The technique is based on capturing the near-field reflected by the sample using a very thin field probe. In this case the diffraction effect does not limit the resolution since the electromagnetic field has not been propagated, and therefore it has not lost information that limits the resolution in typical imaging.

  Additionally, THz imaging techniques are being developed to perform 3-dimensional imaging of biological, pharmaceutical and alimentary samples [40, 41]. The imaging information can be combined with the spectroscopic information to detect different materials dispersed over a sample. The following section describes in detail the current research on THz tomography.

1.2.4   Terahertz spectroscopy and tomography

Terahertz tomography refers to imaging by sections through the use of THz electromagnetic waves. Two main classifications of tomographic techniques are found in the literature: the diffractive techniques [42] and the non-diffractive techniques [43].

The diffractive techniques are based on illuminating the sample with an electromagnetic wave and measure the scattered field. From the measured information the currents that have been excited on the sample by the emitted field can be reconstructed, and thus the shape of the sample can be retrieved. The expressions that govern this method emanate from the Maxwell equations and cannot be solved analytically. In order to solve the expression for the scattered field, an approximation should be used. There are mainly two approximations to solve the problem: the Born approximation [44] and the Rytov approximation [45].

The Born approximation was introduced by Max Born in 1925. If the scattered field is much smaller compared with the incident field, the scattered field can be expressed by its first order approximation. The Born approximation can be applied if $d\Delta n < \frac{\lambda}{4}$ where d is the target size and Δn is the index of refraction difference between the air and the sample. From this approximation, one can observe that the approximation can be applied when the wavelength is several times the size of the object. Hence, in the THz frequency range the use of this approximation is unusual since the wavelength is usually smaller than the object.

The Rytov approximation assumes that the incident field is perturbed by the sample only by introducing a phase shift along its propagation path. This approximation is considered more accurate than the Born approximation and it should provide a better estimate of the scattered wave. In addition, the approximation condition is less restrictive than the condition in the Born approximation and it just requires a slow variation of the refraction index of the sample over a wavelength. Additionally, Rytov approximation also has a better behavior when the measuring wavelength is longer than the sample.

There are not many research publications using the aforementioned algorithms in the THz range since usually the conditions are not fulfilled and the resulting images do not reconstruct the shapes of the sample. The reconstruction algorithm commonly used in THz tomography is a non-diffractive method inspired from the x-ray: Computed Tomography (CT). The attenuation produced in the incident field by the object can be described by a line integral of the object function along its path called Radon transformation

$$P(\theta, t) = \int_{L(\theta,t)} f(x,y)dl = \Re(f(x,y)), \qquad (1.1)$$

where $P(\theta, t)$ is the attenuation function of the incident ray along the path l, and t is the ray minimum distance from the sample origin. The attenuation function can be measured by rotating the the object along θ and by sweeping the position of the ray along a line in order to obtain multiple samples on t. Hence, $f(x,y)$ can be retrieved by applying the reverse Radon transformation to the measurements. In practice, a THz beam cannot be treated as a ray line as in in the x-ray CT. Therefore special attention should be taken to create a measurement environment where the assumptions of CT are still valid. The beam should be focused in the sample by using either lenses of parabolic mirrors. The resolution of the image cannot be better than the waist of the beam synthesized by the focusing element. Moreover, the sample
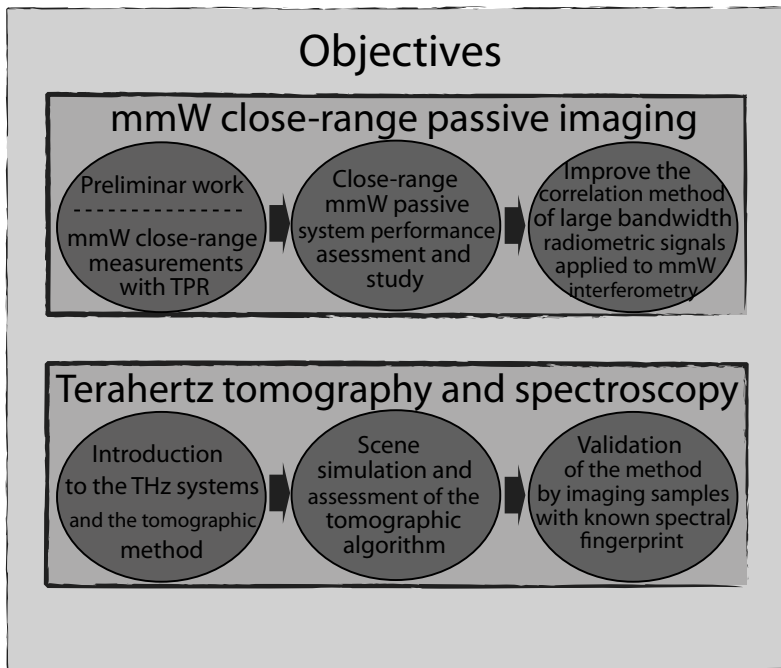
Figure 1.6: Diagram showing the main objectives of both the mmW and THz parts of this thesis.

should be small enough to fit in the focus depth of the beam, otherwise the size of the beam will vary along the sample and the assumption of rays is not further valid.

The spectroscopic information appears directly in the reconstructed result by using all the aforementioned methods [46, 47]. By using a THz-TDS system to measure the multiple point of views, the full spectral information of the sample is obtained. Therefore, the reconstructed image can reveal the different materials contained in the sample analyzing the spectrum. Figure 1.5 shows a THz-TDS system with the main components (e.g. femtosecond laser, two PCA, delay stage,...). This system is used, among other applications, to perform tomography of small samples. The dynamic range is around $65\,\mathrm{dB}$ in present commercial systems and its main advantage is that it can measure the complete THz spectral range at real time.

1.3 Objectives and scope of the thesis

At the beginning of the research work in this thesis, the state of the art for the two main topics described above were analyzed to identify lacks or deficiencies. From the conclusions on the literature survey, the objectives stated in this section were chosen. A main division of the objectives has been done between the objectives that appear in this thesis and the ones that have been considered out of the scope. In addition, the objectives have been sub-divided in two lists, the first related with mmW passive imaging and the second related with THz imaging. Each objective is related with its corresponding paper contribution either in a conference [Ci] or in a journal [Ji].

1.3.1   Objectives appearing in this document

A summary of the objectives appearing in this document is presented in Fig. 1.6 depicting the timeline distribution among the objectives.

- **Millimeter-wave passive imaging**

    - **Passive imaging introduction and imaging:** A simple demonstrator is built to test the passive imaging capabilities in indoor and outdoor conditions [C6, C8, C12].

    - **Close-range passive imaging performance analysis:** A complete theoretical comparison including simulations of the close-range behavior of three radiometers in order to detect optimum configurations that can achieve better performance with lower overall cost [J2].

    - **Correlation method for large bandwidth radiometric signals:** An optical correlation method is applied for correlating large bandwidth radiometric signals coming from mmW interferometric radiometers [C3, C4] [J1].

- **THz spectroscopy and tomography**

    - **Diffractive spectroscopic tomography:** A tomographic algorithm based on the Born approximation is applied to retrieve spectroscopic images. The spectral information of each pixel can be obtained to identify different compound types in the same image. Most of the THz tomographic systems use CT methods to retrieve the image and the diffractive techniques are not studied in deep in the literature [C1].

1.3.2   Objectives excluded from this document

- **mmW systems and components:**

    - **Assessment of THz active Mills-Cross imaging:** By placing two W-band headers from a Vectorial Network Analyzer (VNA) into two linear stages an active Mills-Cross setup is built. Measurements are obtained to assess the suitability of this imaging geometry in the mmW range. [C14–C16].

    - **Radiation pattern characterization of a mmW Cassegrain reflector:** The radiation pattern of a Cassegrain has been characterized from near-field measurements. In addition, the return loss parameter has been adjusted by using a matching section formed by adjustable screws [C2].

- **THz imaging:**

    - **Terahertz subsurface imaging system:** By using a portable THz-TDS system, subsurface images of a ceramic sample are obtained with resolutions around $0.3\,\mathrm{mm}$ [C13].

1.4   Organization of the document

This document has been divided in 4 main parts: 1) the introduction; 2) the research on mmW passive systems; 3) the research on THz tomographic imaging techniques; and 4) conclusions and further discussion. The second part is sub-divided in three chapters whereas the third part is concentrated in one chapter. Each chapter has an introduction or abstract at the beginning followed by a description of the general concepts required to understand the core of the chapter. Measurement or simulation results are found at the end of the chapter and are used to validate the theoretical approach of the problem developed in the core of chapter. At the end of each chapter, with exception of the present one, the conclusions of the obtained results are written.

The second part, Close-range Millimeter-wave Passive Imaging, is devoted to describe the advances achieved in the field of the mmW radiometry. The second chapter includes a total power and interferometric radiometry introduction. Furthermore, it includes a complete design of a total power radiometer used to study the behavior of the mmW components as a previous step to design the interferometric radiometer shown in the third chapter. Indoor and outdoor close-range measurements of persons with concealed objects are shown to study the detection capabilities of the system. The third chapter describes a theoretical study and comparison of three types of screeners and their behavior in close-range imaging: the Real-Aperture (RA) radiometer, the One-Dimensional Synthetic Aperture (1D-SA) and the Two-Dimensional Synthetic Aperture (2D-SA). The fourth chapter and the last one of the second part of this thesis is devoted to describe a method developed to correlate radiometric signals in the optical domain. Measurements of the system are shown validating the suitability of the method for passive mmW interferometric imaging.

The third part, Terahertz Imaging and Spectroscopy, is devoted to describe the tomographic and spectroscopic imaging research performed in this thesis. The fifth chapter, introduces the terahertz imaging basic concepts, presents simulations of the method that is applied and finally show measurements validating the method.

The last part concludes the document and presents further discussion on the achievements of this thesis.

Close-Range Millimeter-Wave Passive Systems

Millimeter-wave radiometric imaging

I<small>N</small> the first part of this chapter the Millimeter-Wave (mmW) radiometry fundamental concepts are described as an introduction for Chapters 3 and 4, paying special attention to the Synthetic Aperture (SA) interferometric radiometry. In the second part of this chapter, design and assembling details of a Total-Power Radiometer (TPR) are explained with the aim of introducing the mmW radiometry from a practical approach. The development of a TPR has been convenient to explore the particularities of mmW components and to acquire the experience to perform the practical work shown in Chapter 4. In addition, several radiometric images obtained with the TPR in different environments are shown, providing examples of concealed object detection capabilities of mmW radiometry.

2.1 Millimeter-wave radiometry

Radiometry is defined as the science devoted to measure the electromagnetic thermal radiation emitted by an object having a temperature higher than $0\,\mathrm{K}$. It was originally developed by the astronomy community to measure the natural radiation produced by cosmic bodies. In the microwave frequency range, an example of radiometric application is the sensing of physical parameters of the Earth such as ocean water salinity levels and soil moisture [48], where the geophysical parameters are related with the levels of thermal emission. At mmW frequencies, the passive close-range imaging for concealed object detection has been developed during the last decade, providing images related with the temperature contrast among bodies in the imaged scene. The latter application is the research focus in the following chapters, therefore this section gives a basic introduction of the main concepts that govern the radiometric science with special emphasis in the behavior at the mmW frequency range.
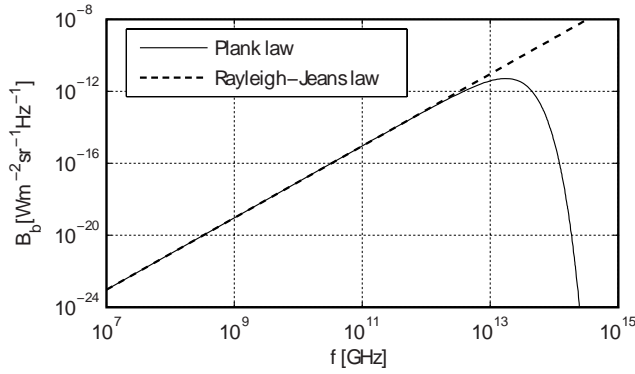
Figure 2.1: Spectral brightness B_b of a black-body with a physical temperature $T_{ph} = 300\,K$ calculated using the Planck's law (2.1) and the Rayleigh-Jeans approximation (2.2).

2.1.1 Thermal radiation and Plank's law

In order to describe the parameters that quantify the thermal radiation of an object, first the concept of black-body should be introduced. It consists of an ideal physical body that, in thermodynamic equilibrium, absorbs all incident energy and re-emits all absorbed energy. The spectral brightness B_b (the radiated power density per unit solid angle, per unit area and per Hertz) of a black-body at a physical temperature T_{ph} is quantified by the Plank's law

$$B_b = \frac{2hf^3}{c^2} \frac{1}{e^{\frac{hf}{k_B T_{ph}}} - 1} \quad [\mathrm{Wm^{-2}sr^{-1}Hz^{-1}}], \tag{2.1}$$

where h is the Planck's constant, k_B is the Boltzmann constant, f is the radiation frequency and c is the speed of light. The exponential function appearing in the Planck's law can be approximated by the first order Taylor polynomial if $f \ll \frac{k_B}{h}T_{ph}$. The resulting expression is the Rayleigh-Jeans law

$$B_b = \frac{2k_B f^2}{c^2} T_{ph} \quad [\mathrm{Wm^{-2}sr^{-1}Hz^{-1}}]. \tag{2.2}$$

This expression is valid if $f \ll 6\,\mathrm{THz}$ for a black-body with a physical temperature $T_{ph} = 300\,K$ (around ambient temperature). Hence, since the radiometric research presented in the following chapters has been performed at W-band ($75 - 110\,\mathrm{GHz}$) and at room temperature, the Rayleigh-Jeans approximation is used instead of the Plank's law for the sake of simplicity.

Figure 2.1 shows the spectral brightness B_b of a black-body with a physical temperature $T_{ph} = 300\,K$ in logarithmic scale, where can be stated that the Rayleigh-Jeans law is a good approximation of the Planck's law for mmW frequencies.

2.1.2 Antenna surrounded by a black body

A radiometer is the name given to the electronic receiver device used to measure the thermal radiation power emitted by a body. The received power by the radiometer with bandwidth B
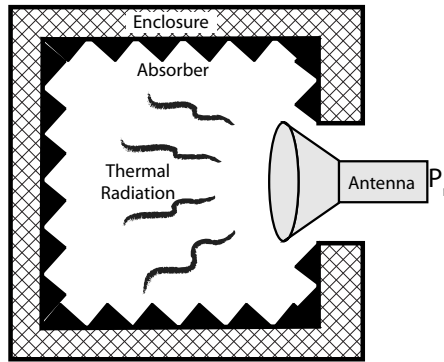
Figure 2.2: Schematic representation of an antenna surrounded by a black-body.

centered at f_0 is calculated by integrating the spectral brightness of the black-body along the frequency bandwidth and along a sphere. In an ideal case, when the radiometer antenna is surrounded by a black-body with constant T_{ph} as shown in Figure 2.2, the received power is

$$P_{\text{c}} = \frac{1}{2} A_{\text{e}} \int\limits_{f_0 - \frac{B}{2}}^{f_0 + \frac{B}{2}} \int \int_{4\pi} \frac{2k_{\text{B}}f^2}{c^2} T_{\text{ph}} t(\theta, \phi) d\Omega df = k_{\text{B}} T_{\text{ph}} B \quad (B \ll f_0) \quad [\text{W}], \qquad (2.3)$$

where A_{e} is the antenna effective area and $t(\theta, \phi)$ is the normalized antenna power pattern. The concept of antenna temperature T_{A} can be defined from the result in (2.3) as the temperature of an ideal black-body that would result in the same received power at the antenna aperture as in the actual case. Therefore, in an ideal receiver, the antenna temperature can be calculated as $T_{\text{A}} = P_{\text{c}}/(k_{\text{B}}B)$.

2.1.3 Gray body radiation and apparent temperature

Real objects do not behave as black-bodies but as gray-bodies. They differ in the sense that gray-bodies do not absorb all the incident radiation because part is reflected, and therefore only part of the incident energy is re-emitted. In addition, the radiation emitted by gray-bodies is not omnidirectional and thus, the radiation angular distribution should be taken into account. The spectral brightness of a gray-body B_{g} is expressed as

$$B_{\text{g}}(\theta, \phi) = \frac{2k_{\text{B}}f^2}{c^2} T_{\text{B}}(\theta, \phi), \qquad (2.4)$$

where T_{B} is the brightness temperature associated to the spectral brightness of the gray-body. The brightness temperature is related with the physical temperature by the material emissivity e as

$$e(\theta, \phi) = \frac{T_{\text{B}}(\theta, \phi)}{T_{\text{ph}}}. \qquad (2.5)$$

The emissivity depends on the material and several parameters such as temperature, emission angle and frequency. The Kirchhoff's law of thermal radiation states that, in thermal equilibrium emissivity equals absorptivity. Hence an object that does not absorb all incident energy

| | Emissivity | | Reflectivity | | Transmissivity | |
Material	100 GHz	500 GHz	100 GHz	500 GHz	100 GHz	500 GHz
Explosive	0.74	0.95	0.26	0.05	0	0
Metal	0	0	1	1	0	0
Skin	0.65	0.91	0.35	0.09	0	0
Denim	0.09	0.49	0.01	0.01	0.9	0.5
T-shirt	0.04	0.2	0	0	0.96	0.8

Table 2.1: Emissivity, reflectivity and transmissivity of typical materials
related with radiometric security imaging [49].

will emit less power than a black-body. From this statement arises the relation among the
emissivity e, reflectivity r and transmissivity t concepts:

$$e + r + t = 1. \tag{2.6}$$

Table 2.1 shows the emissivity, reflective and transmissivity values of various materials re-
lated with human body security imaging at $100\,\text{GHz}$ and $500\,\text{GHz}$. When a gray-body is
placed in a complex environment with other objects surrounding it, the power coming from
the gray-body is not only related with its physical temperature. There are two additional ef-
fects that are included in the measured power coming from the body: 1) the reflected energy
on the body surface; and 2) the energy that penetrates the body and is transmitted thorugh it.
The total measured power is related with an apparent temperature T_A seen from the body

$$T_A = eT_{\text{ph}} + rT_{\text{br}} + tT_{\text{bb}}, \tag{2.7}$$

where T_{br} is the brightness temperature of background which is reflected by the object and
T_{bb} is the temperature of the background behind the object.

2.1.4   Image temperature contrast

The power received by a radiometer coming from a body does not only depend on the body
physical temperature but also on its absorption characteristics and the environment bright-
ness temperature. Therefore the temperature contrast in an image acquired by a radiometer
will strongly depend on the environment when imaging objects that are not purely absorptive.
Table 2.1 shows that the usual object materials found in a security scene have a reflectivity
coefficient greater that 0.2 and in the limit, metal objects have a $r = 1$. Hence, the tempera-
ture contrast of objects that usually appear in security scenarios will strongly depend on the
reflected radiation coming from the environment. In security image two types of scenarios,
the indoor and the outdoor, are defined due two their different characteristics of background
brightness temperature distribution. Figure 2.1.4 shows an artist view with the background
radiation characteristics of both scenarios.

The outdoor scenario is represented in Fig. 2.3(a) where three different background radi-
ations are depicted: 1) the sky radiation has a brightness temperature of around $T_{\text{sky}} = 100\,\text{K}$
at mmW frequencies, although it depends on various parameters such as the incidence angle
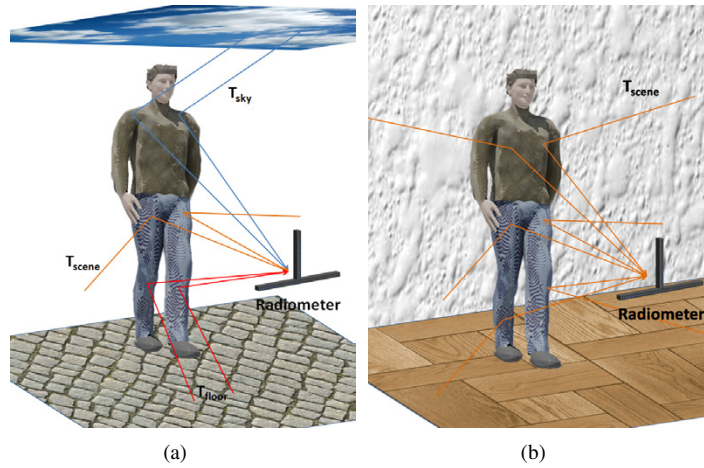
Figure 2.3: Artist views of an outdoor scenario (a) and an indoor scenario (b) depicting the background temperatures that affect the result of the image contrast.

and the cloud density; 2) the brightness temperature of the floor T_{floor} is related on its physical temperature that will depend on the quantity of absorbed solar radiation; and 3) the scene brightness temperature T_{scene} depends on the ambient temperature. The effect of each background radiation is different on the each image portion. The sky temperature is reflected on the shoulders and on metallic objects appearing very cold in the image. The opposite effect is found from the knees to the feet, where the floor radiation is reflected appearing warmer than the rest of the human body. As a result, usually the images have a temperature gradient from cold to warm going from the head to the feet.

Figure 2.3(b) corresponds to a indoor scenario where the brightness temperature of the environment T_{scene} is usually homogeneous and related to the ambient temperature, hence the effect on the image is uniform. The main difference between indoor and outdoor scenarios is the contrast level on the image. Outdoor scenarios experience higher contrasts since the reflection of the sky in the objects increase their apparent temperature difference. The dynamic range of the image also increases and goes from around $100\,\text{K}$ to the ambient temperature ($\approx 300\,\text{K}$). In an indoor scenario, the contrast is poor since the ambient temperature is very close to the body temperature and the dynamic range of the images is of around $20\,\text{K}$. In this case the radiometer should be more sensible in terms of received brightness temperature to be able to detect small changes in temperature. For a radiometer with a certain radiometric sensitivity indoor images are noisier than outdoor images and the detection capabilities are reduced in indoor scenarios. Measured images presented in section 2.2.6 are a good example to examine the aforementioned contrast differences.

2.2   Total-power radiometer with mechanical beam-scanning

The TPR is a basic radiometer receiver that collects the scene radiation by using an antenna, filters and amplifies the Radiofrequency (RF) signal and detects its power by using a device
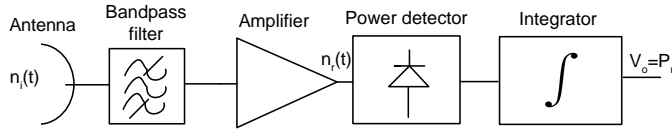
Figure 2.4: Block diagram of the basic components of a TPR.

with a quadratic response. The final step is to average the signal at the output of the power detector in order to improve the Signal to Noise Ratio (SNR). Figure 2.4 shows a simplified block-diagram of the radiometer components. The TPR is the most common radiometer due to its simplicity and is the one chosen to introduce the basic radiometry concepts that will appear along the document.[1]

The voltage noise signal at the input of the power detector $n_{\mathrm{r}}(t)$ can be modeled as

$$n_{\mathrm{r}}(t) = n_{\mathrm{Ir}}(t) \cos(\omega t) - n_{\mathrm{Qr}}(t) \sin(\omega t) \qquad [\mathrm{V}], \qquad (2.8)$$

where $N_{\mathrm{r}}(t) = n_{\mathrm{Ir}}(t) + j n_{\mathrm{Qr}}(t)$ is the equivalent baseband of the input noise. The phase and quadrature components, $n_{\mathrm{Ir}}(t)$ and $n_{\mathrm{Qr}}(t)$ respectively, are independent stochastic processes with Gaussian probability density function and standard deviation σ. Hence, if a unitary resistor is considered at the input of the power detector, the voltage value at the output of the integrator is

$$\overline{V_o} = \mathbb{E}\left\{\|N_{\mathrm{r}}(t)\|^2\right\} = 2\sigma^2 = k_B G B T_{\mathrm{sys}} \qquad [\mathrm{V}], \qquad (2.9)$$

where $\mathbb{E}\{\}$ is the expectation operator and G is the gain of the amplifier. The system temperature $T_{\mathrm{sys}} = T_{\mathrm{A}} + T_{\mathrm{R}}$ includes the contribution of the noise added by the receiver T_{R} to the input noise. The receiver noise temperature T_{R} depends on the Noise Figure (NFI) of the receiver (usually fixed by the first amplifier) and can be calculated as $T_{\mathrm{R}} = 290(\mathrm{NFI} - 1)$. The parameter B is the equivalent noise bandwidth of the bandpass filter defined by

$$B = \frac{1}{H_{\mathrm{max}}} \int_0^\infty |H(f)|^2 df \qquad [\mathrm{Hz}], \qquad (2.10)$$

being $H(f)$ the frequency response of the filter and H_{max} its maximum value. The measurement standard deviation gives an estimation of the sensitivity of the system and can be calculated as

$$\mathrm{std}(V_o) = \sqrt{\frac{\mathbb{E}\left\{\|N_{\mathrm{r}}(t)\|^4\right\} - \mathbb{E}\left\{\|N_{\mathrm{r}}(t)\|^2\right\}^2}{N}} = \frac{2\sigma^2}{\sqrt{N}} \qquad [\mathrm{V}], \qquad (2.11)$$

where N is the number of independent samples taken in the integration being equivalent to $N = B\tau$ where τ is the integration time. From (2.9) and (2.11) the radiometric sensitivity in terms of temperature resolution can be defined as

$$\Delta T_{\mathrm{N}} = \frac{T_{\mathrm{sys}}}{\sqrt{B\tau}} \qquad [\mathrm{K}] \qquad (2.12)$$

---

[1]The following paragraphs of this section may contain verbatim text and figures from [C6, C8, C12].

Ideally, ΔT_N can be arbitrarily low if the integration time is increased. However, the gain variability of the components in the receiver chain strongly reduces the sensitivity of the measurement. This is the main drawback of the TPR and can be solved using compensation techniques such as Dicke switching [50]. The effect of the gain variability on the system temperature is expressed as

$$\Delta T_G = T_{sys} \frac{\Delta G}{G} \qquad [K], \tag{2.13}$$

being independent from the noise statistics. The receiver sensitivity taking into account the gain uncertainty is given by

$$\Delta T = \sqrt{\Delta T_N{}^2 + \Delta T_G^2} = T_{sys} \sqrt{\frac{1}{B\tau} + \left(\frac{\Delta G}{G}\right)^2} \qquad [K], \tag{2.14}$$

The gain instability strongly increases ΔT reducing the radiometric sensitivity of the TPR. Usually, a thermal control is required on the radiometer components to minimize gain fluctuations. When acquiring an image, the fluctuation impacts along the whole image acquisition reducing the sensitivity. If no calibration is performed during the acquisition, the relation between brightness temperature and received power will vary from the first acquired pixel to the last one, yielding a distorted temperature map.

2.2.1 Total-power radiometer system design

A mmW TPR has been designed to evaluate the passive imaging performance at W-band. The receiver architecture of the TPR is presented in Fig. 2.5(a) is based on a double-sideband heterodyne receiver with $64\,\mathrm{dB}$ gain. The NFI of the radiometer is mainly fixed by the first Low-Noise Amplifier (LNA), the $1.5\,\mathrm{dB}$ of the isolator losses and the phase noise introduced by the Local Oscillator (LO).

A horn antenna is followed by an isolator that prevents the noise produced by the first LNA to be radiated by the radiometer. After the isolator, two LNA stages feed the W-band mixer achieving a chain gain of $64\,\mathrm{dB}$. The LO of the system is based on a $15.16\,\mathrm{GHz}$ Phase-Locked Oscillator (PLO) multiplied by 6 using a W-band multiplier. A LO signal of $91\,\mathrm{GHz}$ is mixed with the input noise signal, overlapping the RF bands from $88\,\mathrm{GHz}$ to $91\,\mathrm{GHz}$ and from $91\,\mathrm{GHz}$ to $94\,\mathrm{GHz}$, since the baseband bandwidth of the system is $3\,\mathrm{GHz}$.

The baseband noise power is directly measured using a power detector that provides an output voltage proportional with the input Root-Mean-Square (RMS) voltage. The output/input relation is calibrated and expressed by $V_o = 7.7\mathrm{V/V_{rms}}$. The video bandwidth of the detector is fixed to $2\,\mathrm{kHz}$, however the signal is further averaged using a microcontroller. Therefore, the video bandwidth of the receiver can be selected by changing the averaging time in the microcontroller.

The receiver temperature is stabilized by using a Proportional-Integral-Derivative (PID) controller with 3 heating resistors, 2 fan-coolers, 1 PT100 temperature sensor and 6 digital temperature sensors. Figure 2.5(b) shows a photograph of the radiometer with the parabolic reflector mounted on the pan-tilt scanner system.
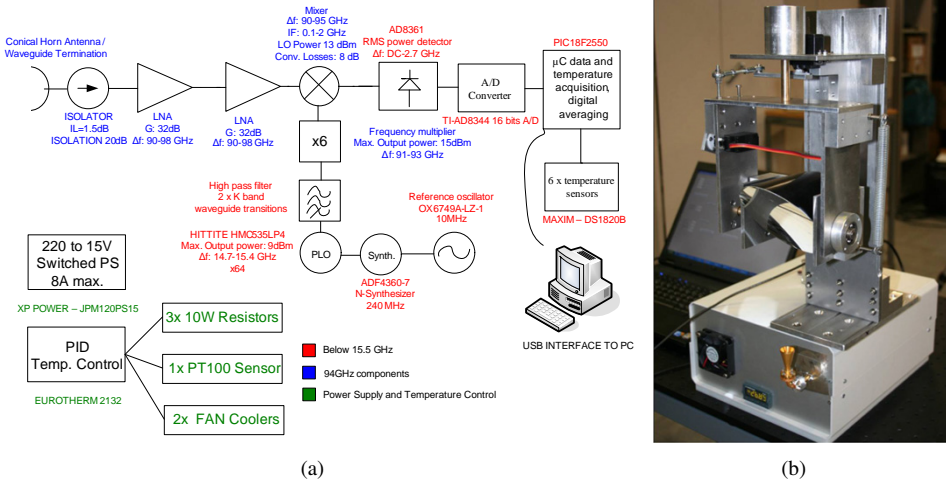
Figure 2.5: (a) Receiver schematic and hardware components of the TPR.
(b) Photograph of the total power radiometer with the scanning system.

2.2.2 Calibration

The radiometer has been calibrated using a method based on measuring a temperature sweep of a resistor block. The parabolic mirror is aimed sequentially to a resistor block and to an absorber with fixed temperature in order to compensate gain fluctuations of the receiver. In each measurement the resistor temperature is modified, starting with $100\,^\circ$C and reducing the temperature in different steps down to $30\,^\circ$C, obtaining 7 calibration points plus 7 reference points. An infrared camera together with a K thermocouple sensor are used to measure the temperature of both the absorber and the resistor block.

The relation between receiver power and brightness temperature of the scene is given by

$$T_\mathrm{B} = aP_\mathrm{o} + b, \tag{2.15}$$

where the parameter $T_\mathrm{B} \approx T_\mathrm{ph}$ is the brightness temperature of the resistor block (where e has been considered 1), b basically depends on the receiver noise temperature and P_o is the corrected received power. The proportional constant a depends basically on the Boltzmann constant, the bandwidth of the receiver, the gain of both LNAs and the losses of the mixer.

The correction of the received power is performed by multiplying the measured power the ratio between the reference measurement P_ref and the absorber measurement P_abs yielding

$$P_\mathrm{o} = \frac{P_\mathrm{ref}}{P_\mathrm{abs}} P_\mathrm{r}. \tag{2.16}$$

Finally, the a and b parameters are obtained by inverting the simultaneous equations obtained
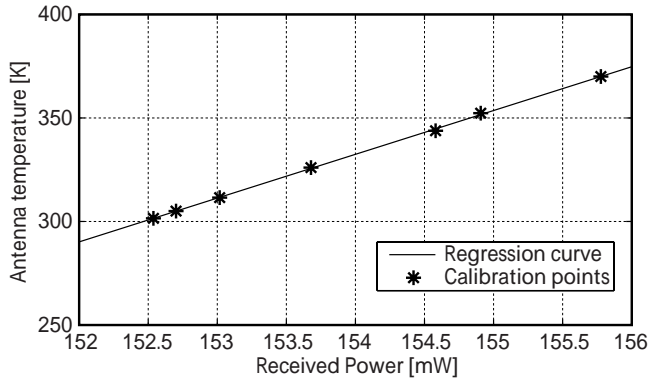
Figure 2.6: TPR calibration curve.

from 7 measurements

$$\begin{bmatrix} a \\ b \end{bmatrix} = \begin{bmatrix} P_{c1} & 1 \\ P_{c2} & 1 \\ \vdots & \vdots \\ P_{c7} & 1 \end{bmatrix}^{+} \cdot \begin{bmatrix} T_{b1} \\ T_{b2} \\ \vdots \\ T_{b7} \end{bmatrix}, \tag{2.17}$$

where the symbol " $+$ " denotes the pseudoinverse of the matrix. The calibration result curve is depicted in Fig. 2.6 having a calculated variance of $0.24\,\mathrm{K}$.

2.2.3 Performance Assessment

The radiometric resolution ΔT in $\mathrm{K}/\sqrt{\mathrm{Hz}}$ of the radiometer has been characterized by measuring the radiometer output response, based on the ratio between the power detector output voltage spectral density ΔV in $\mathrm{V}/\sqrt{\mathrm{Hz}}$ and the power detector output Direct-Current (DC) voltage V_{DC}.

Two different regimes exist in the radiometer response separated by the so-called corner-frequency. In the low frequency region the $1/f$ noise produced mainly by gain fluctuations in the receiver chain predominates whereas in the region beyond the corner-frequency $\Delta V/V_{\mathrm{DC}}$ converges to $\sqrt{1/(2B)}$ in the case of using a linear power detector [51].

The characterization of the first region gives an information of the radiometer response drift for long radiometer acquisition times (e.g. the acquisition of an image). If no calibration is performed during the acquisition of an image, the ΔT will depend on the radiometer stability and thus on the output $1/f$ noise, as described in [52] [53]. However, if the radiometer is calibrated at a faster frequency rate than the corner-frequency (e.g. with a Dicke switch), the ΔT is constant with a relative value of $\sqrt{2/B_{\mathrm{RF}}}$. In this case, the relation between ΔV and ΔT is given by

$$\frac{\Delta T}{T_{\mathrm{sys}}} = 2\frac{\Delta V}{V_{\mathrm{DC}}}. \tag{2.18}$$

In order to obtain ΔV, the output voltage frequency spectrum of the detector has been acquired and normalized by the video bandwidth with a HP 3561A Dynamic Signal Ana-
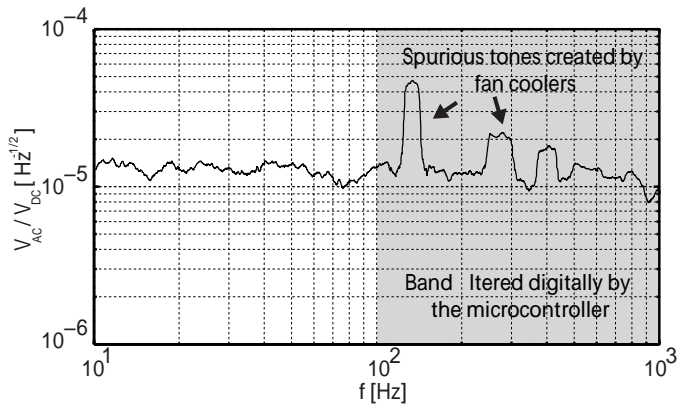
Figure 2.7: Measured radiometer response spectrum against video frequency.

lyzer. The measurements have been performed with the radiometer input terminated with a temperature controlled matched load at a temperature of $298\,\mathrm{K}$. Figure 2.7 shows the measured $\Delta V/V_{\mathrm{DC}}$ for video frequencies between $10\,\mathrm{Hz}$ and $1\,\mathrm{kHz}$, corresponding to frequencies beyond the corner-frequency.

The $\Delta V/V_{\mathrm{DC}}$ is flat from $10\,\mathrm{Hz}$ to $100\,\mathrm{Hz}$ with a mean value of $12.9 \cdot 10^{-6}\,\mathrm{Hz}^{-\frac{1}{2}}$, giving equivalent noise RF bandwidth B_{RF} of $3\,\mathrm{GHz}$. Beyond $100\,\mathrm{Hz}$, spurious tones created by the cooler fans appear. A better isolation between power supplies of the fans and the RF circuitry should be performed to avoid this effect. Nevertheless, the radiometer is operated with integration times greater than 1 ms, canceling these spurious signals. As a final result, the computed ΔT from $10\,\mathrm{Hz}$ to $100\,\mathrm{Hz}$ is $83\,\mathrm{mK}/\sqrt{\mathrm{Hz}}$.

2.2.4   Description of the antenna system

The antenna system mounted on top of the radiometer is shown in Fig. 2.8(b). A $90°$-offset parabolic reflector with $100\,\mathrm{mm}$ of diameter and a focal distance of $152\,\mathrm{mm}$ has been used to enhance the spatial resolution of the imaging system. Moreover, it has been mounted on a pan-tilt scanner to acquire images at close standoff distances. The scanner is moved by two servo motors, one per each axis, yielding a rotation resolution of $0.15\,°$ for both axes. The reflector is fed by a horn antenna placed at $192\,\mathrm{mm}$ from the reflector. Adjusting the feeding point further away from the reflector focal distance allows a proper near-field focusing at $1\,\mathrm{m}$.

An approximated value of the angular resolution (-3 dB) is given by $\Delta\theta = \lambda/D$ for an uniform illumination, where λ is the wavelength at the center RF frequency of $91\,\mathrm{GHz}$ and D is the diameter of the reflector. From this equation, $1.9\,°$ of beamwidth is obtained, translated to $3.3\,\mathrm{cm}$ at $1\,\mathrm{m}$ standoff distance.

Figure 2.8(a) shows a simulation of the radiation pattern of the radiometer antenna. In order to obtain the radiation pattern of the horn-reflector group, two simulation steps have been followed: the first step is obtaining the radiation spherical modes of the horn using a Method of Moments (MoM) simulation; and the second step is to use the spherical modes of the horn as a point source in a Physical Optics (PO) simulation of the reflector.
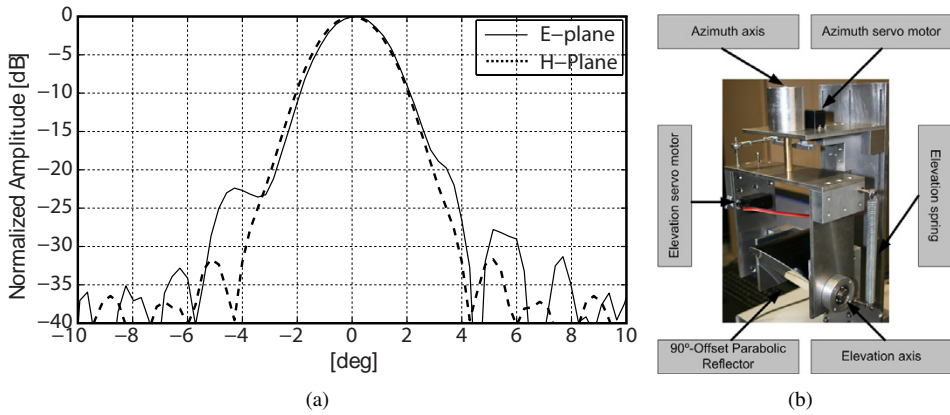
Figure 2.8: (a) Simulated radiation pattern of the radiometer antenna when focusing at $1\,\mathrm{m}$. (b) Photograph of the antenna system specifying the main components.

The simulation results show a beamwidth of $2.28\,^\circ$, slightly wider than the theoretical since the taper caused by the horn illumination produces a reduction of the incident power at the edge of the reflector of $10\,\mathrm{dB}$. This effect reduces the angular resolution of the antenna but improves the beam efficiency. The resulting beam efficiency η_b has been calculated as

$$\eta_\mathrm{b} = \frac{\int_0^{2\pi} \int_0^{\theta_\mathrm{b}} t(\theta, \phi) \sin\theta d\theta d\phi}{\int_0^{2\pi} \int_0^{\pi} t(\theta, \phi) \sin\theta d\theta d\phi}, \tag{2.19}$$

where $t(\theta, \phi)$ is the normalized power pattern of the antenna system and θ_b is half of the beamwidth of the antenna. This calculation gives the ratio of power received by the imaged pixel over the total power received, achieving a $94\,\%$ for the current antenna system. It has to be pointed out the importance of the beam efficiency in our system, since either the spillover at the reflector or sidelobes effects caused by a sharp taper drastically increases the radiometer acquisition error.

2.2.5 Beam distortion

In order to assess the distortion effect produced by the incidence angle and by the displacement of the reflector focus when aiming in elevation, the measurements shown in Fig. 2.9 have been performed. A resistor panel has been placed behind an absorber material having a hole of $1\,\mathrm{cm}$ of diameter, thus creating a hot spot. Two images have been obtained at $1\,\mathrm{m}$ distance: Fig. 2.9(a) shows an image of the hot spot when it is centered in the scene; additionally, a second image presented in Fig. 2.9(b) is acquired when the hot spot has been displaced to the coordinates $(0.4, 0.4)\,\mathrm{m}$ in the scene, thus having the beam an incidence angle of $22\,^\circ$.

Two effects are observed when aiming to the border of the scene in Fig. 2.9(b), both the dynamic range of the image and the spatial resolution are worse than in Fig. 2.9(a). Specifically, the spatial resolution increases from approximately $4\,\mathrm{cm}$ to $6\,\mathrm{cm}$ due to the beam distortion. Moreover, the dynamic range is reduced by $15\,\mathrm{K}$ since the beam efficiency is reduced.

(a) Centered point source (b) Displaced point source
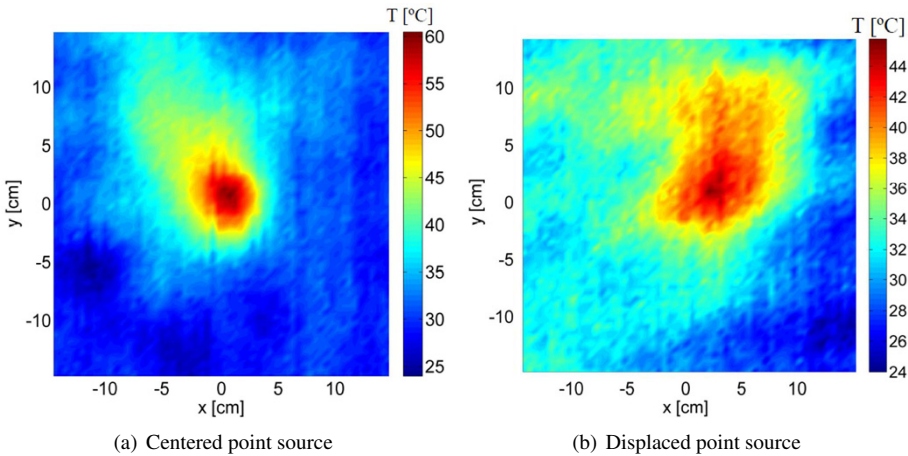
Figure 2.9: Acquired point source images to assess the beam distortion when aiming to the scene limits.

2.2.6 Imaging Performance

The radiometer performs a continuous raster scan in elevation and a step scan in azimuth. For each pixel position, the radiometer microcontroller performs the desired integration of the signal provided by the power detector and sends the value via Universal Serial Bus (USB) to the computer. The computer software synchronizes the reflector aiming position with the power acquisition and stores the information in a 3-dimensional matrix with the elevation, azimuth and power values.

Figure 2.10(a) shows a 50x50 pixels image of a person on a chair with a toy gun concealed under a T-shirt. As a reference, Fig. 2.10(b) shows an snapshot of the same scene recorded with an infrared camera from a different point of view. The image has been acquired with $70\,\mathrm{ms}$ of integration time per pixel. The calibration has been performed applying the curve given in Fig. 2.6 and using an absorber as a reference temperature. Even though the image has been acquired in an indoor environment, still there is enough contrast between the toy gun and the person to identify the shape of the object.

The total acquisition time is $5\,\mathrm{min}$, yielding a mean acquisition time per pixel of $120\,\mathrm{ms}$ taking into account the mechanical movement. The theoretical radiometric resolution of the image is $0.22\,\mathrm{K}$ calculated from the measured value of ΔT in section 2.2.3. However, since only one reference calibration is performed, the radiometric resolution is degraded by drifts in the radiometer response.

A second example of an indoor image from a standing person carrying a toy gun on the waist is shown in Fig. 2.11(b). It consists of a radiometric image with 100x40 pixels acquired in 7 minutes. The radiometric image has $19\,\mathrm{K}$ of dynamic range, showing an apparent temperature of $295\,\mathrm{K}$ for the background and $305\,\mathrm{K}$ for the person. The toy gun and the belt buckle are recognizable as well as the mobile phone carried on the pocket.

The apparent temperature of the person skin in the image will depend on the mean value between its physical temperature and the reflected brightness temperature of the environment. The metal surface of the gun however has a reflectivity value of $r = 1$, thus only reflecting
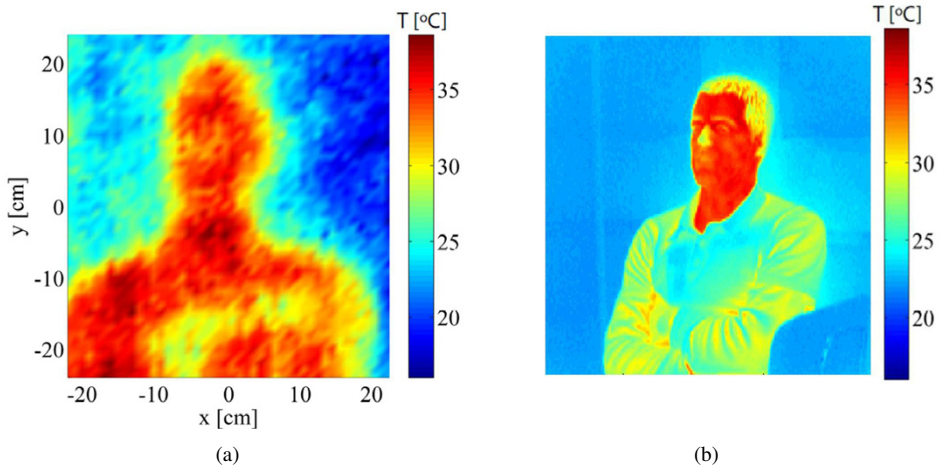
Figure 2.10: (a) W-band radiometric indoor image of a person on a chair with a concealed toy gun under a T-shirt. (b) Infrared image of the same scene.

Figure 2.11: (a) Optical, (b) radiometric and (b) infrared indoor images of a standing person with a concealed toy gun under a T-shirt.

the environmental brightness temperature. As a result of the low contrast of the scenario, a noisy image is obtained and the gun is detected but hard to identify. An infrared image of the imaged scene is presented in Fig. 2.11(c). Even though the spatial resolution of the infrared image is greater than the radiometric image, the toy gun is harder to be detected since the T-shirt is more opaque to infrared frequencies.

Fig. 2.12(b) presents a 100x50 pixels image of a person with a concealed toy gun as in

Fig. 2.11(b), however in this case the image has been acquired in an outdoor environment. The dynamic range of the image is around $200\,\mathrm{K}$ with a background apparent temperature of approximately $100\,\mathrm{K}$. The image has been obtained in a roof of a building with an tilted metallic plate that reflects the sky as shown in Fig. 2.12(a). Therefore the background of the image has the same brightness temperature as the sky. A temperature gradient of around $50\,\mathrm{K}$ is observed in the body. This effect is due to the incidence angle of the radiometer at the person.

For a negative incidence angle, that is when aiming below the waist of the person, the body is reflecting the floor of the roof that is around $310\,\mathrm{K}$ of physical temperature. Hence, this part of the image appears warmer due to the contribution of the building and the surroundings. For positive incidence angles the body reflects the sky reducing the apparent temperature of this part of the body. Furthermore, for high incidence angles there is a distortion caused by the projection of the beam on the body and by the displacement of the focus of the reflector. This distortion is clearly observed in the image as a stretched neck. The toy gun appears with an apparent temperature of around $240\,\mathrm{K}$ since it reflects partially the sky. The high contrast of the image compared with the radiometer sensitivity provides a clean image compared with the noisy image presented in Fig. 2.11(b).

The radiometer sensitivity is enough to detect a concealed toy gun under a T-shirt in an indoor environment. However due to the low contrast of the image the identification of the object is hard to achieve. In the outdoor environment, where the contrast is clearly higher than the radiometric sensitivity the smooth edges and the clean image allows both detection and identification of the concealed object. Appendix A shows a variety of outdoor images obtained with the TPR radiometer described in this section. The images show the body shape of each person in a way that is impossible to see from an optical image. Hence, mmW images can be used as a source of biometric information.

2.3 Synthetic Aperture (SA) Interferometric Radiometry

Whereas the TPR radiometer is formed by just one receiver, the interferometric radiometer is composed by multiple receivers forming an SA array. Each receiver element captures the radiation coming from the scene, performs its demodulation and sends the processed signal to a correlator processing unit. By correlating all combinations of signals coming from all receiver pairs, the so-called visibility values of the scene are obtained, being related with the temperature map of the scene by a Fourier Transform (FT). In the following sections, the basic concepts of SA radiometry are introduced with special emphasis on performance parameters such as radiometric sensitivity and spatial resolution.

2.3.1 Time-domain correlation

Figure 2.13 shows a block diagram of a basic passive interferometer composed by two radiometric receivers and a correlator. The process of capturing the thermal noise from the scene is also depicted in the figure. Assuming that both receivers are equal, the result of the

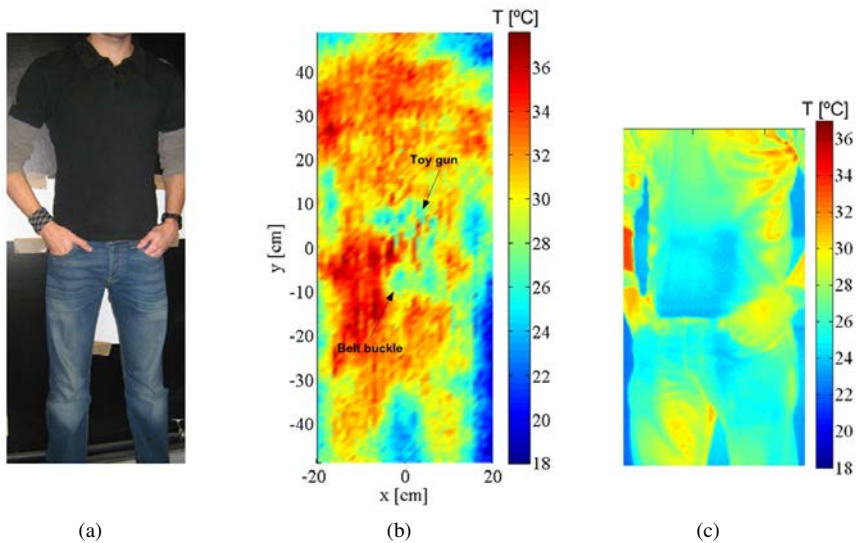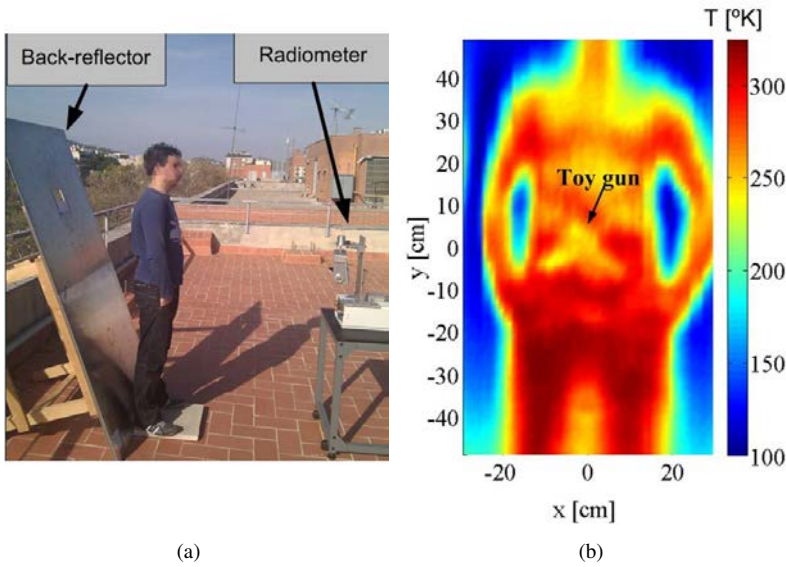**Figure 2.12:** (a) Optical and (b) radiometric infrared outdoor images of a standing person with a concealed toy gun under a T-shirt.
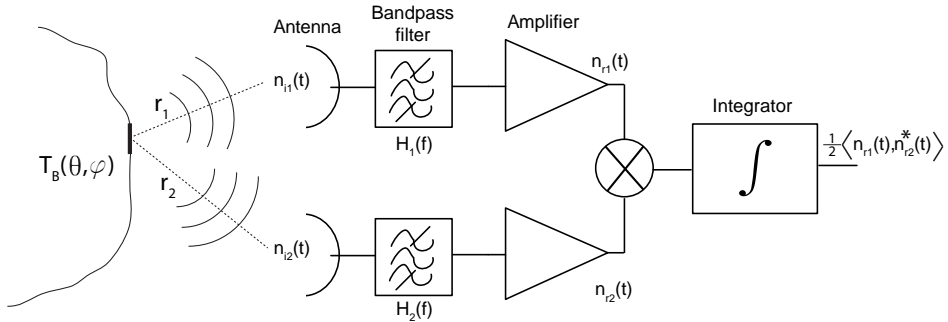
Figure 2.13: Reception of the scene thermal radiation by two receivers and their block diagrams representing the correlation process.

correlation is

$$\frac{1}{2}\langle n_{\mathrm{r}1}(t), n_{\mathrm{r}2}^*(t)\rangle = \frac{k_{\mathrm{B}}}{\Omega_{\mathrm{p}}} \iint_{4\pi} \int_0^\infty T_{\mathrm{B}}(\theta, \phi) t(\theta, \phi) \|H(f)\|^2 e^{-jk(r_2 - r_1)} df \, d\Omega, \qquad (2.20)$$

where $H(f)$ is the spectral response of the receiver chain consisting basically of the band-pass filter and the amplifier, the $\frac{1}{2}$ term is considered since only the signal associated to one polarization state is captured, $t(\theta, \phi)$ is the normalized power pattern of the single element antenna, $k = \frac{2\pi}{\lambda}$ is the wavenumber and Ω_{p} is the antenna pattern solid angle. The term that takes into account the decorrelation effects that appear when correlating band-limited signals
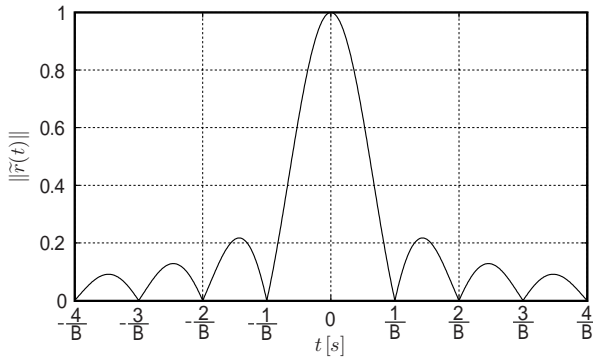
Figure 2.14: Modulus of the fringe washing function $\|\widetilde{r}\|$ for ideal rectangular filtering with bandwidth B.

is the so-called fringe washing function $\widetilde{r}(t)$ and is defined as

$$\widetilde{r}(t) = \frac{e^{-j2\pi f_0 t}}{BG} \int_0^\infty \|H(f)\|^2 e^{j2\pi f t} df, \tag{2.21}$$

where B is the noise equivalent bandwidth of the filter and G is the amplifier gain. Hence, (2.20) can be rewritten as

$$\frac{1}{2}\langle n_{r1}(t), n_{r2}^*(t)\rangle = \frac{k_B BG}{\Omega_p} \iint_{4\pi} T_B(\theta, \phi) t(\theta, \phi) \widetilde{r}\left(\frac{\Delta r}{c}\right) e^{jk_0 \Delta r} d\Omega, \tag{2.22}$$

where k_0 is the wavenumber associated with the central frequency of the filter and $\Delta r = r_2 - r_1$. The result of the integral shown in (2.21) gives the following result for the temporal definition of the fringe washing function for a rectangular filter with bandwidth B:

$$\widetilde{r}(t) = e^{-j2\pi f_0 t} \text{sinc}(Bt). \tag{2.23}$$

Figure 2.14 shows a plot of (2.23) pointing out that $\frac{\Delta r}{c} \ll \frac{1}{B}$ to maintain the correlation between the signals of both receivers. Otherwise, the correlation level could fall below the sensitivity of the receiver or even it can be canceled out if $\frac{\Delta r}{c} = \frac{1}{B}$. In practice, this means that the Field of View (FoV) is constrained by the bandwidth of the receiver. If a large bandwidth is used to improve the sensitivity of the receiver, the FoV will be reduced and viceversa.

2.3.2   Visibility function

A SA interferometric radiometer is formed by an array of antennas such as the one given in Fig. 2.15 where the receiver elements are represented by black dots. It is convenient to express the coordinate system in direction cosines $\xi = \sin\theta\cos\phi$ and $\eta = \sin\theta\sin\phi$ to simplify the formulation. Hence, the path difference Δr of the signals captured by two receivers can be approximated by $\Delta r \approx -[\xi(x_2 - x_1) + \eta(y_2 - y_1)]$ if the paraxial approximation
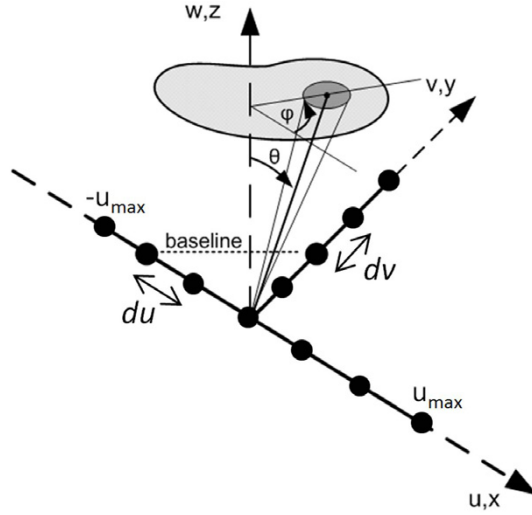
Figure 2.15: Geometry of a 2D-SA T-shape interferometric radiometer.

is assumed, where (x_i, y_i) are the antenna coordinates. If the coordinates (u, v) are defined as the normalized antenna spacing $(u, v) = (\frac{x_2 - x_1}{\lambda}, \frac{y_2 - y_1}{\lambda})$, (2.22) can be expressed for any pair of receivers as

$$\frac{1}{2}\langle n_{\mathrm{r}i}(t), n_{\mathrm{r}j}^*(t)\rangle = \frac{k_{\mathrm{B}}BG}{\Omega_{\mathrm{p}}} \iint\limits_{\xi^2 + \eta^2 \leq 1} \frac{T_{\mathrm{B}}(\xi, \eta) - T_{\mathrm{r}}}{\sqrt{1 - \xi^2 - \eta^2}} t(\xi, \eta) \widetilde{r}\left(-\frac{u\xi + v\eta}{f_0}\right) e^{-j2\pi(u\xi + v\eta)} d\xi d\eta,$$

(2.24)

where the receiver equivalent noise temperature T_{r} term is added to account for the coupling between antennas [54]. The function containing the cross-power spectral density of the signals of all combinations of receiver pairs (i, j) is defined as the visibility function $V_{ij}(u, v)$ and is given by

$$V_{ij}(u, v) = \frac{1}{2k_{\mathrm{B}}BG}\langle n_{\mathrm{r}i}(t), n_{\mathrm{r}j}^*(t)\rangle,$$

(2.25)

For identical receivers there is no distinction among visibilities corresponding to the same baseline $V_{ij}(u, v) = V(u, v)$. In this case, from (2.24) and (2.25) the relationship between the temperature map $T_B(\xi, \eta)$ of the scene and the visibility function is given by a FT [55]:

$$V(u, v) = \mathfrak{F}\left[\frac{T_{\mathrm{B}}(\xi, \eta) - T_{\mathrm{r}}}{\sqrt{1 - \xi^2 - \eta^2}} \widetilde{r}\left(-\frac{u\xi + v\eta}{f_0}\right)\frac{t(\xi, \eta)}{\Omega_{\mathrm{p}}}\right] = \mathfrak{F}\left[T'_{\mathrm{B}}(\xi, \eta)\right] \quad [\mathrm{K}],$$

(2.26)

where $T'_{\mathrm{B}}(\xi, \eta)$ is the modified brightness temperature of the scene including the antenna pattern, the fringe washing function and the $-T_{\mathrm{r}}$ term.

Note from (2.26) that since the (u, v) space is sampled with discrete intervals (du, dv), the angular dimensions of the target is constrained by the Nyquist theorem. If the FoV dimensions are given by $(\xi_{\mathrm{max}}, \eta_{\mathrm{max}})$ the antenna separation in wavelength units is given by the Nyquist sampling theorem $(du = (2\xi_{\mathrm{max}})^{-1}$ and $dv = (2\eta_{\mathrm{max}})^{-1})$. Note that if the antenna
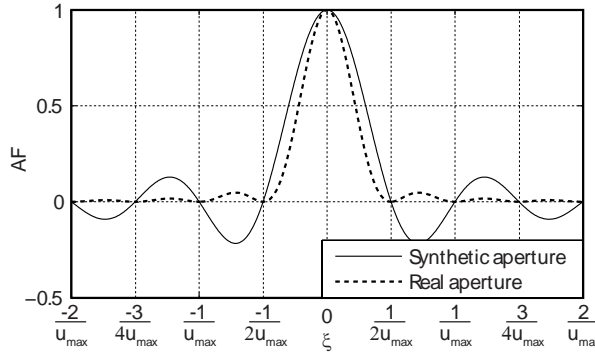
Figure 2.16: Comparison between array factors of a SA and a rectangular RA.

separation (du and dv) is greater than $\lambda_0/2$ (where λ_0 is the system wavelength at the central frequency of the filter), the image presents aliasing of the scene background. However, this issue can be solved in screener applications where differential imaging, with respect to an homogeneous background, can be used to set the alias zone to zero and cancel its contribution to the reconstructed image [56].

2.3.3 Beamwidth of the synthesized beam

The number of measured visibility samples is limited and depends on the number of antennas. Therefore the (u,v) domain is windowed with a window $W(u,v)$ that extends to the array size (u_{max}, v_{max})

$$T'_{\mathrm{B}}(\xi,\eta) = \iint W(u,v)V(u,v)e^{j2\pi(u\xi+v\eta)}dudv, \tag{2.27}$$

where the product $W(u,v)V(u,v)$ in the transformed domain (u,v) is equivalent to a convolution in the (ξ,η) domain of their inverse Fourier transforms

$$T'_{\mathrm{B}}(\xi,\eta) = \iint T'_{\mathrm{B}}(\xi',\eta')AF(\xi-\xi',\eta-\eta')d\xi'd\eta', \tag{2.28}$$

where the inverse Fourier Transform (iFT) of the window is the antenna factor $AF(\xi,\eta)$, also called point source response [57] [58]. When a rectangular window is used to account for the finite coverage of the (u,v) domain, the array factor is defined as

$$AF(\xi,\eta) = \mathrm{sinc}(2u_{\mathrm{max}}\xi)\mathrm{sinc}(2v_{\mathrm{max}}\eta). \tag{2.29}$$

The Half-Power Beamwidth (HPBW) for both x and y axes is given by

$$\Delta\theta_{\mathrm{x}} \cong \Delta\xi = \frac{0.60}{u_{\mathrm{max}}} \quad ; \quad \Delta\theta_{\mathrm{y}} \cong \Delta\eta = \frac{0.60}{v_{\mathrm{max}}}. \tag{2.30}$$

It must be pointed out that a physical aperture with uniform fields and the same size in the sampling domain $2u_{max}\mathrm{x}2v_{max}$ would have a different HPBW. In this case, the normalized

antenna power pattern would be approximated for small θ values by [59]:

$$t(\xi, \eta) \cong \left[\mathrm{sinc}(2u_{\mathrm{max}}\xi)\right]^2 \left[\mathrm{sinc}(2v_{\mathrm{max}}\eta)\right]^2. \tag{2.31}$$

And, due to the squared terms, the HPBW of the equivalent aperture would be

$$\Delta\theta_x \cong \frac{0.44}{u_{\mathrm{max}}} \quad ; \quad \Delta\theta_y \cong \frac{0.44}{v_{\mathrm{max}}}. \tag{2.32}$$

Figure 2.16 shows a comparison between antenna factors of a SA and a RA. For apertures of the same size, the RA yields better spatial resolution than the SA.

2.3.4   Pixel overlapping in the synthesized images

Due to the Discrete Fourier Transform (DFT) properties, in the (ξ, η) domain the pixels are equally spaced with a separation

$$d\xi = \frac{1}{2u_{\mathrm{max}}} \quad ; \quad d\eta = \frac{1}{2v_{\mathrm{max}}}. \tag{2.33}$$

In addition, the T-shaped array in Fig. 2.15 measures the visibility samples in a square of $N_{\mathrm{u}}\mathrm{x}N_{\mathrm{v}}$ equally spaced points in the (u, v) domain given by

$$N_{\mathrm{u}} = 2\frac{u_{\mathrm{max}}}{du} + 1 \quad ; \quad N_{\mathrm{v}} = 2\frac{v_{\mathrm{max}}}{dv} + 1. \tag{2.34}$$

Hence, from (2.34) and (2.33), the number of pixels in the synthesized domain (ξ, η) equals the number of visibility samples in the (u, v) domain:

$$N_{\mathrm{px}} = \frac{2\xi_{\mathrm{max}}}{d\xi} + 1 = N_{\mathrm{u}};$$

$$N_{\mathrm{py}} = \frac{2\eta_{\mathrm{max}}}{d\eta} + 1 = N_{\mathrm{v}}. \tag{2.35}$$

For a large number of antennas, pixel spacing can be given as a function of the synthesized beam HPBW in each of the orthogonal directions by combining (2.30) into (2.33):

$$d\xi = \frac{\Delta\xi}{1.2} \quad ; \quad d\eta = \frac{\Delta\eta}{1.2}. \tag{2.36}$$

It is shown that pixel separation is lower than the HPBW. Therefore, the interferometric radiometer with rectangular taper yields to a pixel overlapping factor of 1.2. This factor will be used when comparing the performances of the interferometer and the RA radiometer in chapter 3.

2.3.5   Radiometric sensitivity

The variance at the output of the correlator and therefore the variance of a single visibility measurement σ_{v}^2 is given by [60]:

$$\sigma_{\mathrm{v}}^2 = \rho_{\mathrm{r}1}\rho_{\mathrm{r}2} + \rho_{\mathrm{r}1\mathrm{r}2}^2 = k_{\mathrm{B}}^2(T_{\mathrm{A}}^2 + T_{\mathrm{sys}}^2)B^2, \tag{2.37}$$
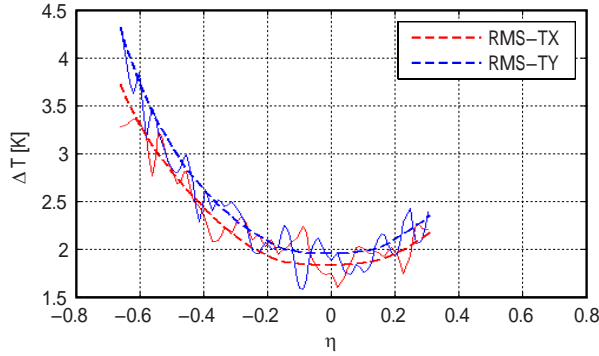
Figure 2.17: Radiometric sensitivity of the MIRAS/SMOS instrument over the ocean compared
with the theoretical estimation as given in [62].

where ρ_{ri} is the autocorrelation at the origin of the signal $n_{\mathrm{r}i}(t)$ and ρ_{r1r2} is the cross-correlation at the origin between $n_{\mathrm{r1}}(t)$ and $n_{\mathrm{r2}}(t)$. Hence, if $T_{\mathrm{A}} \ll T_{\mathrm{sys}}$, the temperature standard deviation of a visibility measurement is

$$\Delta T_{\mathrm{v}} = \frac{T_{\mathrm{sys}}}{\sqrt{B\tau}} \quad [\mathrm{K}]. \tag{2.38}$$

In order to calculate the standard deviation of the modified brightness temperature, the inversion equation (2.27) is discretized

$$T'_{\mathrm{B}}(\xi,\eta) = \Delta s \sum_{m} \sum_{n} W(u_{\mathrm{mn}}, v_{\mathrm{mn}}) V(u_{\mathrm{mn}}, v_{\mathrm{mn}}) e^{j2\pi(u_{\mathrm{mn}}\xi + v_{\mathrm{mn}}\eta)}, \tag{2.39}$$

where Δs is the elementary area in (ξ, η). Hence, if visibility errors are uncorrelated the standard deviation of the modified brightness temperature is

$$\Delta T'_{\mathrm{B}}(\xi,\eta) = \Delta s \Delta T_{\mathrm{v}} \sqrt{\sum_{m} \sum_{n} W_{\mathrm{mn}}^2} = \Delta s \frac{T_{\mathrm{sys}}}{\sqrt{B\tau}} \alpha_{\mathrm{w}} \sqrt{N_{\mathrm{v}}}, \tag{2.40}$$

where α_{w} is a parameter that depends on the window and N_{v} is the number of visibility samples. From (2.26) and (2.40), the radiometric resolution of a SA radiometer imaging an extended source of thermal radiation is [61]:

$$\Delta T_{\mathrm{B}}(\xi,\eta) = \Delta s \frac{T_{\mathrm{A}} + T_{\mathrm{R}}}{\sqrt{B\tau}} \frac{\Omega_{\mathrm{p}}}{t(\xi,\eta)} \sqrt{1 - \xi^2 - \eta^2} \frac{\alpha_{\mathrm{w}} \alpha_{\mathrm{s}}}{\alpha_{\mathrm{f}}} \sqrt{N_{\mathrm{v}}} \quad [\mathrm{K}] \tag{2.41}$$

where α_{s} takes into account the sensitivity loss due to non-analog correlation and α_{f} takes into account the pre-detection filter shape.

The accuracy of this formula has been recently validated by the MIRAS/SMOS instrument [62] launched on November 2009. Figure 2.17 shows a comparison between the radiometric sensitivity ΔT_B of the Microwave Imaging Radiometer using Aperture Synthesis (MIRAS) instrument calculated with (2.41) (dotted lines) and measured by means of brightness temperature images over the ocean (continuous line) for both horizontal (Tx) and vertical (Ty) polarizations at the antenna plane.

2.4   Conclusion

In this chapter, a brief description of classical radiometry concepts has been performed as an introduction of the research presented in this document. Special attention is paid to SA interferometric radiometry since the main research is done in this area.

In addition, a practical study of mmW radiometry has been presented in this chapter, exposing the imaging capabilities of a mechanically scanned radiometer for concealing object detection. The simplicity of the receiver architecture and its good performance in terms of spatial resolution and radiometric sensitivity makes it appropriate for applications where the acquisition time is not constrained. The antenna subsystem achieves enough spatial resolution to detect objects with dimensions on the order of several centimeters. In addition, having radiometric sensitivity close to 1 K has allowed the acquisition of low-contrast indoor images that reveal concealed objects with only few degrees of temperature contrast.

Nevertheless, it is unfeasible to use a single-receiver mechanically scanned system for real-time imaging purposes. The following chapters present performance studies and practical solutions with the objective of optimizing the acquisition time and the cost of the imaging system.

Millimeter-wave Performance Constraints for Passive Close-Range Screening

Iₙ this chapter, a theoretical study of the performance constraints appearing in passive close-range screening are studied. Three types of radiometers have been analyzed in terms of radiometric sensitivity and spatial resolution: 1) the Two-Dimensional Synthetic Aperture (2D-SA) radiometer; the One-Dimensional Synthetic Aperture (1D-SA) radiometer and the Real-Aperture (RA) radiometer. The analytical expressions for the radiometric resolution, the number of required antennas and the number of pixels in the image are derived taking into account the distortion produced by the Near Field (NF) geometry at non-boresight directions where the distortion is dominant. The image distortion caused by the NF geometry is assessed by using 2D-SA screener simulations.

An screener geometry based on a sparse linear array is proposed as an optimum solution to achieve the best performance with the minimum number of receivers. If a moving walkway is used with a sparse linear array, no mechanical movements are needed on the receiver. Special attention is paid to this system since it solves problems regarding the number of receivers and acquisition time. Based on theoretical results a performance comparison among the studied systems is carried out to show the advantages and drawbacks when using the radiometers in a close-range screening application. Additionally the screener performance in a close-range environment is discussed from the results obtained in the aforementioned comparison. [1]

3.1 Close-range aperture synthesis

In this section the performance expressions for the 2D-SA, 1D-SA and RA radiometers are particularized for close-range screening. In the case of the interferometer systems, a T-shape array is the optimum configuration regarding a rectangular Field of View (FoV) as the one required by screening systems [60]. Therefore, the analytical expressions of sensitivity and

---

[1]The following sections of this chapter may contain verbatim text and figures from [J2].
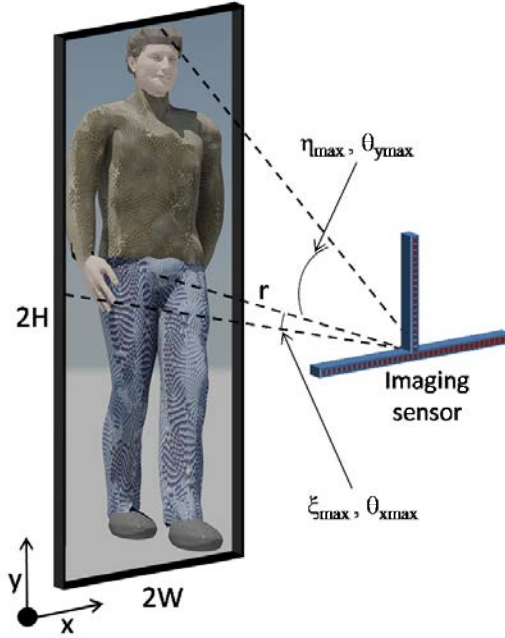
Figure 3.1: Imaging setup used to compare different screening configurations.

spatial resolution are derived for this geometry. Figure 3.1 shows the screener geometry and its disposition with respect the scene. The scene dimensions 2Wx2H together with the imaging range r define the FoV of the system.

In order to use the inverse Fast Fourier Transform (iFFT) to obtain the image from the visibilities measured by the interferometric radiometer the targets of interest should be located in the Far Field (FF) range of the array [63]. For close-range operation, a Near-to-Far-Field correction is proposed in [64] [65] to use the Fast Fourier Transform (FFT) to retrieve images acquired in NF range if a certain degree of distortion at the edges of the FoV is allowed. It is considered that the scene is in the NF of the array if the distance between the array and the scene is $r < 2D_a^2/\lambda$, where D_a is the array physical size. The equality is given when the maximum phase error due to the paraxial approximation is $\pi/8$. In this situation, the phase error present in the visibilities should be compensated in order to avoid distortion if an iFFT is used as an image focusing technique. From the measured visibilities in NF V_{kj}^{NF}, an estimation of the FF visibilities is given by

$$\widehat{V}_{kj}^{\mathrm{FF}} = V_{kj}^{\mathrm{NF}} e^{-jk_0(r_k - r_j)} e^{-j2\pi(u\xi + v\eta)}. \tag{3.1}$$

The correction consists of a phase compensation introduced by the term $e^{-jk_0(r_k - r_j)}$, where r_i is the distance from the antenna "i" to the center pixel of the image. Hence, by using this correction, the center pixel is properly focused whereas the focusing level is decreased as the pixels are further from the center. Note that the target is in the FF of any single antenna

element in the array and close-range distortion is exclusively caused by non-paraxial imaging and by the projection of the screener beams on the image plane.

The following points apply the formulation for 2D-SA, 1D-SA and RA radiometers developed in [64] to close-range applications. The general sensitivity equations for the different radiometers are elaborated for a NF geometry. These expressions can be directly compared at an equivalent imaging time (t_s) depending on the system bandwidth, system temperature, scene range and dimensions and required resolution. In order to analyze several radiometer configurations, only boresight radiometric resolution is taken into account.

3.1.1 Single element constraints

Equation (2.41) shows that boresight radiometric resolution is improved by minimizing the single element solid angle Ω_e. However, since off-boresight radiometric resolution is degraded with the antenna pattern, a tradeoff is achieved by constraining this degradation to a maximum factor of 2 when the single element Half-Power Beamwidth (HPBW) matches the FoV. To assess the feasibility of this approach we must notice that the maximum size of a single element in the array is limited by the minimum antenna separation du and dv. In this case, according to (2.32), the single element HPBW for an aperture with uniform fields and size $du \cdot dv$ is given by

$$\Delta\theta_{ex} = \frac{0.88}{du} = 0.88(2\xi_{max}) \quad ; \quad \Delta\theta_{ey} = \frac{0.88}{dv} = 0.88(2\eta_{max}). \tag{3.2}$$

Therefore, in the case of practical antennas the HPBW of the single element antenna can be adapted to the scene FoV by using an aperture slightly smaller than the minimum antenna separation as described by the following expression:

$$L_x \cong 0.88du \qquad L_y \cong 0.88dv \tag{3.3}$$

where L_x and L_y are the aperture dimensions of the single element antenna normalized to the system wavelength.

3.1.2 Particularized radiometric sensitivity

For the sake of simplicity, rectangular tapering, analog correlation and ideal rectangular predetection filtering are considered in (2.41) yielding

$$\Delta T_B = \frac{T_A + T_R}{\sqrt{Bt_s}} du \cdot dv \cdot \Omega_e \sqrt{N_u N_v}, \tag{3.4}$$

where the elemental sampling area given by $\Delta s = du \cdot dv$ has been considered for rectangular sampling. It should be pointed out that according to (3.4) ΔT_B is optimized if the single element solid angle Ω_e is minimized by matching the HPBW of the single element antenna pattern to the FoV.

In the case of a large number of elements in the array, from (2.30) and (2.34) the following equation is obtained

$$du \cdot dv \cong \frac{4u_{max}v_{max}}{N_u N_v} \cong \frac{1}{N_u N_v} \frac{4 \cdot 0.60^2}{\Delta\theta_x \Delta\theta_y}. \tag{3.5}$$

Now, if the synthesized solid angle is approximated by the product of the HPBW in the two orthogonal directions, $\Omega_{\text{syn}} \cong \Delta\theta_{\text{x}}\Delta\theta_{\text{y}}$, and taking into account the relationship between solid angle and effective area ($\Omega_{\text{syn}}/\Omega_{\text{e}} = A_{\text{e}}/A_{\text{syn}}$) the following expression is obtained

$$\Delta T_{\text{B}} = 0.72\frac{T_{\text{A}} + T_{\text{R}}}{\sqrt{Bt_{\text{s}}}}\frac{A_{\text{syn}}}{A_{\text{e}}}\frac{1}{\sqrt{N_{\text{mu}}N_{\text{mv}}}}, \tag{3.6}$$

where A_{syn} and A_{e} are the effective areas of the synthetic aperture and the single element aperture. Note that (3.6) is consistent with the approximate expression usually found in the literature [66], where the number of measured visibility samples $N_{\text{mu}} \cdot N_{\text{mv}} = N_{\text{u}} \cdot N_{\text{v}}/4$ is used (the Hermitian visibility samples are not taken into account).

3.1.3 2D synthetic aperture interferometric radiometer

In order to obtain the NF sensitivity expression, (3.4) is transformed using the following parameters:

- Boresight spatial resolution in x: $\Delta x = r\Delta\theta_{\text{x}} \cong r\Delta\xi$

- Boresight spatial resolution in y: $\Delta y = r\Delta\theta_{\text{y}} \cong r\Delta\eta$

- Target size along x: $2\xi_{\max} = 2\sin(\arctan(\frac{W}{r}))$

- Target size along y: $2\eta_{\max} = 2\sin(\arctan(\frac{H}{r}))$

Since the synthesized image is computed as the FFT of the visibility samples, if Fourier interpolation is not used, the number of independent pixels in the synthesized image (N_{px} and N_{py}) is coincident with the number of visibility samples (N_{vx} and N_{vy}). In order to take into account the smearing of the image, the relation between the Effective Field of View (EFoV) and the Instantaneous Field of View (IFoV) is considered for the computation of the number of pixels.

The angular resolution ($\Delta\theta_{\text{x}}$ and $\Delta\theta_{\text{y}}$) is approximated by the increment of the direction cosines ($\Delta\xi$ and $\Delta\eta$) at boresight. If the single element HPBW matches the FoV: $\Omega_{\text{e}} \cong \Delta\theta_{\text{ex}}\Delta\theta_{\text{ey}} \cong 2\xi_{\max}2\eta_{\max}$ and $\Omega_{\text{e}}\Delta s = 1$. Thus if the NF distortion can be neglected ΔT_{B} is independent on the imaging range as presented in point 3.1.6 and depends on the receiver parameters, the scene dimensions and the spatial resolution. Furthermore, as the antenna separation is also adapted to the FoV, the spatial resolution for a given number of antennas is approximately maintained independent of the range. Due to the pixel overlapping of the synthesized images given as a result of (2.35) and (2.36), the number of pixels related with the FoV and the spatial resolution is

$$N_{\text{u}} = N_{\text{px}} = 1.2\frac{2\xi_{\max}}{\Delta\theta_{\text{x}}} + 1 \approx 1.2\frac{2\xi_{\max}}{\Delta\theta_{\text{x}}}; \tag{3.7}$$

$$N_{\text{v}} = N_{\text{py}} = 1.2\frac{2\eta_{\max}}{\Delta\theta_{\text{y}}} + 1 \approx 1.2\frac{2\eta_{\max}}{\Delta\theta_{\text{y}}}. \tag{3.8}$$

By substituting the aforementioned parameters in (3.4) the resulting expression is

$$\Delta T_{2D}^{NF} = 2.4 \frac{T_{sys}}{\sqrt{Bt_s}} \frac{\arctan(\frac{W}{r})\arctan(\frac{H}{r})}{\sin(\arctan(\frac{W}{r}))\sin(\arctan(\frac{H}{r}))} \sqrt{\frac{\sin(\arctan(\frac{W}{r}))}{\frac{\Delta x}{r}} \frac{\sin(\arctan(\frac{H}{r}))}{\frac{\Delta y}{r}}}.$$
(3.9)

3.1.4   1D synthetic aperture interferometric radiometer

A 1D-SA radiometer that performs synthetic imaging in the vertical direction y and real aperture in horizontal direction x is studied. The 1D-SA radiometer must acquire a vertical line of pixels in $t_i = t_s/N_{px}$ seconds in order to have a 2D image in t_s seconds. In this case, the radiometric resolution is approximated by the following expression

$$\Delta T_B = \frac{T_A + T_R}{\sqrt{Bt_s}} \Delta\theta_y dv \sqrt{N_v N_{px}}.$$
(3.10)

The following equation is obtained if the parameters of (3.10) are transformed to consider the NF geometry

$$\Delta T_{1D}^{NF} = \sqrt{4.8} \frac{T_{sys}}{\sqrt{Bt_s}} \frac{\arctan(\frac{H}{r})}{\sin(\arctan(\frac{H}{r}))} \sqrt{\frac{\arctan(\frac{W}{r})}{\frac{\Delta x}{r}} \frac{\sin(\arctan(\frac{H}{r}))}{\frac{\Delta y}{r}}} \sqrt{\frac{EFOV}{IFOV}}.$$
(3.11)

As in the 2D-SA case, the single element HPBW must match the FoV and the antenna separation dv is adjusted to the image FoV ($dv = (2\eta_{max})^{-1}$). The number of mechanically scanned pixels depends on the scene distance for close-range imaging resulting in

$$N_{px} = \frac{2\arctan\left(\frac{W}{r}\right)}{\frac{\Delta x}{r}} \frac{EFOV}{IFOV}.$$
(3.12)

3.1.5   Real aperture radiometer

A system based on a single receiver radiometer with a beam-scanning antenna system has been considered for the RA screener configuration. In this case if $N_{px} \cdot N_{py}$ pixels are imaged in t_s seconds, the integration time for each pixel t_i must be reduced accordingly, yielding a radiometric sensitivity

$$\Delta T_B = \frac{T_A + T_R}{\sqrt{Bt_s}} \sqrt{N_{px} N_{py}}.$$
(3.13)

Taking into account the number of pixels in NF, (3.13) develops into

$$\Delta T_{RA}^{NF} = \frac{T_{sys}}{\sqrt{Bt_s}} \sqrt{\frac{2\arctan(\frac{W}{r})}{\frac{\Delta x}{r}} \frac{2\arctan(\frac{H}{r})}{\frac{\Delta y}{r}} \frac{EFOV}{IFOV}}.$$
(3.14)

3.1.6   Far field radiometric sensitivity

In the FF screening range $(r \gg W, H)$, the trigonometric functions of (3.9), (3.11) and (3.14) can be approximated by the angles, yielding the following expression

$$\Delta T_{\mathrm{B}}^{\mathrm{FF}} = \frac{T_{\mathrm{A}} + T_{\mathrm{R}}}{\sqrt{Bt_{\mathrm{s}}}} \sqrt{\frac{2W}{\Delta x} \frac{2H}{\Delta y} \frac{\mathrm{EFOV}}{\mathrm{IFOV}}}. \tag{3.15}$$

Hence, the radiometric sensitivity ΔT_{B} in the FF range tends to the same value for the three studied systems. Note that the Interferometric Radiometer Uncertainty Principle derived in [61] can be translated to the screener case by the following expression

$$\Delta T_{\mathrm{B}} \cdot \Delta x \cdot \sqrt{t_{\mathrm{s}}} = \frac{T_{\mathrm{sys}}}{\sqrt{B}} \frac{\mathrm{EFOV}}{\mathrm{IFOV}} 2\sqrt{WH}. \tag{3.16}$$

The performance parameters have been grouped in the left hand side of the equation whereas the system parameters are in the right hand side. A clear tradeoff between spatial resolution and radiometric sensitivity is shown in the expression.

3.2   Screener design parameters

In the following sections the expressions derived in section 3.1 are compared depending on several parameters. Additionally, a sparse array configuration is described for the 1D-SA radiometer. It should be pointed out that time delays caused by mechanical movements have been neglected in the comparison.

3.2.1   Radiometric sensitivity comparison

The radiometric sensitivity ΔT_{B} describes the capacity of the radiometer to distinguish among small scene contrasts in the image and hence, the capacity of detecting concealed objects with an apparent temperature similar to the background. The three radiometer systems are compared with similar front-end characteristics: $T_{\mathrm{R}} = 300\,\mathrm{K}$ (3 dB noise figure), $T_{\mathrm{A}} = 300\,\mathrm{K}$, $B = 500\,\mathrm{MHz}$, $\Delta x = \Delta y = 3\,\mathrm{cm}$, and a target size $2H = 180\,\mathrm{cm}$ and $2W = 90\,\mathrm{cm}$ (Fig.3.1). A relation between EFoV and IFoV is chosen as EFoV $= 1.2$IFoV for mechanical scanning to compare all systems in equal smearing conditions. These parameters will be used in the following points to compare the different radiometer architectures unless otherwise noted.

Figure 3.2(a) shows the variation of ΔT_{B} with the imaging time calculated with (3.9), (3.11) and (3.14) at a range $r = 1.25\,\mathrm{m}$. In this particular case, $\xi_{\max} = 0.33$ and $\eta_{\max} = 0.58$ yielding an antenna separation of $du = 1.51$ and $dv = 0.86$. The spatial resolution sets $u_{\max} = v_{\max} = 25$ and the number of pixels $N_{\mathrm{u}} = 34$ and $N_{\mathrm{v}} = 59$. The result is similar for the three radiometers and shows that with the studied system configuration the radiometric sensitivity is below $1.5\,\mathrm{K}$ for an image acquisition time of $1\,\mathrm{s}$ at a bandwidth of $500\,\mathrm{MHz}$. Sub-second imaging or improved radiometric sensitivity requires larger pre-detection bandwidth (e.g. $B = 2\,\mathrm{GHz}$).
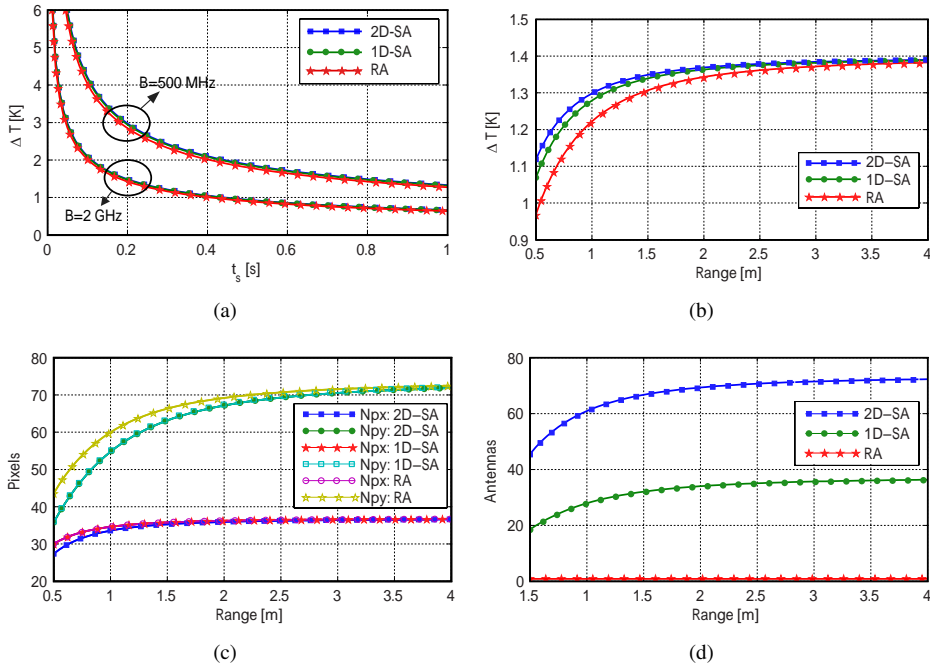
Figure 3.2: (a) Radiometric sensitivity against integration time and bandwidth of the radiometers. Sub-second imaging and sub-Kelvin sensitivity requires a large bandwidth. (b) Radiometric sensitivity depending on the scene distance from the radiometer. (c) Number of pixels in the image for the different studied radiometers. (d) Number of antennas required to fulfill the FoV and spatial resolution specifications depending on the scene range.

The range dependance of the radiometric sensitivity in passive NF imaging is pointed out in Fig. 3.2(b). For the aforementioned system characteristics and for a range between 0.5 and 2 meters the sensitivity is dependent on the range. For a range larger than 2 meters the sensitivity tends to a value of $1.4\,\mathrm{K}$, close to the FF value. The variation of the sensitivity in the NF range is due to the reduction of the number of pixels needed to acquire the image as presented in Fig. 3.2(c). This effect occurs since the projection of the beam on the scene degrades the spatial resolution at the edges and therefore the number of pixels required to fill the scene is reduced. Furthermore, as the number of pixels is reduced, the number of antennas is as well reduced in the case of the interferometric radiometers as shown in Fig. 3.2(d). Further discussion of NF distortion effects are carried out is section 3.3.2.

Table 3.1 shows a comparison made according to a similar front-end configuration at $1.25\,\mathrm{m}$ range with $3\,\mathrm{cm}$ of spatial resolution. The RA screener needs one receiver antenna with an area of approximately $177\,\mathrm{cm}^2$ to obtain the desired spatial resolution whilst the 1D filled (*) interferometric array is composed by 31 antennas of $3.4\,\mathrm{cm}^2$ and the 2D array contains 65 antennas with an area of $0.13\,\mathrm{cm}^2$. The parameters specified for a 1D (**) array represent the performance of an array thinned to 10 antennas. The compared systems have nearly the same radiometric sensitivity if they are optimized for a specific range as shown in Table 3.1.

	$\Delta T_{\mathrm{B}}[\,\mathrm{K}]$	N_{px}	N_{py}	N_{vx}	N_{vy}	N_{ant}	$A_{\mathrm{e}}(\,\mathrm{cm}^2)$
RA	1.26	35	64	0	0	1	176.83
1D (*)	1.31	35	60	0	60	31	3.40
1D (**)	1.31	35	60	0	60	10	3.40
2D	1.33	35	60	35	60	65	0.13

(*) Filled array. In this case the baselines are highly redundant.
(**) Thinned array. In this case the 1D-SA array has been thinned to 10 antennas.

Table 3.1: Screener comparison for similar front-end configuration
$r = 1.25\,\mathrm{m}$, $\Delta x = 3\,\mathrm{cm}$, $B = 500\,\mathrm{MHz}$, $t_s = 1\,\mathrm{s}$, $T_{\mathrm{sys}} = 600\,\mathrm{K}$
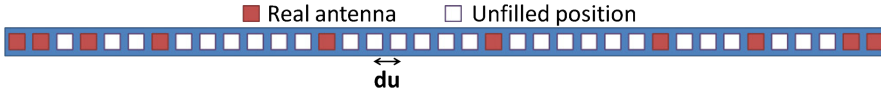
Figure 3.3: Schematic of the antenna disposition in a sparse array composed of 10 antennas that synthesizes 37 visibilities ($u_{\max} = 36du$) [67].
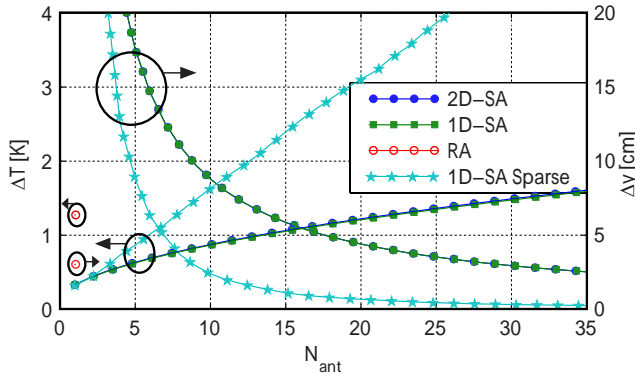
Figure 3.4: Comparison depending on the number of antennas N_{ant} of the radiometric sensitivity ΔT and spatial resolution along the y-axis Δy of the 2D-SA, 1D-SA, RA and 1D-SA sparse radiometers. The calculation has been performed with the following system parameters: $t_s = 1$, $\Delta x = 3\,\mathrm{cm}$, $B = 500\,\mathrm{MHz}$, $H = 90\,\mathrm{cm}$, $W = 45\,\mathrm{cm}$. $r = 125\,\mathrm{cm}$ and $T_{\mathrm{sys}} = 600\,\mathrm{K}$.

3.2.2 1D-SA sparse array

The main advantage of the 1D-SA is that the redundancy in the visibilities is greatly reduced by using a thinned array with a minimum redundancy as described in [67]. In order to make a comparison with the T-shape array, the number of antennas in each of the arms of a 2D-SA sensor (Fig. 2.15) can be directly related to the number of visibility samples $N_{\mathrm{vx}} \cdot N_{\mathrm{vy}}$ used to synthesize an image

$$N_{\mathrm{ax}} = N_{\mathrm{vx}} \quad ; \quad N_{\mathrm{ay}} = \frac{1}{2}(N_{\mathrm{vy}} - 1). \tag{3.17}$$

If a 1D-SA sparse array is used to synthesize the image in the y direction, the larger baseline needed to have the same number of visibility samples (pixels) as in the T-shape case is

Sensor type	$\Delta y \cong 3\,\mathrm{cm}$	$\Delta y \cong 2\,\mathrm{cm}$	$\Delta y \cong 1\,\mathrm{cm}$
2D-SA T-shape	66	99	197
1D-SA sparse	10	12	17

Table 3.2: Number of antennas for a given boresight spatial resolution
Target size: $2H = 180\,\mathrm{cm}$, $2W = 90\,\mathrm{cm}$ at $r = 125\,\mathrm{cm}$
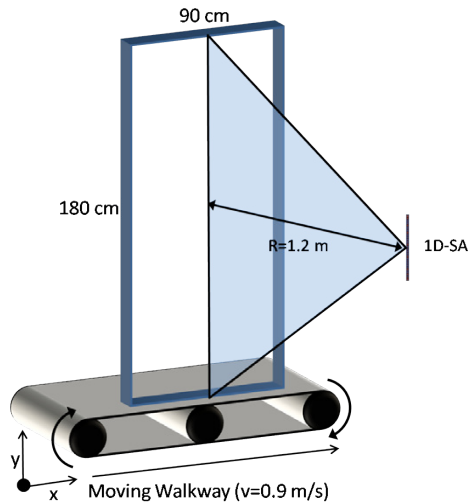
Figure 3.5: Proposed imaging setup based on a 1D-SA radiometer. The vertical pixels are synthesized by the radiometers whereas the horizontal are obtained by translating the scenario using a moving walkway.

$v_{\mathrm{max}} = 0.5(N_{\mathrm{vy}} + 1)$, which gives the number of required antennas in the thinned array [19]. As an example, Fig. 3.3 shows the antenna arrangement of the sparse array with 10 antennas where, in order to minimize the effect of NF distortion, the thinned array with better symmetry has been selected. A comparison of the spatial resolution Δy and radiometric sensitivity ΔT among the studied radiometers is shown in Fig. 3.4 depending on the number of antennas N_{ant}. It is shown that the one-dimensional sparse array has an improved spatial resolution with respect the 2D-SA and the 1D-SA for the same N_{ant}. Nevertheless, the radiometric sensitivity is reduced for equivalent number of antennas. Table 3.2 gives the number of antennas required in the two cases to yield the same spatial resolution in the synthesized direction. As spatial resolution gets more stringent 1D-SA thinned arrays lead to a drastic reduction of the number of antennas with relation to a 2D-SA sensor.

3.2.3 1D-SA screener with moving walkway

A screener system based on a 1D interferometric radiometer is proposed working at $94\,\mathrm{GHz}$ consisting of a vertical thinned linear array of 10 antennas as the one explained in section 3.2.2. The radiometer array is used as a static imaging sensor whereas a moving walkway translates the person in the horizontal direction. In this case, no moving mechanical parts

	ADVANTAGES	**DRAWBACKS**
RA	Use of direct detection receivers No degradation of ΔT at the image edges Simple signal processing	Requires mechanical scanning Large single element antenna Aiming problems in non-stable environments
1D-SA	1D images obtained in single acquisition Thinned arrays can be used Visibility redundancy can be minimized	IF processing of large bandwidth signals 1-D mechanical movement needed Heterodyne receivers
2D-SA	A 2D image obtained in a single acquisition ΔT improved by averaging redundancy No mechanical movement needed	IF processing of a large amount of correlations Large number of receivers required Heterodyne receivers

Table 3.3: Advantages and drawbacks of the radiometer configurations for close-range screening purposes

in the screener are needed, reducing the design dimensions and cost. Figure 3.5 shows the imaging setup describing the main geometrical parameters. A distance between the imaging sensor and the scene has been chosen to be $1.25\,\mathrm{m}$ as a tradeoff in order to avoid the pixel distortion on the edges ($\Delta x_{\max} = 1.22\Delta x$) but still maintaining a small array ($100\,\mathrm{mm}$ length). If the speed of the moving walkway is fixed to $0.5\,\mathrm{m/s}$, the required time to acquire an image is fixed to 1.8 seconds. In this case, if a receiver with a $T_{\mathrm{sys}} = 600\,\mathrm{K}$ and a predetection bandwidth of $500\,\mathrm{MHz}$ is considered, the resulting ΔT from (3.11) is $1.4\,\mathrm{K}$. The angular resolution is obtained from (2.30) giving $\Delta\theta_{\mathrm{y}} = 0.96\,^\circ$ at boresight ($\Delta_y = 2\,\mathrm{cm}$).

In this proposed system, additional focusing in the horizontal axis is needed to provide the required angular resolution in this direction. This can be achieved by using a cylindrical reflector with an aperture dimension of $D = 1.2\frac{\lambda}{\Delta\theta_{\mathrm{x}}} = 220\,\mathrm{cm}$.

3.3 Screener performance

Table 3.1 summarizes the performance of the different sensor configurations described so far in order to show the feasibility of close-range radiometric screening with relatively small antenna size and reasonable receiver characteristics. Since the most suitable configuration will depend, to a large extent, on the application and the environment, the following sections are devoted to highlight the limitations and improvement paths in the case of synthetic apertures. Additionally, Table 3.3 summarizes the advantages and drawbacks of each radiometer system when used in a screener system.

3.3.1 Spatial/Radiometric resolution tradeoff

The tradeoff between the spatial and the radiometric resolutions when assessing the object detection capabilities of a passive screener system is described in this section. The temperature contrasts in a certain beam projection on the scene are averaged. Therefore, an object with smaller dimensions than the spatial resolution can be detected if the averaged pixel temperature differs with the contiguous pixels with a value greater than the radiometric sensitivity.
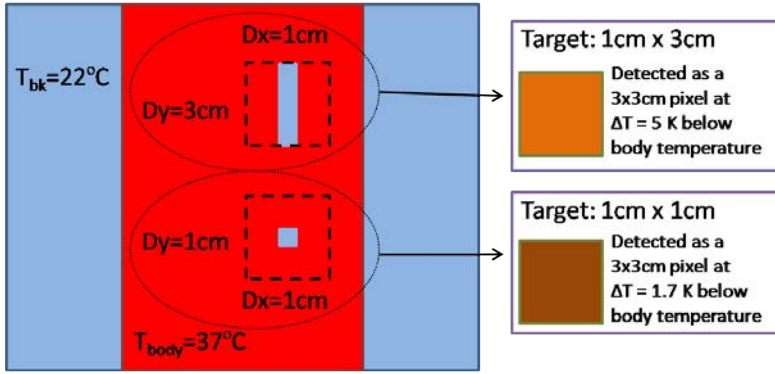
Figure 3.6: Schematic depicting the tradeoff between the spatial resolution and radiometric sensitivity in the object detection problem for an ideal reflective target.

Nevertheless, it should be pointed out that two objects separated with a distance less than the spatial resolution will be detected only as a one object.

Figure 3.6 shows a simplified schematic example of a scene consisting on a person at a physical temperature of $37\,^{\circ}$C in front of a background being at $22\,^{\circ}$C (considering that both have an emissivity of 1). Two metallic objects with different dimensions are placed on the person reflecting the background temperature. A differential passive imaging system with a spatial resolution of $3\,$cm detects the 1x3 cm object as a 3x3 cm spot with an apparent temperature of $5\,$K below the body temperature. In the case of the 1x1 cm object, it is detected as a 3x3 cm spot at $1.7\,$K below the body temperature.

Hence, an object with smaller dimensions than the spatial resolution of the system can be detected if the radiometric sensitivity level is below the value given by

$$\Delta T_B < (T_{\text{body}} - T_{\text{bk}})\frac{Dx \cdot Dy}{\Delta x \cdot \Delta y}, \tag{3.18}$$

where $DxxDy$ are the object dimensions. Note that for equal spatial resolution on the two dimensions, the radiometric sensitivity requirement is inversely proportional to Δx^2 and gets dramatically stringent at sub-centimetric resolution.

3.3.2   Off-axis performance degradation

Synthetic Aperture (SA) interferometric radiometers have two sources of NF distortion: 1) the beam projection on the image plane; and 2) the paraxial approximation assumed when reconstructing the temperature image from the visibilities applying an iFFT.

The first source of distortion produces a degradation of the spatial resolution at the edges Δx_{max} with relation to the boresight value Δx_0 given by

$$\frac{\Delta x_{\text{max}}}{\Delta x_0} = \frac{1}{\cos^2\left(\arctan\left(\frac{W}{r}\right)\right)} \tag{3.19}$$

as a function of the range and target size (Fig. 3.7(a)). For distances below $2\,$m the spatial resolution at the edges is deteriorated in the x- and y-axes. This effect causes a blurring

(a)   (b)
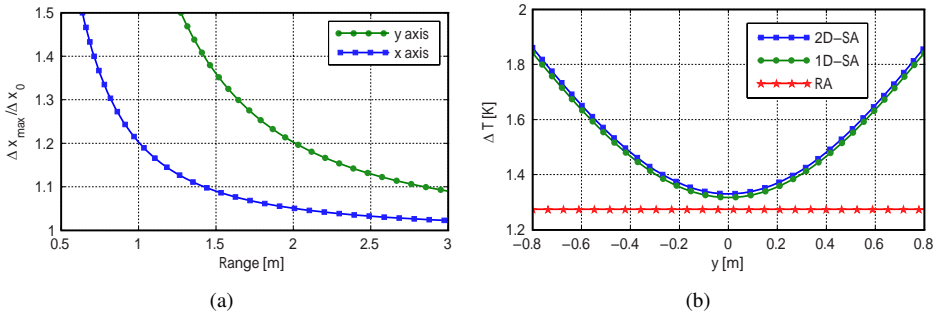
Figure 3.7: (a) Spatial resolution degradation at the edge of the FoV due to NF distortion. (b) Variation of the radiometric resolution $\Delta T_{\rm B}$ along y-axis of the image for the three screener configurations. The curves have been calculated with (2.41) and (3.14).

(a)   (b)
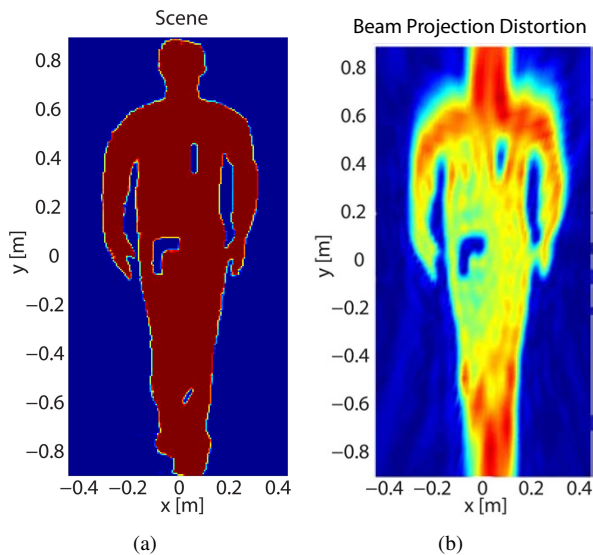
Figure 3.8: 2D Screener simulation at $f_0 = 94\,{\rm GHz}$ and $r = 0.6$ m applying the NF to FF correction. Decorrelation effects are neglected. (a) Scene with a 90x180 cm^2 target consisting on an person with metallic objects of the following dimensions: 1) 4x10 cm^2 in the chest; 2) an L-shape object with 5 cm width in the waist and 3) 3x5 cm^2 in the ankle. The person has a differential temperature of 15 K with respect the background. (b) Reconstructed image showing the effect of the beam projection distortion at the edges.

of the image at the edges. Nevertheless, in a typical imaging scenario, the information is concentrated at the center of the scene, and some distortion of the pixels at the borders of the image can be allowed. Moreover, in the case of the interferometric radiometers the $\Delta T_{\rm B}$ is also decreased in the edges as shown in Fig. 3.7(b). The dependence of $\Delta T_{\rm B}$ with the pixel position is also shown in Fig. 2.17. Note that in the case of the RA radiometer, the radiometric sensitivity does not vary along the axis. The conjunction of these two distortion
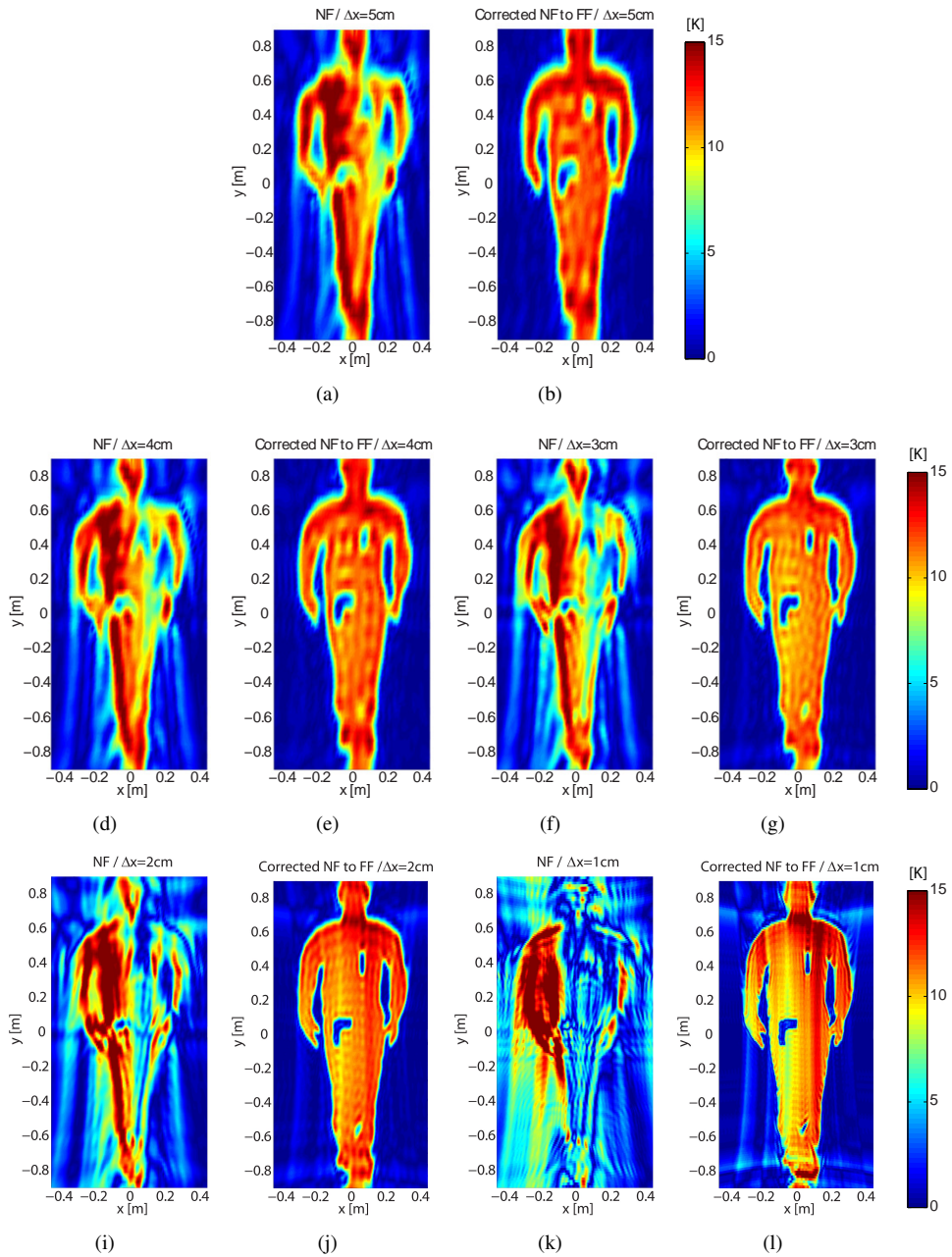
Figure 3.9: 2D Screener simulations of the scene shown in Fig. 3.8(a) with $r = 1.2\,\mathrm{m}$. Decorrelation effects are neglected. (a) Scene consisting on an person with metallic objects of the following dimensions: 1) $4\mathrm{x}10\,\mathrm{cm}^2$ in the chest; 2) an L-shape object with $5\,\mathrm{cm}$ width in the waist and 3) $3\mathrm{x}5\,\mathrm{cm}^2$ in the ankle. The person has a differential temperature of $15\,\mathrm{K}$ with respect the background. Figures (a)(d)(f) (i)(k) are retrieved differential images using standard iFFT with a boresight HPBW $\Delta x = \Delta y = \{5, 4, 3, 2, 1\}\,\mathrm{cm}$ respectively. The objects 1) and 3) cannot be detected due to NF distortion. Figures (b)(e)(g)(j)(l) are retrieved images after NF to FF correction with a boresight HPBW $\Delta x = \Delta y = \{5, 4, 3, 2, 1\}\,\mathrm{cm}$ respectively.
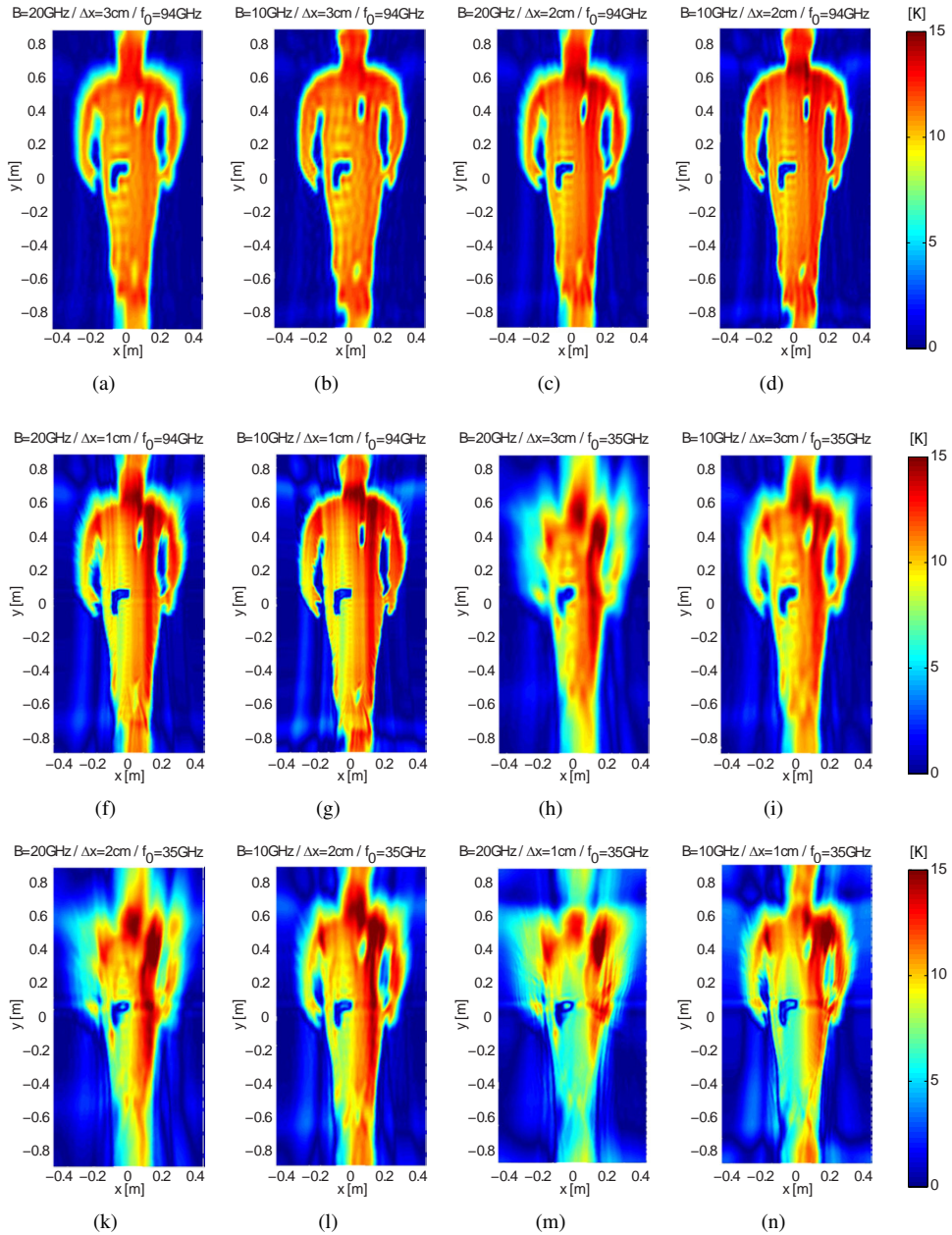
Figure 3.10: 2D Screener simulations of the scene shown in Fig. 3.8(a) with $r = 1.2$ m. Decorrelation effects are taken into account. The simulations have been performed at two center frequencies $f_0 = \{94, 35\}$ GHz and two RF bandwidths $B = \{10, 20\}$ GHz. The differential images reconstructed at $f_0 = 94$ GHz are: (a)(c)(f) with $B = 20$ GHz and $\Delta x = \Delta y = \{3, 2, 1\}$ cm respectively; (b)(d)(g) with $B = 10$ GHz and $\Delta x = \Delta y = \{3, 2, 1\}$ cm respectively. The results at $f_0 = 35$ GHz are: (h)(k)(m) with $B = 20$ GHz and $\Delta x = \Delta y = \{3, 2, 1\}$ cm respectively;(i)(l)(n) with $B = 10$ GHz and $\Delta x = \Delta y = \{3, 2, 1\}$ cm respectively.

effects produced by the beam projection on the image plane reduces the detection capability of the system at the edges. Figure 3.8(b) shows the distortion produced by the beam projection on a reconstructed image at $r = 0.6\,\mathrm{m}$, where the NF to FF correction has been applied. The edges of the image are affected by a blurring caused by a increment of the pixel dimension. The object placed in the ankle cannot be detected due to the distortion. In the case that this distortion level is unacceptable for the screener application, the radiometer should be placed at a further range, thus implying an increment of size of the imaging array.

The second source of distortion is the assumption of the paraxial approximation in the reconstruction of the image. This assumption produces a phase error when imaging at close-range that should be corrected to properly reconstruct the image [64] [65]. Figure 3.9 is devoted to better illustrate the distortion effects produced in the close-range imaging. The effect predominating in the images appearing in the figure is the one produced by the paraxial approximation. An scenario with dimensions $2W = 90\,\mathrm{cm}$ and $2H = 180\,\mathrm{cm}$ has been used as a reference target to foresee the distortion produced by using standard interferometric techniques in the NF range. The scene contains a person at a differential temperature of $15\,\mathrm{K}$ with respect the background. The person carries 3 metallic objects with different dimensions: 1) $4\mathrm{x}10\,\mathrm{cm}^2$ in the chest; 2) an L-shape object with $5\,\mathrm{cm}$ width in the waist and 3) $3\mathrm{x}5\,\mathrm{cm}^2$ in the ankle. Figures 3.9(a)(d)(f) (i)(k) are retrieved differential images using standard iFFT with a boresight HPBW $\Delta x = \Delta y = \{5, 4, 3, 2, 1\}\,\mathrm{cm}$ respectively. It can be appreciated that, as the spatial resolution is improved, the distortion is aggravated. This is due to the array enlargement needed to achieve the required resolution. Hence, if the array is larger, the phase error related to the paraxial approximation is increased. The phase error produces a distorted image not suitable for identification of concealed objects.

Figures 3.9(b)(e)(g)(j)(l) are retrieved images after NF to FF correction with a boresight HPBW $\Delta x = \Delta y = \{5, 4, 3, 2, 1\}\,\mathrm{cm}$ respectively. The reconstructed images after NF to FF shows a reduced level of distortion an are suitable to detect the objects, nevertheless the distortion level is increased at the edges as the spatial resolution is improved. The distortion correction capabilities are reduced when the array dimensions are increased to improve the spatial resolution. Hence, the Fig. 3.9(g) shows less distortion than 3.9(l). The results presented in Fig. 3.9 also show the detection capabilities depending on the spatial resolution. In Fig. 3.9(b), with $\Delta x = \Delta y = 5\,\mathrm{cm}$ the object concealed in the ankle cannot be detected due to a lack of spatial resolution. However, in Fig. 3.9(l) the object is clearly identified.

3.3.3 Decorrelation effects

Section 3.3.4 will show that a large predetection bandwidth B is required to significantly improve the performance of the screener with relation to the example described in Table 3.1. However, although analog correlation allows very large bandwidth, decorrelation may degrade off-axis spatial resolution. Simulation of the NF visibilities in Fig. 3.10 has included the impact of decorrelation when an ideal rectangular bandpass filter in each receiver is taken into account. In this case, the fringe washing function for the baseline (u, v) given by a pair of receivers "k" and "j" has been modeled as:

$$r_{kj}(\tau_{\mathrm{d}}) = \mathrm{sinc}\left(\frac{B}{c_0}(r_k - r_j)\right) \qquad (3.20)$$

where the delay τ_{d} between the radiation collected by antennas k and j is direction dependent, $c_0 = 3 \cdot 10^8 \, \mathrm{m/s}$ and $r_{k,j}$ the distance of each pixel in the image to antennas k and j respectively. Figure 3.10 shows the impact of decorrelation effects in the reconstructed image for all combinations of $f_0 = \{94, 35\} \, \mathrm{GHz}$, $\Delta x = \Delta y = \{3, 2, 1\} \, \mathrm{cm}$ and $B = \{10, 20\} \, \mathrm{GHz}$. For $f_0 = 94 \, \mathrm{GHz}$, the impact of decorrelation is negligible for predetection bandwidths of $B = 10 \, \mathrm{GHz}$. However, the effects are noticeable for $B = 20 \, \mathrm{GHz}$, mainly if $\Delta x = \Delta y = 1 \, \mathrm{cm}$. For $f_0 = 35 \, \mathrm{GHz}$, the decorrelation effects seriously impact the image, hindering the detection of objects at the edges of the image.At lower frequency bands the decorrelation impact of pre-detection bandwidth is higher due to the larger size of the array. This result justify that in order to avoid the NF distortion in the image Millimeter-Wave (mmW) frequency bands should be selected for close-range imaging.

3.3.4 Improved performance

The results presented in Table 3.1 and Fig. 3.9 are related to a quite simple sensor design to show, as a first approach, the main performance parameters of a close-range screener. However, the enhanced performance that some applications may require can be achieved on penalty of higher cost and complexity. The improvement of any of the performance parameters of (3.16), while keeping constant the others, can only be achieved by improving the system parameters in the right hand side of the equation:

- *System temperature*. Since the antenna temperature is fixed to $T_{\mathrm{A}} \cong 300 \, \mathrm{K}$, system temperature can only be significantly improved if a cryogenic front end, either passive or active, is foreseen to reduce $T_{\mathrm{R}} = 300 \, \mathrm{K}$. The theoretical maximum improvement factor in the $\Delta T_{\mathrm{B}} \cdot \Delta x \cdot \sqrt{t_{\mathrm{s}}}$ product is 2 when $T_{\mathrm{R}} = 0 \, \mathrm{K}$.

- *Predetection bandwidth*. B can be greatly increased if analog correlation, IF channelization or a combination of both is taken into account. The simulation in the previous section has shown that very large predetection bandwidths are feasible with negligible decorrelation effects in the W-band. If an effective bandwidth $B = 10 \, \mathrm{GHz}$ is used the sensor parameters would be improved by a factor of 4.5 with respect the curves shown in section 3.2.1.

- *Redundancy*. The radiometric resolution expressions given in [61] and [66] do not take into account any level of redundancy. Two baselines are said to be redundant one with the other when the distance and the direction of the two receivers involved in each one of the two baselines are the same. Unfortunately, the level of redundancy in 2D arrays is marginal (only in the direction of the axis). On the other hand, 1D-AS arrays have a large degree of redundancy but can be thinned to a large extent to minimize the number of antennas. Therefore, the most direct way to reduce radiometric noise by averaging simultaneous independent measurements is by replicating the whole sensor. This is particularly efficient in the case of 1D-SA sparse array.

  For instance in Table 3.1 2D-SA and 1D-SA sparse sensors require 65 and 10 antennas respectively to achieve the same radiometric resolution ($\Delta T_{\mathrm{B}} = 1.3 \, \mathrm{K}$). If 6 1D-SA sparse arrays are placed together pointing to the same pixel (or adjacent pixels in the mechanically scanned direction), radiometric resolution is improved by a factor $\sqrt{6}$ with relation to the 2D case.

- *Environment*. The absorbers placed in front of the FoV can be cooled down to increase the contrast between reflective targets and the body temperature. For instance, surrounding temperature $T_{\mathrm{ph}} = 12\,^{\circ}\mathrm{C}$ increases the contrast from $15\,\mathrm{K}$ to $25\,\mathrm{K}$ and relaxes ΔT_{B} requirement by a factor 1.7.

3.4   Conclusion

The theoretical framework developed in [66] for 1D, 2D and RA systems has been applied to analyze the performance and basic constraints of passive interferometric imaging for close-range applications. Close range system parameters have been set as a tradeoff between radiometric sensitivity, imaging rate and boresight spatial resolution, that has been presented as the close-range uncertainty principle. It has been shown that, when compared with the same front end parameters, spatial resolution and imaging rate, 2D-SA, 1D-SA and RA radiometric sensitivity is equivalent and not a driver to select one of the options. However, off-boresight radiometric resolution degrades as a function of $\xi^2 + \eta^2$ in the synthesized cases.

Close attention has been paid to analyze close-range radiometric sensitivity, which is critical to achieve both high imaging rates and good spatial resolution. The accurate radiometric sensitivity expression recently validated within the Soil Moisture and Ocean Salinity (SMOS) project [61] has been used , and its consistency to the approximate formula widely used in passive interferometry [66] has been demonstrated. It has been shown that the optimum performance is achieved when imaging at a fixed range and the HPBW of each single antenna in the array matches the scene FoV. Also, that this condition is always feasible, in a first approach, independently of the imaging geometry and requirements.

Simulations and theoretical analysis have shown that close-range imaging with moderate requirements is feasible with relatively simple front end configurations if some degree of off-axis performance degradation is allowed. Additionally, section 3.3 has discussed the path to achieve more stringent specifications (e.g. $\Delta x \cong 1\,\mathrm{cm}$, $\Delta T_{\mathrm{B}} \cong 1\,\mathrm{K}$ and $t_{\mathrm{s}} \ll 1\,\mathrm{s}$) on the penalty of higher cost and complexity. It is known that mmW screener applications benefits from the penetrating capability of the electromagnetic fields. The simulations in this work has been used to illustrate the main features and constraints of close-range synthetic aperture imaging to show that, due to the small array size, mmW operation also allows for very large predetection bandwidths and close-range configurations to improve radiometric sensitivity while minimizing decorrelation effects and NF distortion.

It can be concluded that an sparse 1D-SA radiometer can be used with a moving walkway to perform personnel screening avoiding mechanical movements with an optimum number of mmW receivers. The performance of this screener in terms of Δx, ΔT and t_{s} is equivalent to the performance of an screener based on a 2D-SA or a 1D-SA radiometer. However, using interferometric radiometers at mmW frequencies is still a challenge due to the required Intermediate Frequency (IF) processing. This conclusion motivates the research presented in chapter 4, where a technique to reduce the complexity of a mmW screener system is described.

One-dimensional Synthetic Aperture Radiometer with Optical Signal Processing

C HAPTER 3 concludes that the one-dimensional sparse interferometric radiometer achieves a good tradeoff between radiometric performance and number of receivers for close-range screening purposes. However, still a major drawback resides on this type of radiometer: the acquisition of multiple correlations of large bandwith signals required to retrieve the visibilities of the scene. This is a huge problem when the bandwith of the signals is on the order of several GHz if traditional techniques such as digital signal correlation or Intermediate Frequency (IF) analog correlation are used [68] [69]. Specifically, if digital correlation technique is chosen, Analog-to-Digital Converters (ADCs) with a sampling frequency of $f_s = 2B$ should be used in order to fulfill Nyquist criteria. Additionally, the correlations are performed in Field Programmable Gate Arrays (FPGAs) that should process the large amount of data incoming from the ADCs. If the bandwidth of the signals are on the order of several GHz, the hardware complexity required by the correlator system is unaffordable since neither FPGAs nor ADCs supporting such large digital speed rate are commercially available.

This chapter describes a method to overcome the problem of routing and correlating all the antenna signal pairs in an interferometric radiometer by upconverting the Radiofrequency (RF) signal to the optical domain. Hence, the relative bandwidth of the modulated signal is small (even with a RF bandwidth consisting of tens of GHz) allowing the use of commercially available components for optical communications (e.g. Distributed Feedback (DFB) lasers, photodiodes, couplers...). In addition, the distribution of the signal is simplified in the optical domain with respect an RF distribution, since multiple optical signals can be guided either by fiber optics or free-space avoiding coupling effects.

The first section of the chapter is devoted to describe the optical modulation and correlation process using LiNbO3 phase modulators. The working principle of the optical modulator is explained with the aim of understanding the characteristics of the modulated optical. Moreover, the resulting expressions for an optical correlation of two radiometric receivers are obtained for two different modulation schemes: 1) Double-Sideband (DSB) and 2) Single-Sideband (SSB) modulations. In the second section of the chapter, the expressions governing
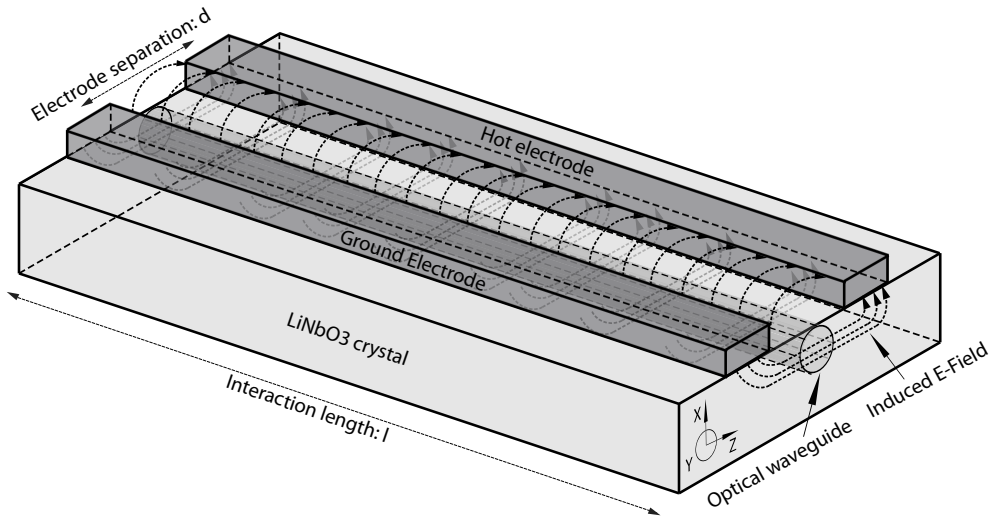
Figure 4.1: Perspective schematic view of an x-cut optical phase modulator where the main parts (RF electrodes, optical waveguide, LiNbO3 crystal...) are depicted.

the method are related with the classical interferometric theory. Both sections are comple-
mented with measurements that confirm the validity of the expressions. Additionally, final
measurements consisting on one-dimentional images are acquired by moving two W-band
radiometric receivers along a line in order to synthesize the required baselines. The third
section is devoted to explain the optical distribution scheme that is able to obtain the signal
combinations between all receiver pairs. Finally, considerations regarding the performance
of the system are discussed at the end of the chapter for both types of optical modulations.[1]

4.1   Optical modulation

In order to up-convert the RF signal to the optical domain, a laser optical source is modulated
by the RF signal. There are mainly three types of commercially available optical modulator:
1) LiNbO3 modulators [70], 2) electro-absorption modulators [71] and 3) the direct modula-
tion of a laser [72]. The study described in this chapter uses LiNbO3 modulators since they
achieve the maximum bandwidth among all the options [73].

4.1.1   LiNbO3 phase modulators

The LiNbO3 optical phase modulators are based in the electro-optical effect that occurs in
the LiNbO3 crystal. If the LiNbO3 crystal is placed between two electrodes, the phase of the
optical signal going through the crystal is modulated by the voltage V between the electrodes

---

[1]The following sections of this chapter may contain verbatim text and figures from [J1] [C3,C4].

as

$$\Delta\Phi = \frac{\pi n_0^3 r V}{\lambda_0}\frac{l}{d}, \tag{4.1}$$

where d is the electrode separation, r is an electro-optic tensor that depends on the polarization of the optical beam, n_0 is the LiNbO3 index of refraction, l is the length of the interaction between the crystal and the optical signal and λ_0 is the optical wavelength. Figure 4.1 shows an schematic of a LiNbO3 phase modulator where the electrodes, the optical waveguide and the direction of the electric field are depicted. The voltage required to produce a phase shift of π is called half-wave voltage V_π. The half-wave voltage is defined by the geometrical characteristics of the modulator and is obtained directly from (4.1) as

$$V_\pi = \frac{\lambda_0}{n_0^3 r}\frac{d}{l}. \tag{4.2}$$

The orientation of the crystal axes with respect the optical waveguides and the electrodes affects to the modulator efficiency and therefore to the half-wave voltage. The electric field should be aligned with the z-axis of the crystal since it is the axis presenting the highest electro-optic coefficient [70]. Figure 4.1 shows an schematic of an x-cut optical phase modulator where it is shown that the electric field created between the electrodes by the RF signal generates an electric field parallel to the z-axis of the crystal. Additionally, LiNbO3 crystals are birefringent and thus their refractive index depend on the polarization of the optical wave. A consequence of the birefringence in the LiNbO3 crystal is that the modulation efficiency of a LiNbO3 modulator also depends on the polarization of the incident optical wave. Hence, an optical polarization control is required to maximize the modulation efficiency.

4.1.2 Optical phase modulation by a CW signal

If an RF Continuous Wave (CW) signal defined by $x(t) = V_0\sin(\omega_m t + \psi)$ is used to modulate a laser beam with and electric field $E(t) = E_0 e^{j(\omega_0 t + \phi_0)}$, the signal coming out of the LiNbO3 modulator is

$$E_{\mathrm{m}}(t) = E_0 e^{j(w_0 t + \phi_0 + m\sin(\omega_m t + \psi))}, \tag{4.3}$$

where $m = \frac{\pi V_0}{V_\pi}$ and $\phi_0 = \frac{2\pi n_0 l}{\lambda_0}$. The term $e^{jm\sin(\omega_m t + \psi)}$ can be decomposed as

$$e^{jm\sin(\omega_m t + \psi)} = \sum_{k=-\infty}^{\infty} J_k(m)e^{jk(\omega_m t + \psi)}, \tag{4.4}$$

where J_k is the Bessel function of the first kind and order k. Therefore the resulting modulated signal spectrum contains multiple sidebands separated ω_m from the optical center frequency ω_0. If the RF signal amplitude fulfils the condition $V_0 \ll V_\pi$, the following approximations can be performed: $J_k(m) \approx 0 \quad \forall\ |k| > 1$, $J_{\pm 1}(m) \approx \pm\frac{m}{2}$ and $J_0(m) \approx 1$. Therefore (4.4) can be expressed as

$$e^{jm\sin(\omega_m t + \psi)} \approx 1 + \frac{m}{2}(e^{j(\omega_m t + \psi)} - e^{-j(\omega_m t + \psi)}), \tag{4.5}$$

where only the carrier and the first sidebands are considered. Introducing (4.5) in (4.3) the optical signal is

$$E_{\mathrm{mod}}(t) \approx E_0 e^{j(\omega_0 t + \phi_0)}\left[1 + jm\sin(\omega_m t + \psi)\right]. \tag{4.6}$$
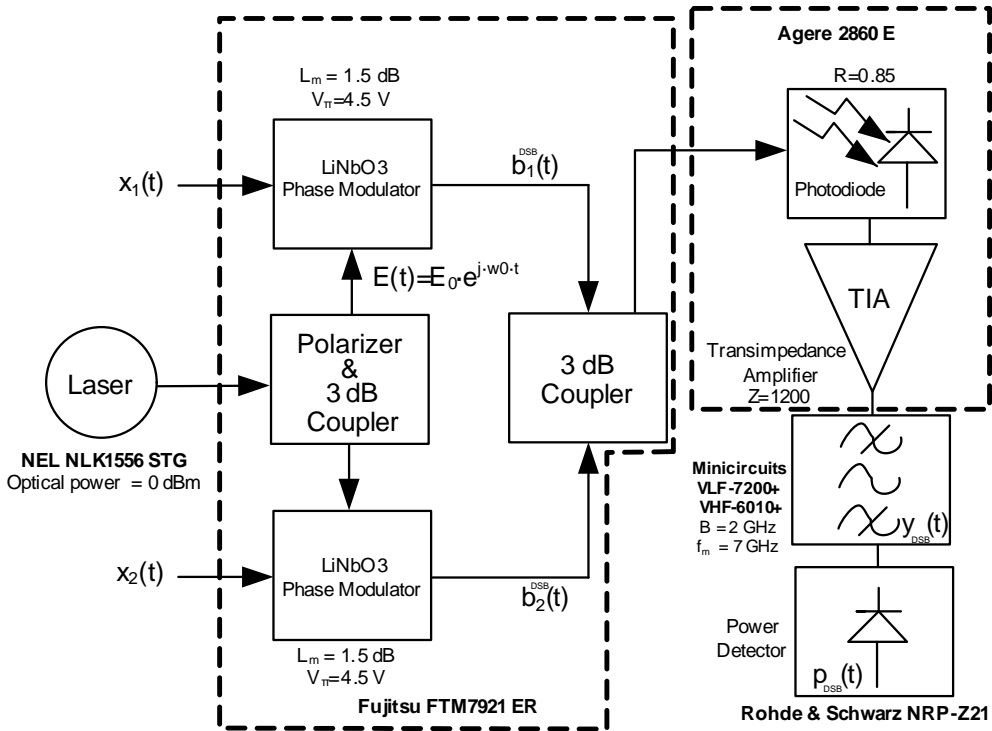
Figure 4.2: Optical modulation and detection schematic for two receivers. The optical signal provided by a laser is modulated by the RF radiometric signals coming from the receivers. Two LiNbO3 modulators are used for this purpose. The DSB modulated signals are added and detected by a photodiode. The resulting photocurrent contains the correlation between both receiver signals. The component model of each part used in the measurement setup is specified.

Equation (4.6) approximates the result of the optical signal phase-modulated by a single RF tone.

4.1.3   Cross-correlation of double-sideband optical modulated signals

Figure 4.2 shows a block diagram of the proposed optical conversion system. The RF signals collected by the antennas in the millimeter-wave band are downconverted to provide $x_{1,2}(t)$ at an IF frequency compatible with the modulation bandwidth of the LiNbO3 phase modulator. The polarization of the optical signal produced by a DFB laser is adjusted by using an optical polarizer to maximize the modulation efficiency of the LiNbO3 modulators as described in the previous section. The optical signals $b_{1,2}^{\mathrm{DSB}}(t)$ have been modulated respectively by the IF radiometric signals $x_{1,2}(t)$ and are combined and detected by a photodiode. The photodetected current is amplified using a Transimpedance Amplifier (TIA) and the power of the resulting signal is measured with a power detector.

Although (4.6) is derived for a single tone, the results are also valid when the modulating signal is band-limited Gaussian noise with a small power [74] [75]. In this case, and going
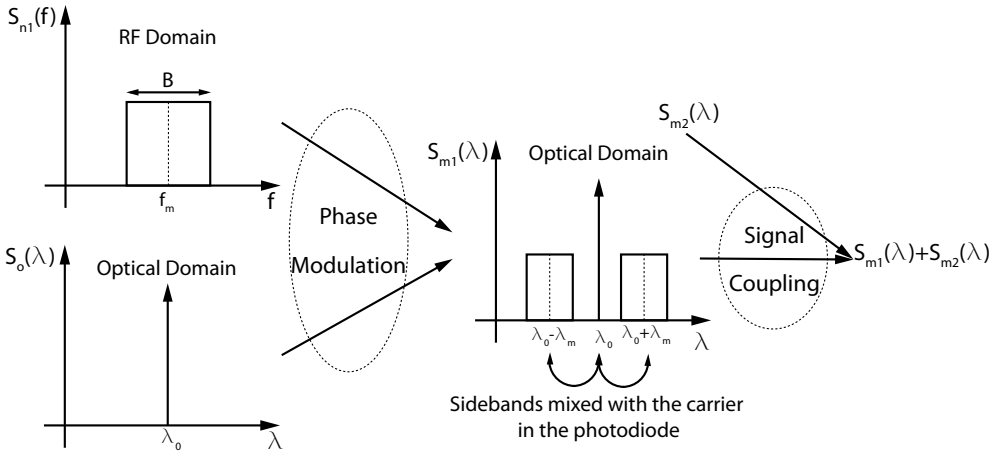
Figure 4.3: Spectrum of the signal in each step of the modulation and detection process. The RF spectrum of the signal coming from the receiver $S_{ni}(f)$ modulates an ideal optical laser source $S_o(\lambda)$. The resulting modulated signal S_{mi} is added to the modulated signal coming from other receiver S_{mj}. The result is mixed in a photodiode producing a signal with spectrum centered at f_m and bandwidth B proportional to $S_{ni}(f) + S_{nj}(f)$. The final step is to measure the power of the signal with a power detector. This process yields a DC component with the correlation between the RF signals coming from both receivers.

back to the block diagram of Fig. 4.2, for an input signal of the modulator $x_{1,2}(t)$ consisting of a band limited Gaussian noise of bandwidth B, the modulated optical signal is given by

$$b_i^{\text{DSB}}(t) \approx E_0 \left[\cos\left(\omega_0 t + \phi_i\right) - \frac{\pi}{V_\pi L_m} x_i(t) \sin(\omega_0 t + \phi_i) \right], \tag{4.7}$$

where L_m corresponds to the optical losses in the modulator and $x_i(t)$ is defined as

$$x_i(t) = n_{\text{I}i} \cos(\omega_m t) - n_{\text{Q}i} \sin(\omega_m t), \tag{4.8}$$

being $n_i(t) = n_{\text{I}i}(t) + j n_{\text{Q}i}(t)$ the equivalent baseband signal of the noise.

The following calculations are particularized for two front-ends and it is assumed that $n_{1,2}(t)$ are equal with a certain group delay difference $n_1(t) = n_2(t - \tau)e^{-j\omega_m \tau}$ and with equal power $P_{n1,n2} = P_n$. Hence the correlation level of the RF signals modulating the laser in each branch will depend on the delay difference τ. The effect of the receiver equivalent noise temperature and therefore the effect of additive uncorrelated noise in the result is discussed in Section 4.1.5.

In Fig. 4.2 the modulated optical signals $b_1^{\text{DSB}}(t)$ and $b_2^{\text{DSB}}(t)$ are combined using an optical coupler and driven into a photodiode. The resulting photocurrent is amplified using a TIA. The photo-conversion processing performs a non-linear operation that mixes the frequency of the sum $b_1^{\text{DSB}}(t) + b_2^{\text{DSB}}(t)$ resulting in a DC component and multiple signal bands of which only the ones falling inside the photodiode bandwidth $\omega = \{\omega_m, 2\omega_m\}$ are available. If a bandpass filter centered at $\omega = \omega_m$ is applied to the output of the TIA the resulting signal is given by

$$y_{\text{DSB}}(t) = \sqrt{C}\sin(\Delta\phi)[x_1(t) - x_2(t)], \qquad (4.9)$$

where $C = \left(\frac{\pi E_0^2 R Z}{V_\pi L_m}\right)^2$ being Z the transimpedance of the TIA, and R the responsivity of the photodetector. Finally, the power of the filtered signal is described as

$$p_{\text{DSB}}(\tau, \Delta\phi) = \frac{C}{2T}\int_T \|y_{\text{DSB}}(t)\|^2 dt = \frac{C}{2T}\sin^2(\Delta\phi)\left[\int_T \|n(t)\|^2 dt - \right.$$
$$\left. - \Re\left\{\int_T n(t)n^*(t-\tau)e^{-j\omega_m\tau}dt\right\}\right], \qquad (4.10)$$

where $n(t) = n_2(t)$, $\Delta\phi = \phi_2 - \phi_1$ is the phase difference between optical channels and the symbol $\Re$ denotes real part. Taking into account the properties of band limited noise the power of the filtered signal becomes

$$p_{\text{DSB}}(\tau, \Delta\phi, \Delta\psi) = C \cdot P_n \sin^2(\Delta\phi)(1 - \cos(\Delta\psi) \cdot \text{sinc}(B\tau)), \qquad (4.11)$$

where $\Delta\psi = \psi_2 - \psi_1 = \omega_m\tau$ is the RF instantaneous phase difference. Note that (4.11) gives the theoretical cross-correlation between $x_1(t)$ and $x_2(t)$ except for a phase shift of $180°$ and a factor which depends on the optical phase difference $\Delta\phi$. By properly controlling $\Delta\phi$ to the fixed values $\Delta\phi = \frac{\pi}{2}, \frac{3\pi}{2}$, the measured power becomes

$$p_{\text{DSB}}(\tau, \Delta\psi) = C \cdot P_n(1 - \cos(\Delta\psi) \cdot \text{sinc}(B\tau)). \qquad (4.12)$$

An schematic showing the spectrum of the signal in each of the intermediate steps of the modulation and detection process is presented in Fig. 4.3.

4.1.4   Cross-correlation of single-sideband optical modulated signals

The main drawback of working with a DSB modulation resides in the necessity of maintaining the optical phase difference to $\Delta\phi = \frac{\pi}{2}, \frac{3\pi}{2}$. If only the correlation between two receivers is needed, the phase control can be easily performed by applying a DC voltage to the phase modulators. However, if the number of receivers is greater than 2, it is not possible to have simultaneously all the optical channels with the required phase difference. Therefore the correlations of all receiver pairs cannot be computed at once. A possible solution is to use a SSB modulation that, as will be shown in the following paragraphs, requires a phase difference between optical channels of $\Delta\phi = 0$.
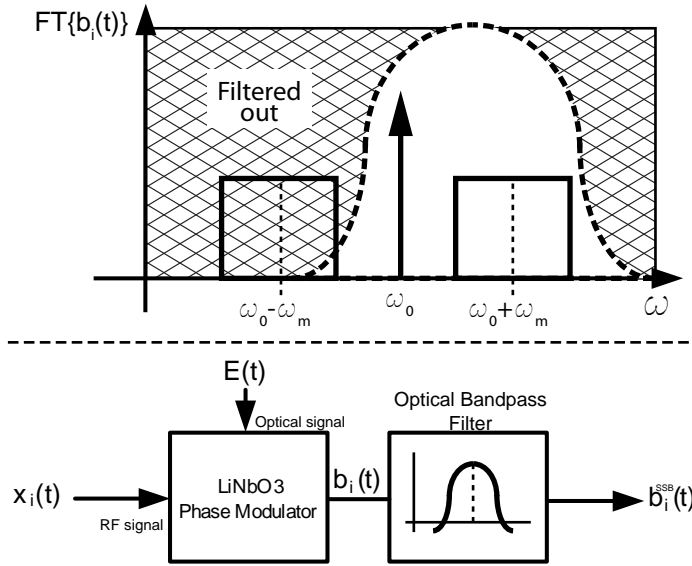
Figure 4.4: Schematics of the filtering process required to obtain the SSB modulation. The top scheme shows the frequency spectrum of the signal $b_i(t)$ with both sidebands. In this case, the lower sideband is filtered out to obtain an upper-sideband modulation. The bottom scheme shows a block diagram with the process required to obtain $b_i^{\mathrm{SSB}}(t)$.

In a SSB modulation, either the upper or the lower sideband created by the modulation is suppressed. Figure 4.4 shows an schematics with the procedure required to obtain an SSB modulation. In order to filter out one of the sidebands created by the phase modulation two different techniques can be applied: the first consists on filtering out one of the sidebands given by a phase modulator whereas the second consists on using an SSB modulator which suppresses one of the sidebands in the modulation process [76]. In both cases, the complexity of the system is increased: In the first case a an additional optical component consisting of an optical filter should be added in each optical branch; and in the second case, the utilization of an optical SSB modulator requires splitting the RF signal in two branches and switching the phase 90° in one of the branches, thus requiring extra RF hardware.

In the case that the lower sideband is removed from the modulation the signal $b_i(t)$ at the output of the modulator is expressed as:

$$b_i^{\mathrm{SSB}}(t) \approx E_0 \Re \left\{ e^{j(\omega_0 t + \phi_i)} \left[1 + \frac{\pi}{2 V_\pi L_m} n_i(t) e^{j\omega_m t} \right] \right\} \tag{4.13}$$

The signals coming from both modulators are combined, detected by a photodiode, amplified by a TIA and filtered at $\omega = \omega_m$. The resulting signal at the output of the filter is:

$$y^{\mathrm{SSB}}(t) = \frac{\sqrt{C}}{2} \left[(x_1(t) + x_2(t))(1 + \cos(\Delta\phi)) + \right. \\ \left. + \sin(\Delta\phi)(x_1'(t) - x_2'(t)) \right] \tag{4.14}$$

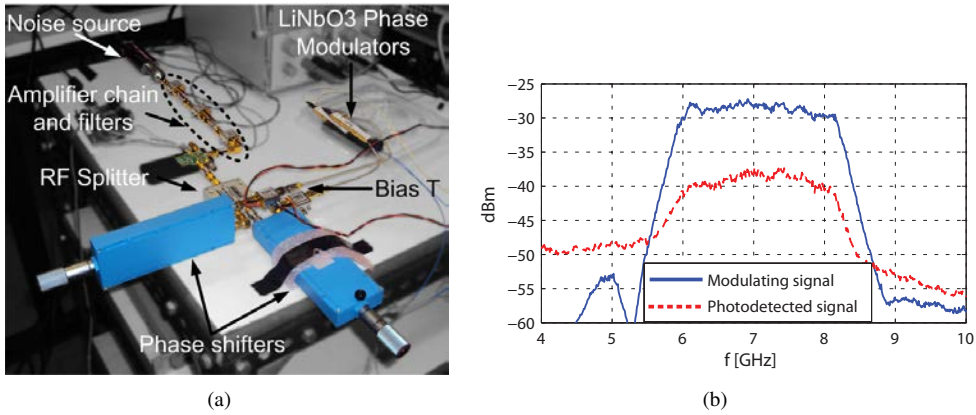(a)   (b)

Figure 4.5: (a) Photograph of the RF part of the setup used to prove experimentally eq. (4.11). The noise signal generated by a noise source is amplified, filtered and split in two branches. One phase shifter is used per branch in order to avoid signal decorrelation although only the phase of one branch is swept. Two Bias-T are used to control the optical phase difference between paths by applying a DC voltage to the modulators. (b) Spectrum of the RF noise signal used to modulate the optical laser (in blue) and spectrum of the optical modulated signal mixed by the photodiode and amplified by the TIA (in red). The resolution bandwidth of the measurement is $10\,\mathrm{MHz}$.

where $x_i'(t) = \Re\left\{jn_i(t)e^{j\omega_m t}\right\}$. If it is assumed that $n_1(t) = n_2(t-\tau)e^{-j\omega_m \tau}$ and $P_{n1,n2} = P_n$, then the measured power is described by:

$$p^{\mathrm{SSB}}(\tau, \Delta\phi, \Delta\psi) = \frac{1}{2T}\int\limits_T \left\|y^{\mathrm{SSB}}(t)\right\|^2 dt =$$

$$= CP_n(1 + \cos(\Delta\phi)\left[1 + \mathrm{sinc}(B\tau)\cos(\Delta\psi - \Delta\phi)\right] \tag{4.15}$$

If the phase difference between optical channels is fixed to $\Delta\phi = 0$ the maximum output power is achieved for a certain correlation level of the signals, yielding:

$$p^{\mathrm{SSB}}(\tau, \Delta\psi) = 2CP_n\left[1 + \mathrm{sinc}(B\tau)\cos(\Delta\psi)\right] \tag{4.16}$$

4.1.5   Optical correlation measurements of RF noise

This section presents a first experimental validation of the results obtained in Section 4.1.3. The measurements presented in this chapter are performed using a DSB modulation since the hardware requirements are lower. The results obtained with the DSB modulation are used to validate the utilization of the optical technique with interferometric radiometers. The conclusions obtained with those results can be directly extended to the method using a SSB modulation since the principle of operation is the same. Figure 4.5(a) shows part of the experimental setup used to perform the measurements, including the RF stage and the optical modulators. The rest of the setup is included in the schematic of Fig. 4.2.

In order to test the optical correlator, the IF noise signals $x_{1,2}(t)$ shown in Fig. 4.2 are synthesized by means of a broadband noise source with an equivalent noise temperature $T_N = 10000\,\mathrm{K}$ followed by 3 amplifiers of $24\,\mathrm{dB}$. A bandpass filter centered at $7\,\mathrm{GHz}$
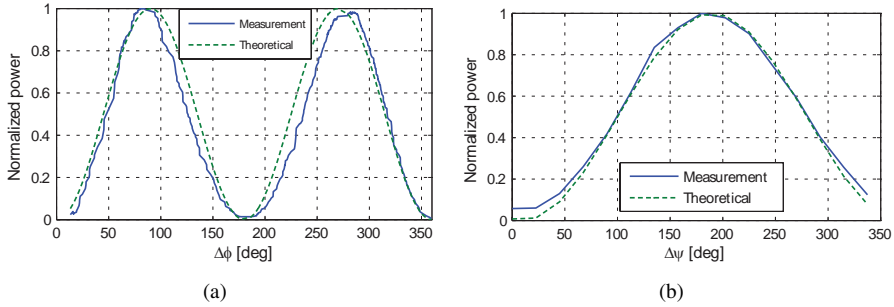
Figure 4.6: (a) Measured signal amplitude (blue line) of the setup presented in Section 4.1.5 when varying the IF phase $\Delta\psi$ with the phase shifter placed in the RF noise signal path while maintaining $\Delta\phi = \frac{\pi}{2}$. The theoretical curve (green dotted line) has been calculated using (4.12). (b) Measured signal amplitude (blue line) of setup presented in Section 4.1.5 when varying the optical phase $\Delta\phi$ by applying a DC voltage to one modulator. The theoretical curve (green dotted line) has been calculated using (4.11).

with approximately $2\,\mathrm{GHz}$ of bandwidth is placed just after the amplifiers. The signal is then divided in two using an RF splitter, and phase shifters are introduced in each path to allow changing their phase independently while preserving the symmetry between paths length, thus preserving correlation. The signals coming out of the phase shifters are driven to the optical modulators through a Bias-T to permit the use of a DC voltage to control the optical phase difference $\Delta\phi$. Finally the signals from each modulator are combined using an optical coupler and mixed in a photodiode. The detected photocurrent is then amplified using a TIA.

Figure 4.5(b) shows the spectrum of the RF modulating signal (blue line) and the detected optical signal (red line) when both paths are combined. The measurement has been performed just at the output of the optical receiver Agere 2860E shown in Fig. 4.2 using a Rohde & Schwarz FSP40 spectrum analyzer. An equivalent noise bandwidth of $1.8\,\mathrm{GHz}$ centered at $7\,\mathrm{GHz}$ is achieved, and the whole optical stage attenuates the band of interest about $10\,\mathrm{dB}$.

The experimental setup allows to modify the optical phase difference $\Delta\phi$ and the RF phase difference $\Delta\psi$. Figures 4.6(a) and 4.6(b) show the relative variation of the detected signal amplitude with $\Delta\phi$ and $\Delta\psi$ respectively. The measured results are compared with the expected behavior according to (4.11) and (4.12). A good agreement is obtained between analytical results and measurements, which experimentally confirms the feasibility of correlating two RF signals in the optical domain. Furthermore, Fig. 4.6(a) shows the capability of the system to keep the optical phase coherence.

4.2 Millimeter-wave interferometry measurements with optical signal processing

This section presents measurements performed using two independent radiometric front-ends to synthesize the different baselines of a 1D interferometric radiometer array. Therefore in this case, the signals $n_1(t) = n_c(t) + n_{u1}(t)$ and $n_2(t) = n_c(t-\tau) + n_{u2}(t)$ are composed by

a correlated $n_c(t)$ and an uncorrelated noise $n_{ui}(t)$. The correlated part is the noise coming from the scene that reaches both receivers and therefore is directly related with the antenna temperature T_A. The uncorrelated part is the noise generated by the receiver itself and is related to the receiver noise temperature T_R. If the noise power reaching each antenna is considered equal, as well as the equivalent noise temperature of both receivers, the total power at the output of the receivers are equal $P_{n1,n2} = P_n$. If phasorial notation is used for the noise, eq. (4.10) is transformed in the following expression for $\Delta\phi = \{\frac{\pi}{2}, \frac{3\pi}{2}\}$ [54]

$$
\begin{aligned}
p(\tau) &= C\Re\left[P_n - \frac{1}{2T}\int_T n_c(t)n_c^*(t-\tau)e^{-j\omega_m\tau}dt \right] \\
&= C\Re\left[P_n - S\iint T_B'(\xi,\eta)e^{-j2\pi u\xi}d\xi d\eta \right],
\end{aligned}
\tag{4.17}
$$

where symbol $\Re$ denotes real part and $S = k_B BG$ and

$$
T_B'(\xi,\eta) = \frac{T_B(\xi,\eta)t(\xi,\eta)}{\Omega_a\sqrt{1-\xi^2-\eta^2}}.
\tag{4.18}
$$

Decorrelation effects have been neglected ($\text{sinc}(B\tau) \approx 1$) for the sake of simplicity. By including (2.26) in (4.17) the relation between the measured optical power and the scene visibility becomes

$$
p(u) = C\left(P_n - S\Re\{V(u)\} \right).
\tag{4.19}
$$

Note that P_n can be several orders of magnitude higher than $S\Re\{V(u)\}$ due to the equivalent noise temperature of the receivers and therefore the dynamic range of the measurement is strongly reduced. This issue cannot be calibrated since gain stability effects on P_n would mask completely the calibration and the measurement of $\Re\{V(u)\}$. However this can be solved by using the phase switching technique proposed in this section, which subtracts P_n thus improving the quality and stability of the measurement.

4.2.1   Phase switching technique

The value of $\Re\{V(u)\}$ can be directly obtained if a phase switching method is used [77]. If a phase shift of $\psi_0 = 180\,^\circ$ is introduced to the output signal of one of the radiometric receivers, the second term in equations (4.17) and (4.19) becomes positive. Hence, taking the difference between two consecutive measurements with a phase shift $\Delta\psi_0 = 180\,^\circ$ between them, the resulting value is given by

$$
r(u) = 2CS\Re\{V(u)\}.
\tag{4.20}
$$

Hence, if the RF and optical parameters of the receiver are calibrated the value $\Re\{V(u)\}$ can be obtained. The phase switching technique can be implemented by either having a phase shifter in each RF front-end and sequentially change between both phase states or by duplicating the optical channel with a difference of $180\,^\circ$. There is a tradeoff between complexity and acquisition time, since duplicating the optical channel will reduce the acquisition time by

a factor of 2. In the case of having a phase shifter, it can also be used to obtain the imaginary part of the correlation by adding a phase shift of $90\,^\circ$ between both receiver signals

$$r(u)|_{\psi_0 = 90^\circ} = 2CS\Im\{V(u)\}. \tag{4.21}$$

An additional issue to consider in the phase switching technique is the effect of the gain fluctuation of receiver amplifiers in the value of P_n. In order to subtract the value of P_n from the measurement, the effect of gain variations must be canceled. This is achieved by setting the phase switching rate faster than the gain variation. In our experiment, we have chosen a switching rate of $50\,\mathrm{Hz}$, above the gain fluctuation rate of our system. In order to have a visibility integration time t_v larger than the phase switching period, multiple measurements are averaged.

4.2.2   Fringes created by a point source

An scene with a point source has been employed to validate the equations presented in the previous section. The schematic of the scene setup is shown in Fig. 4.7(a). The fringe pattern is measured by translating the point source along the x direction in the range of $-2.5\,\mathrm{cm} < x_{\mathrm{PS}} < 2.5\,\mathrm{cm}$ at a distance $R = 25\,\mathrm{cm}$ from the antennas, for a fixed baseline $u_0 = 17.13$. In this case $T'_B(\xi_i, \eta_i) = \frac{T_{B0} t(\xi_i, 0)}{\Omega_a} \Pi(\frac{\xi - \xi_i}{\Delta \xi}) \Pi(\frac{\eta - \eta_i}{\Delta \eta})$ where Π corresponds to a normalized rectangular function. The antenna power pattern $t(\xi, \eta)$ is considered to be constant along the point source solid angle and the source is considered to be close to the boresight direction. In this case (4.17) is expressed as:

$$p(\xi_i) = C\left[P_n - \frac{ST_{B0}t(\xi_i, 0)}{\Omega_a} \Delta\xi\Delta\eta \cos(2\pi u_0 \xi_i)\mathrm{sinc}(u_0\Delta\xi)\right] \tag{4.22}$$

and applying the phase switching technique, the correlation is:

$$r(\xi_i) = \frac{2CST_{B0}t(\xi_i, 0)}{\Omega_a} \Delta\xi\Delta\eta \cos(2\pi u_0 \xi_i)\mathrm{sinc}(u_0\Delta\xi) \tag{4.23}$$

An interferometric radiometer with two receivers has been built to test the capabilities of the method with a wide bandwidth radiometric signal. The setup is shown in Fig. 4.7(b) and Fig. 4.8, and it consists of two W-band front-ends to downconvert a $97\,\mathrm{GHz}$ signal to a $7\,\mathrm{GHz}$ IF (the maximum operating frequency of the LiNbO3 modulator is $10\,\mathrm{GHz}$). This configuration can be simplified if a W-band LiNbO3 modulator is used [78]. The optical scheme is the same one used in Section 4.1.5. The RF front-end consists of a W-band conical horn antenna, with a beamwidth of $17.5\,\mathrm{deg}$ followed by a LNA; a double-balanced mixer and a $2\,\mathrm{GHz}$ band-pass filter centered at $7\,\mathrm{GHz}$; a chain of two amplifiers with a total gain of $48\,\mathrm{dB}$ gain and a phase shifter to implement the phase switching technique between the receivers. Finally the integration time for each fringe point has been established at $200\,\mathrm{ms}$.

The point source consists of a ceramic resistor that has been warmed up to around $240\,^\circ\mathrm{C}$. Fig. 4.9 shows the resulting theoretical fringe pattern obtained with (4.23) plotted with the measured response. It can be observed that the measurements matches with theoretical prediction, proving the suitability of the method with radiometric signals.
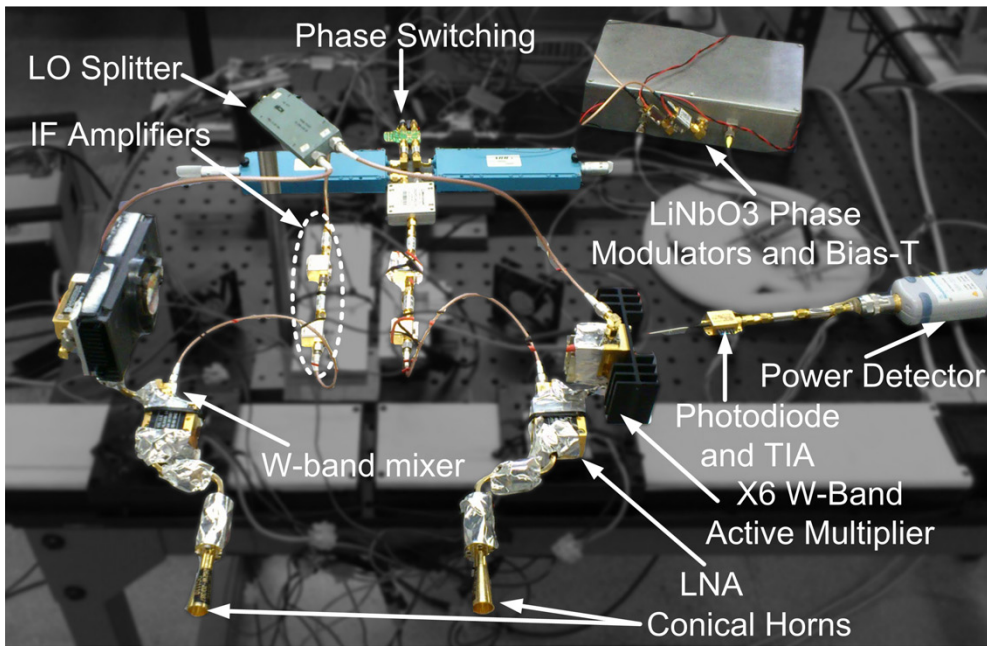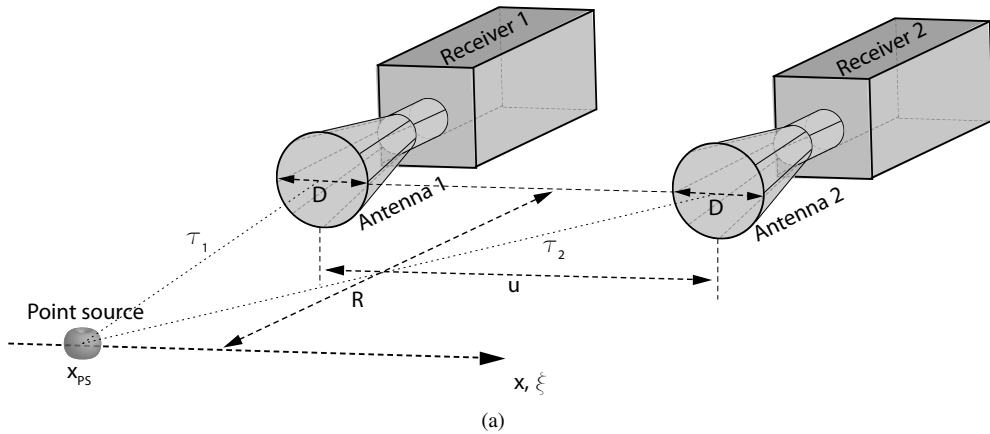
(a)

(b)

Figure 4.7: (a) Schematic of the setup used in Sections 4.2.2 and 4.2.3. A point source based on a hot resistor has been used as target to perform the measurements. (b) Photograph of the W-band and optical setup built to perform the measurements described in Sections 4.2.2 and 4.2.3. The components of two radiometric receivers are shown. The W-band components of each receiver are a conical horn antenna, a LNA, a mixer and a x6 multiplier. The schematics of the receiver chain is described in Fig. 4.8 whereas the optical part has been shown in Fig. 4.2.

4.2.3   One-dimensional image

A one-dimensional brightness temperature distribution has been imaged using the optical correlation method proposed in this paper with the same receiver architecture as in Section 4.2.2.
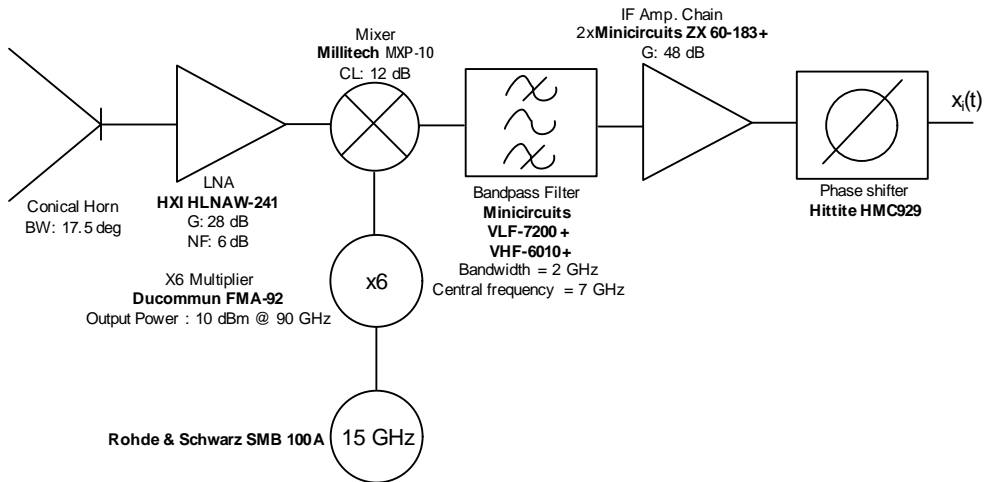
Figure 4.8: Schematic of the W-band receiver components. A conical horn with $17.5\,\text{deg}$ of beamwidth has been used as an antenna. A LNA with $28\,\text{dB}$ gain and NF of $6\,\text{dB}$ is placed before the mixer. The $7\,\text{GHz}$ IF signal is filtered with $2\,\text{GHz}$ of bandwidth and is amplified $48\,\text{dB}$. The last component before the optical modulator is a phase shifter used to perform the phase switching described in Section 4.2.1.
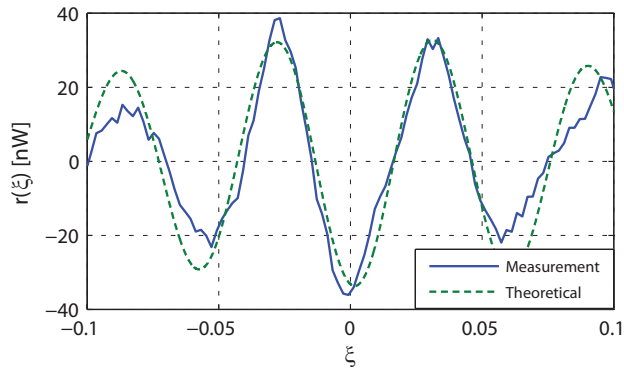

Figure 4.9: Measured fringe pattern created by a point source at a distance of $25\,\text{cm}$ with a fixed antenna baseline of $u = 17.13$. The center frequency of the RF signal is $97\,\text{GHz}$ as described in Fig. 4.8. The measured values match with the analytical expression (4.23).

The radiometric front-ends have been mounted on linear stages to synthesize the baselines corresponding to a linear array of antennas. The real part of the visibility samples have been obtained from the correlation of the signals given by both receivers as described by (4.22) integrating $200\,\text{ms}$ for each visibility. In order to obtain the imaginary parts of the visibilities, a $90°$ phase shift has been added to one receiver signal. Moreover, before obtaining the images a first calibration has been performed to retrieve the phase imbalance between both receivers. In order to obtain the reconstruction of the scene the phase imbalance has been
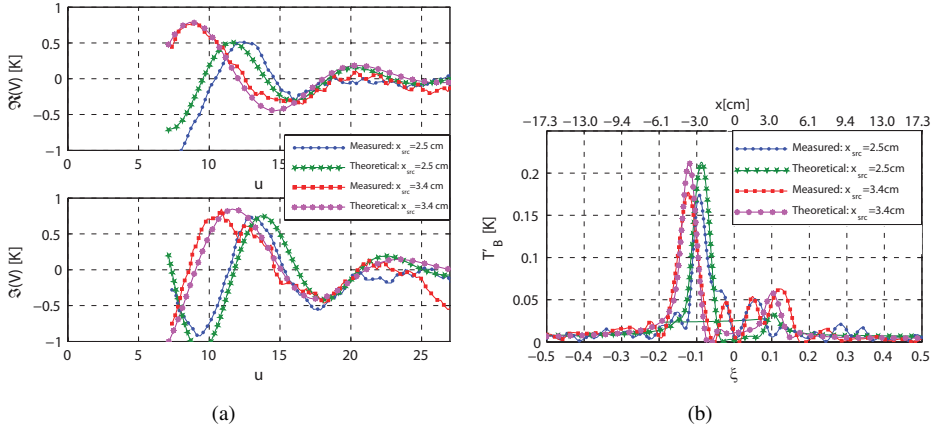
Figure 4.10: (a) Measured real and imaginary parts of the scene visibilities for two different scenes consisting on a point source placed at $x_{PS} = -2.5\,\text{cm}$ and $x_{PS} = -3.4\,\text{cm}$ from the origin. The visibilities from $u = 0$ to $u = 6$ cannot be measured since the minimum antenna spacing is given by the conical horn flange adapter of 22 mm. (b) The plot shows two reconstructed scenes obtained by applying (4.24) to the measured visibilities shown in Fig. 4.10(a). The two different scenes consist of a point source placed at $x_{PS} = -2.5\,\text{cm}$ and $x_{PS} = -3.4\,\text{cm}$ from the origin at a distance $R = 30\,\text{cm}$ from the antennas.

corrected from the visibilities. An antenna separation of $\Delta u = \lambda/2$ has been chosen in order to avoid aliasing in the image as explained in Chapter 2.

The same ceramic resistor used in the previous section has been used as the point source and it has been placed at a distance of $R = 30\,\text{cm}$ of the array. Two measurements have been taken corresponding to two positions of the resistor, $x_{PS} = -2.5\,\text{cm}$ ($\xi_{PS} = -0.08$) and $x_{PS} - 3.4\,\text{cm}$ ($\xi_{PS} = -0.12$) from the center of the array. A total of $N_{mu} = 42$ visibilities have been measured corresponding to a synthetic array of 42 antennas. Figure 4.10(a) shows the visibilities for $u > 0$ with an $u_{max} = 27$. It must be noted that the visibilities in the range $0 < u < 6$ cannot be measured due to the flange of the conical horn antennas used in the measurement, which forces a minimum baseline $u_{min} = 6$. Nevertheless, the measured visibility values agree with the simulated values. In order to retrieve the scene from the measured visibilities the inverse Fast Fourier Transform (iFFT) is applied:

$$T'_B(\xi) = \int V(u)e^{j2\pi u\xi}du \tag{4.24}$$

giving as a result the linear reconstruction shown in Fig. 4.10(b). The reconstructed image matches with the position of the point source and roughly matches with the amplitude if the system parameters described in Section 4.2.2 are used to calculate constants C and S of (4.21).

A second scene has been measured with two resistors placed at $x_{PS} = -5.5\,\text{cm}$ ($\xi_{PS} = -0.09$) and $x_{PS} = 1.5\,\text{cm}$ ($\xi_{PS} = 0.02$) from the center of the array at a distance $R = 60\,\text{cm}$ from the antennas. Fig. 4.11(a) shows an infrared image of the scene revealing the physical temperature of the resistors. After applying (4.24), the scene is reconstructed as shown in Fig. 4.11(b). A good agreement between the image and the scene is obtained.
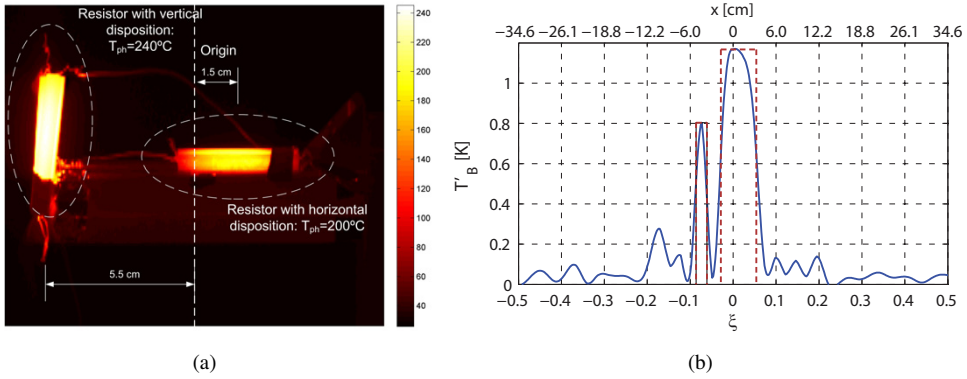
(a)   (b)

Figure 4.11: (a) Infrared image of a scene consisting on one resistor in vertical disposition placed at $x_{PS} = -5.5$ cm from the origin and one resistor placed horizontally at $x_{PS} = 1.5$ cm. The measured physical temperature of the resistors is around $200\,°C$. The scene distance from the antennas is $R = 60$ cm. (b) Reconstructed image from the scene shown in (a) obtained by applying (4.24) to the measured visibilities. The response of both resistors, centered at $x_{PS} = -5.5$ cm and $x_{PS} = 1.5$ cm from the center of the array respectively and at a distance $R = 60$ cm from the antennas.

4.3 Optical signal distribution for cross-correlation of multiple receivers

The measurements presented in Section 4.1.5 have been performed with two receivers. Nevertheless the optical modulation method presented in this paper allows the combination of multiple receiver signals in the optical domain in order to perform the cross-correlation. The combination can be performed in the free-space due to the possibility of guiding optical beams with low divergence and with high spatial density. Moreover, the high level of integration of optical components and waveguides make the optical signal routing affordable with no constraint on the RF signal bandwidth [79] [80]. The following section proposes a free-space combination scheme for an arbitrary number of front-end receivers.

4.3.1 Distribution technique

Figure 4.12 show an schematics of the signal distribution system. The optical signals coming from each modulator $b_i(t)$ are introduced to an optical splitter matrix having a number of inputs equal to the number of receivers N_r and a number of outputs of $2N_r$. This matrix is equivalent to N_r sub-couplers, one for each optical channel, that is in charge of coupling the input signal to 2 outputs with the same power level. The $2N_r$ output channels are distributed using fiber optics towards collimating lenses that will emit the optical beam in a collimated way. The N_r optical beams split by the optical splitter matrix, containing one of the two beams split by each sub-coupler $sb_{i2}(t)$, carried and grouped into collimating lenses that will emit the beams with horizontal distribution. The N_r beams are introduced to a diffractive beamsplitter that will divide each beam along the vertical axis in N_r sub-beams.

The beams produced by a diffractive beamsplitter are emitted with a certain angle, there-
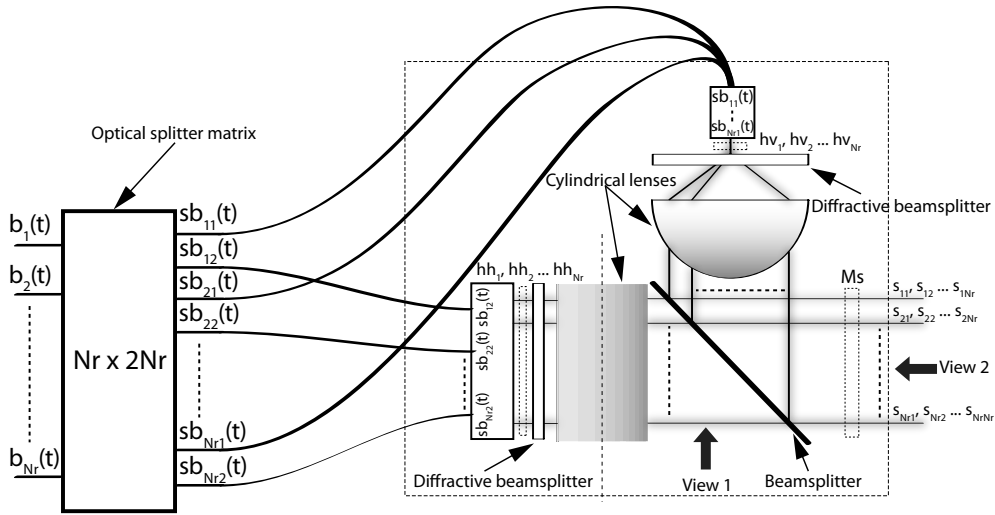
Figure 4.12: Schematic of the distribution system. The optical signals $b_i(t)$ coming from the modulators enter to the optical splitter matrix placed at the left of the schematic. The output signal matrix beams s_{ij} are driven to photodiode matrix shown in Fig. 4.14. The schematics of the points of view "View 1" and "View 2" are shown in Fig. 4.13.
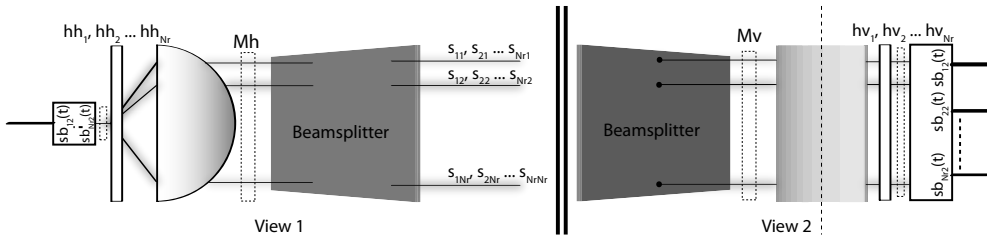
Figure 4.13: Points of view "View 1" and "View 2" from the Fig. 4.12.
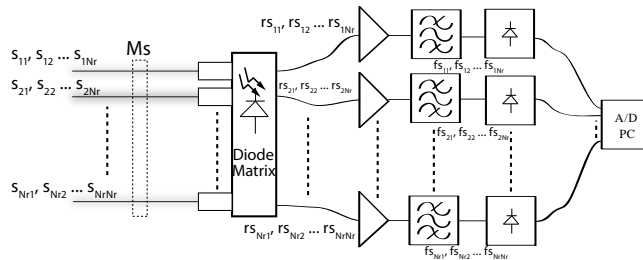
Figure 4.14: Schematics showing the opto-electronic conversion matrix, the filtering and amplifying components and the power detector arrays.

fore in order to avoid the divergence of the beams a cylindrical lens is used to collimate the beams along the vertical axis. This lens should be placed with the cylinder axis along the horizontal plane and with a distance from the diffractive splitter equal to its focal distance. In
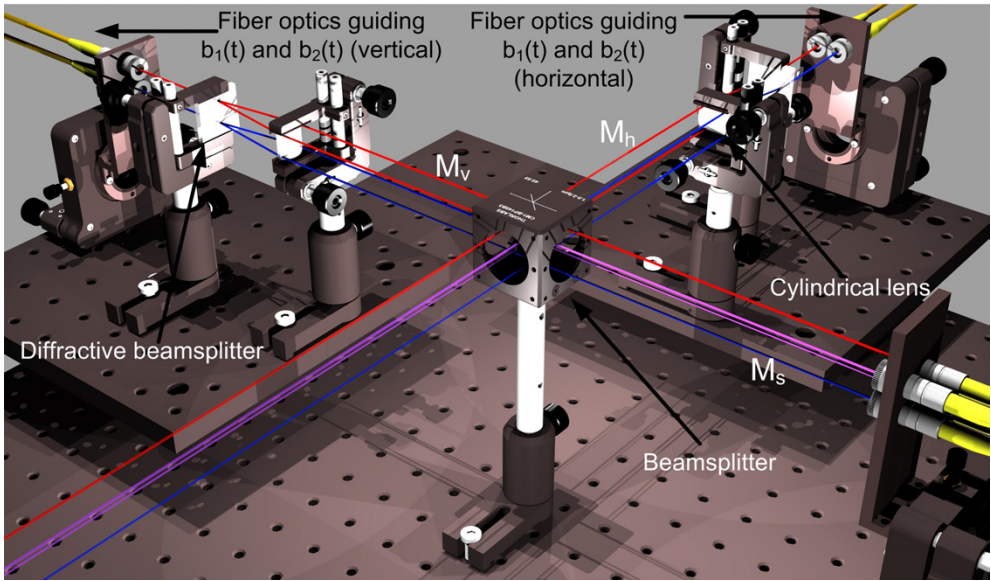
Figure 4.15: Artist view of the multiplexing scheme. The red beam represents $b_1(t)$ whereas the blue beam represents $b_2(t)$. The purple beam is the result of adding $b_1(t) + b_2(t)$. The artist view is representative of the setup mounted in the laboratory to prove the suitability of the scheme.

such way the beams are collimated and the matrix Mh is formed

$$
M_h = \begin{bmatrix} b_1 & b_2 & \cdots & b_{N_r} \\ b_1 & b_2 & \cdots & b_{N_r} \\ \vdots & \vdots & \ddots & \vdots \\ b_{N_r} & b_2 & \cdots & b_{N_r} \end{bmatrix}.
\tag{4.25}
$$

The remaining Nr channels $sb_{i1}(t)$ split by the optical splitter matrix are transported, grouped along the vertical axis, introduced in collimating lenses and emitted with vertical disposition. Using a diffractive beamsplitter the beams are divided along the horizontal plane creating N_r beams from each original beam an therefore creating a matrix of N_rxN_r elements. Finally the beams are collimated using a cylindrical lens having the cylinder axis along the vertical axis of the system. The process is equivalent to the one described in the previous paragraph with the only difference that the resulting beam matrix M_v is rotated 90° with respect the matrix M_h

$$
M_v = \begin{bmatrix} b_1 & b_1 & \cdots & b_1 \\ b_2 & b_2 & \cdots & b_2 \\ \vdots & \vdots & \ddots & \vdots \\ b_{N_r} & b_{N_r} & \cdots & b_{N_r} \end{bmatrix}.
\tag{4.26}
$$

Figure 4.13 clarifies the beam distribution in this part of the system. In a final step, the beam matrices M_h and M_v are driven to a beamsplitter plate in order to combine the beams and

obtain a sum matrix M_s

$$M_s = \begin{bmatrix} b_1 + b_1 & b_2 + b_1 & \cdots & b_{N_r} + b_1 \\ b_1 + b_2 & b_2 + b_2 & \cdots & b_{N_r} + b_2 \\ \vdots & \vdots & \ddots & \vdots \\ b_1 + b_{N_r} & b_2 + b_{N_r} & \cdots & b_{N_r} + b_{N_r} \end{bmatrix}. \tag{4.27}$$

The final step in the correlation process is based on the detection of the signal contained in each optical beam. Figure 4.14 shows that a photodetector matrix is used to obtain the mixing between the optical carrier and the optical sidebands for each element of M_s. Each photodetector is followed by a TIA in order to convert the current signal given by the photodetector to a voltage signal with a certain transimpedance gain. Following the TIA a filter with the same passband as the original RF signal is placed. The resulting signal at this point is given by 4.9 or 4.14 if either DSB or SSB modulations are used respectively. The final step consists of measuring the power by using an array of power detectors. The resulting matrix contains the real part of the visibilities and is given by the following matrix for a DSB modulation

$$M_v = C(P_n - S\Re \left\{ \begin{bmatrix} V_{11} & V_{21} & \cdots & V_{N_r 1} \\ V_{12} & V_{22} & \cdots & V_{N_r 2} \\ \vdots & \vdots & \ddots & \vdots \\ V_{1N_r} & V_{2N_r} & \cdots & V_{N_r N_r} \end{bmatrix} \right\}). \tag{4.28}$$

The following step is to perform the phase switching technique to remove P_n from the result. It should be pointed out that the lower triangular matrix is redundant and it is not necessary to be measured. The main drawback of this method is the strong alignment requirements of the optical devices. Moreover, the phase variations in the fiber makes the proposed scheme unfeasible without a phase control on each channel. Both issues can be solved if the scheme is integrated and implemented with photonic waveguides. Figure 4.15 shows a 3D representation of the proposed optical signal distribution scheme.

4.4 System Performance Considerations

The performance of the system in terms of radiometric sensitivity is described in this section taking into account the contribution of optical correlation process and the phase switching technique. In addition, the image acquisition time is studied depending on the optical modulation scheme and system parameters to foresee the suitability of the method when real-time imaging is required.

4.4.1 Radiometric sensitivity

The main noise sources in the system are the thermal noise generated in the receiver chain, the shot noise generated in the photodetector and the receiver gain variations falling in a phase switching period. The effect of the shot noise of the photodetector is neglected in front of the thermal noise generated in the receiver front-ends since this is pre-amplified in the RF stage.
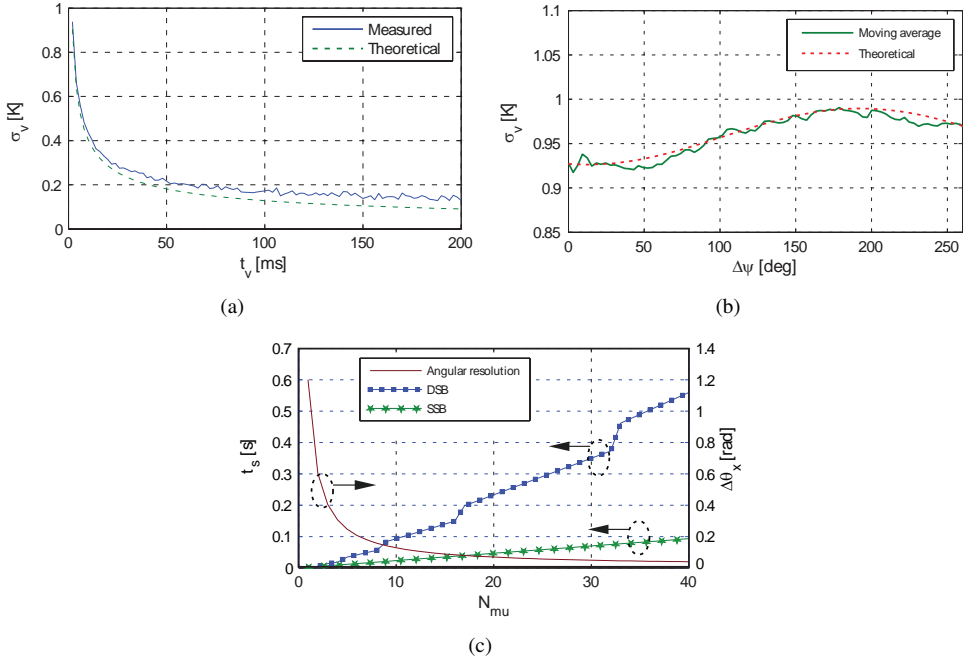
Figure 4.16: (a) Standard deviation of a visibility measurement σ_v depending on the integration time t_v. The noise received by the antennas is purely uncorrelated. The measurement is compared with the theoretical values provided by (4.29). (b) Standard deviation of a visibility measurement σ_v depending on the signal correlation level for an integration time $t_v = 2\,\text{ms}$. The phase of the IF signal is shifted $260\,\text{deg}$ with steps of $3\,\text{deg}$ to sweep the correlation level of the noise radiatied from a resistor point source. A moving average of 20 samples is calculated from the measured points. The measurement is compared with a theoretical curve calculated using (4.29). (c) Image acquisition time t_s depending on the number of antennas N_{mu} for a $\Delta T = 1\,\text{K}$. The system parameters are $T_A = 300\,\text{K}, T_R = 1000\,\text{K}$ and $B = 1.8\,\text{GHz}$. The angular resolution $\Delta\theta_x$ of the synthesized array is also depicted to show the tradeoff between spatial resolution and radiometric sensitivity.

The phase switching rate is selected to avoid the gain fluctuations of the front-end receiver components as well as to avoid variations in the laser amplitude. If a high gain LNA is placed at the front of the chain as in our case, T_R is mainly fixed by the noise figure of the LNA. The resulting standard deviation for a single visibility measurement if DSB modulation is used is given by

$$\sigma_v = \frac{T_{Au} + T_R - T_{Ac}\cos(\Delta\psi)}{\sqrt{Bt_v}} \quad [K], \tag{4.29}$$

where T_{Au} and T_{Ac} are respectively the equivalent temperature of the uncorrelated and correlated noise captured by the receiver antenna. The visibility integration time t_v is the sum of multiple phase switching periods. In the measurements performed in the previous sections, the integration time is $t_v = 200\,\text{ms}$ corresponding to 10 repetitions of a phase switching period of $20\,\text{ms}$. In order to validate (4.29), the visibility standard deviation has been calculated from visibility samples measured with the system described in Section 4.1.5.

Figure 4.16(a) shows the standard deviation of measured visibility samples for different integration times t_{v}. An absorber has been used to have a constant source of uncorrelated noise in front of the antennas ($T_{Ac} = 0\,\mathrm{K}$). The values of S and C used to obtain the visibility value from the measured power (4.21) are those used in Section 4.1.5. The theoretical curve has been calculated using (4.29) with $T_{Au} = 300\,\mathrm{K}$, $T_{Ac} = 0\,\mathrm{K}$, $T_R = 1400\,\mathrm{K}$ (corresponding to a $NF = 7.7\,\mathrm{dB}$) and $B = 1.8\,\mathrm{GHz}$.

Additionally, the dependance of the visibility standard deviation with the correlation level ($T_{Ac} = 60\,\mathrm{K}$) of the signals is shown in Fig. 4.16(b). A point source consisting of a resistor has been used to radiate correlated noise. In order to modify the correlation level of the processed noise signals, a phase sweep of $260\,^\circ$ in steps of $3\,^\circ$ has been performed using the phase shifter placed in the receiver chain. A set of 1000 visibility samples has been measured consisting of two phase switching periods of $1\,\mathrm{ms}$ yielding a total integration time of $t_{\mathrm{v}} = 2\,\mathrm{ms}$. These samples have been used to calculate the standard deviation of the visibility for different values of phase shift. A moving average of 20 samples has been calculated to clearly observe the sinusoidal behavior. The measurement is compared with a theoretical curve calculated using (4.29) with $T_{Ac} = 60\,\mathrm{K}$, $T_{Au} = 400\,\mathrm{K}$, $T_R = 1400\,\mathrm{K}$ and $B = 1.8\,\mathrm{GHz}$.

4.4.1.1 Image acquisition time

If a DSB modulation is used in the conversion process the phase shift between receiver channels $\Delta\phi$ should be maintained to $\{\frac{\pi}{2}, \frac{3\pi}{2}\}$ as stated in Section 4.1.3. Therefore, an imaging system composed by $N_{\mathrm{mu}} > 2$ receivers is not able to measure all the visibilities simultaneously since it is not possible to have the required phase shift between all the receiver pairs at once. A solution is to repeat the measurements in order to cover the whole set of combinations. It can be shown that for N_{mu} receivers, it is required a minimum of $\lceil \log_2(N_{\mathrm{mu}}) \rceil$ steps, where $\lceil \cdot \rceil$ denotes the ceiling value. Therefore the image acquisition time t_s depends on the number of receivers as $t_s = t_v \lceil \log_2(N_{mu}) \rceil$, leading to a radiometric sensitivity

$$\Delta T_{\mathrm{DSB}} = 1.4 \frac{T_A + T_R}{\sqrt{Bt_{\mathrm{s}}}} \sqrt{N_{\mathrm{mu}} \lceil \log_2(N_{\mathrm{mu}}) \rceil}. \tag{4.30}$$

A different approach is either to use a SSB modulation or to filter one of the sidebands, thus adding complexity to the system. In this case the optical phase shift required to perform the correlation is $\Delta\phi = 0$, and the complete set of visibilities could be measured at once ($t_s = t_v$) yielding

$$\Delta T_{\mathrm{SSB}} = 1.4 \frac{T_A + T_R}{\sqrt{Bt_{\mathrm{s}}}} \sqrt{N_{\mathrm{mu}}}. \tag{4.31}$$

Figure 4.16(c) shows the image acquisition time and angular resolution depending on the number of receivers for a $\Delta T = 1\,\mathrm{K}$. From the figure, it can be seen that for a particular case with an spatial resolution of $3\,\mathrm{cm}$ at a distance of $1\,\mathrm{m}$ from the antennas, the required number of antennas is $N_{\mathrm{mu}} = 36$. For this system, a DSB modulation increases the acquisition time by a factor of 6 compared with the SSB modulation.

4.4.1.2 Comparison with other available correlation techniques

The optical correlation technique described in this paper is similar to an RF analog correlation [58]. In both cases the correlation is performed by measuring the power of the combination of the received signals. The main difference resides in which domain the signal is distributed in order to obtain the combination of all receiver pairs as required in aperture synthesis interferometry.

There are several advantages of distributing the signals in the optical domain: 1) the signals can be distributed in the free space with collimated optical beams thus avoiding signal couplings and uncontrolled radiation that could appear with RF signal distribution; 2) photonic integrated devices can be used to incorporate the whole distribution system in a compact device; and 3) the bandwidth is limited by the optical modulator and can be of several tens of gigahertz whereas in the RF distribution the bandwidth would be limited by the complexity of the distribution components required to support large relative bandwidths. Nevertheless, in practice the optical system requires a real-time phase control to maintain fixed $\Delta\phi$, representing a drawback in front of the RF correlator.

An additional technique commonly used in interferometric radiometry consists on sampling the RF signals with 1-bit precision and performing the correlation in a field programmable gate array (FPGA) [81]. In this case the number of receivers N_r and the capacity of the FPGA limits the bandwidth, and therefore limits the real-time imaging capabilities of the system. Taking into account that the signal should be digitized with a sampling frequency of $f_s = 2B$ to fulfill Nyquist criteria, the amount of internal data that the FPGA should manage is related with $f_s N_r$ kbps. Hence, an interferometric system with a bandwidth of several GHz would require a huge processing system [82] that are not affordable for screening systems.

4.5   Conclusions

This chapter presents a method to perform cross-correlation of RF radiometric signals in the optical domain. The expressions governing the method are derived relating the results to the classical interferometric imaging theory. In addition, the experimental validations prove the suitability of the method to perform millimeter-wave passive interferometric imaging: 1) the fringe pattern of a moving point source has been measured using a single baseline obtaining a result that matches with the theoretical expressions; and 2) linear interferometric images have been acquired by translating two receivers to sequentially synthesize the baselines of a filled array of receivers, where the whole set of visibility samples have been obtained performing the correlation in the optical domain.

With respect to the performance of the system, it has been shown that the receiver temperature T_R of the system is not critically degraded by converting the signal to the optical domain since the LNA placed at the front-end fixes the noise figure for the whole receiver chain. This statement is supported in Section 4.4 with the calculation of the standard deviation of a visibility measurement σ_v, showing that the optical processing has no significant influence on the radiometric performance of the system. In addition, the dependance of the visibility standard deviation with the signal correlation level has been also supported with measurements in Section 4.4.

Additionally, Section 4.1.3 shows that if DSB modulation is used, the optical channels should have an optical phase difference fixed to $\Delta\phi = \{\frac{\pi}{2}, \frac{3\pi}{2}\}$. This has a direct impact on the image acquisition time since the visibilities cannot be acquired at once, representing an increment of $\lceil \log_2(N_{\mathrm{mu}}) \rceil$ with respect to SSB modulation. Hence for systems with high number of receivers an SSB modulation should be used (adding complexity in the optical modulation hardware) in order to achieve real-time imaging with bandwidths in the order of the GHz.

Terahertz Imaging and Spectroscopy

Terahertz Tomographic Imaging

T HE combination of diffractive THz tomography of a sample with its spectroscopic information has been investigated and the results are presented in this chapter. An algorithm based on the Born approximation has been used to retrieve 2-dimensional cuts of the sample. This method is based on filling the image spectrum by performing electric field measurements of the sample from different points of view. Once the image is reconstructed by applying an inverse Fast Fourier Transform (iFFT), each pixel contains the absorption spectrum of the material at that position. Section 5.1 shows the theoretical background of the diffractive tomography algorithm used to retrieve the images.

In order to test the reconstruction algorithm and to foresee the results, an electromagnetic simulation of the imaging scenario has been performed using the commercial simulator *COMSOL Multiphysics*. This simulator includes a 2-dimensional solver, thus allowing the simulation of scenarios (constant in z axis) that would be unaffordable for a 3-dimensional solver in terms of memory. The simulation setup and the results are presented in section 5.2 where the capabilities of the algorithm in terms of material detection are validated.

The third part of the chapter include THz measurements of different pharmaceutical compounds acquired with two different systems: 1) a time-domain spectroscopy system and 2) a frequency domain THz system. The first system has been used to measure the absorption spectrum of the compounds used as a sample in the imaging scenario whereas the frequency domain system has been used to perform the tomographic measurements.

On the one hand, the full absorption spectrum has been measured by using the time-domain spectroscopy system due to several reasons: 1) the THz path is purged with nitrogen thus avoiding the influence of the water vapor in the measured spectrum; 2) the dynamic range in the higher frequency range of the THz band is higher, as well as the total frequency range that extends up to 3 THz and 3) the frequency axis is precisely extracted due to the high accuracy of the linear delay stage.

On the other hand, the tomographic measurements have been performed with the frequency domain system since the fiber coupling of the Photoconductive Switch (PCS) allows the free movement of the antennas. Since the system consists on 1 transmitter antenna and

1 receiver antenna, rotation movements should be performed to measure the required points of view required to apply the reconstruction algorithm. Section 5.3 describes the measurement setup and presents the reconstructed tomographic images that show the detection and identification capabilities of the reconstruction algorithm introduced in this chapter.

5.1 Terahertz diffraction tomography

The imaging algorithm used to reconstruct the tomographic images appearing in this chapter is based on the Born approximation [83]. This approximation was first introduced in 1925 by Max Born in order to solve problems related with the scattering of atomic particles. It consists on a first-order approximation of a second-order differential equation (the inhomogeneous wave equation) that governs the electromagnetic field distribution in the object to be imaged.

The method described in this section is based on illuminating the sample with a plane wave and measure the field diffracted and scattered by the sample. The approximation is valid if the condition $d\Delta n < \frac{\lambda}{4}$ (where d is the sample diameter and Δn is the permittivity contrast between the sample material and the air) is fulfilled. Therefore, for a fixed sample size, as the frequency increases the permittivity contrast should decrease in order to fulfill the approximation.

Both the simulations and the measurements presented in this chapter do not fulfill the approximation. In practice, this means that no absolute information can be obtained from the images. Nevertheless, the relative information can be extracted to identify the sample component without absolute quantification. A different technique is usually used if absolute information is required: THz Computed Tomography (CT). CT uses a straight ray approach for the image reconstruction, however this is an assumption that is not always correct at THz frequencies.

The algorithm assumes that the sample properties does not vary in the z axis. The image consists on a bidimensional reconstruction of a sample slice in the (x, y) plane. Moreover, if the antennas are linearly polarized in the z axis direction, the electric field and the current vectors are described by scalar field equations.

5.1.1 Reconstruction algorithm

The sample physical property that interacts with the electromagnetic waves is its complex permittivity, defined for a lossy material as $\epsilon(\vec{r}) = \epsilon' + j\frac{\sigma}{\omega}$, where σ is the material conductivity. The field scattered by the sample $E_s(\vec{r})$ is defined as

$$E_s(\vec{r}) = E(\vec{r}) - E_i(\vec{r}), \tag{5.1}$$

where $E_i(\vec{r})$ is the electric field impinging to the object and $E(\vec{r})$ is the total field. The scattered field can be expressed as the field generated by the equivalent currents on the sample

$$E_s(\vec{r}) = \iint_S -j\omega\mu_0 J(\vec{r'})G(\vec{r} - \vec{r'})dr', \tag{5.2}$$
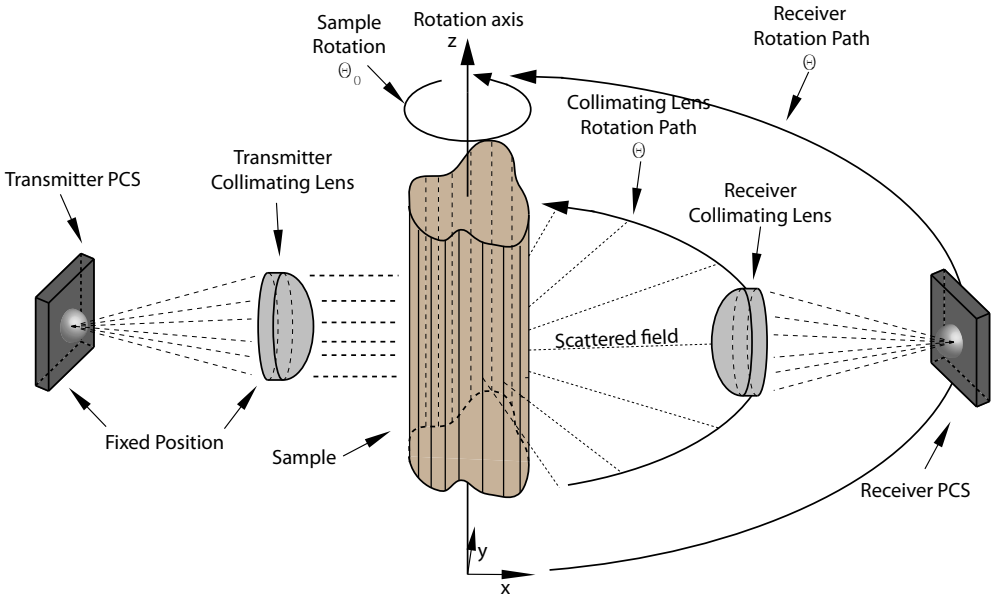
Figure 5.1: 2D simulation geometry consisting on a Rohacell cylinder containing two cylinders filled with two different compounds Ph1 and Ph2.

where $G(\vec{r} - \vec{r'})$ is the Green's function and

$$J(\vec{r'}) = -j\omega(\epsilon(\vec{r'}) - \epsilon_0)E(\vec{r'}) \tag{5.3}$$

is the induced current on the sample. By applying a bidimensional Fourier transform, the angular spectrum of the currents is obtained

$$\tilde{J}(\vec{k}) = \iint_S J(\vec{r})e^{j\vec{k}\vec{r}}d\vec{r}. \tag{5.4}$$

The following assumptions are taken from now on:

- The field scattered by the object is negligible in front of the incident field (Born approximation): $\epsilon(\vec{r}) \approx \epsilon_0$ and therefore $E(\vec{r}) \approx E_i(\vec{r})$

- The object is illuminated by a plain wave with an incidence angle θ_0: $E_i(\vec{r}) = e^{-j\vec{k}\hat{\theta}_0\vec{r}}$ where $\hat{\theta}_0$ is the unit vector in the θ_0 direction.

In addition $\tilde{C}(\vec{k} - k_0\hat{\theta}_0)$ is defined as the bidimensional Fourier transform of the contrast function $C(\vec{r}) = 1 - \frac{\epsilon(\vec{r})}{\epsilon_0}$, Hence, the resulting expression after introducing (5.3) in (5.4) evaluated at $|k| = k_0$ is

$$\tilde{J}(\vec{k}) = -j\omega\epsilon_0\tilde{C}(\vec{k} - k_0\hat{\theta}_0). \tag{5.5}$$

The reciprocity theorem states that the integral of the currents radiating on a volume v_a multiplied by the electric field generated by currents on a volume v_b, is equal to the integral of

the currents radiating on a volume v_b multiplied by the electric field radiating from currents on the volume v_a [84]

$$\iint_{v_a} \vec{J}_a \cdot \vec{E}_b \, dv_a = \iint_{v_b} \vec{J}_b \cdot \vec{E}_a \, dv_b. \tag{5.6}$$

In the scenario shown in Fig. 5.1, it is assumed that J_b corresponds to the currents induced on the sample by the electric field $E_i(\vec{r}; \theta_0)$ and J_a are the currents on the transmitter antenna. In addition, J_b radiates the scattering field $E_s(\vec{r})$ whereas J_a radiates a plane wave $e^{-jk_0\hat{\theta}\cdot\vec{r}}$. Therefore, from (5.3) the currents induced in the sample from the incoming field $E(\vec{r}; \theta_0)$ is described by

$$J_b(\vec{r}) = -j\omega\epsilon_0 C(\vec{r}) E(\vec{r}; \theta_0). \tag{5.7}$$

From (5.5) and using (5.6) the following expression is obtained

$$\tilde{C}(k_0(\hat{\theta} - \hat{\theta}_0)) = j\omega\mu_0 \int_{v_a} J_a(\vec{r}, \theta) E_s(\vec{r}; \hat{\theta}_0) dv_a. \tag{5.8}$$

If a cylindrical measurement geometry as presented in Fig. 5.1 is considered, (5.7) is expressed as

$$\tilde{C}(k_0(\hat{\theta} - \hat{\theta}_0)) = j\omega\mu_0 \int_0^{2\pi} I(\theta - \sigma) E_s(\sigma; \hat{\theta}_0) R d\sigma, \tag{5.9}$$

where $I(\theta - \sigma)$ is the current distribution along an angular position σ of the antenna that radiates a plane wave with θ direction. This current distribution can be expressed, for an arbitrary radius of the cylinder geometry as

$$I(\theta - \sigma) = -\frac{2}{\omega\mu_0 R\pi} \sum_{n=-\infty}^{\infty} \frac{j^{-n}}{H_n^{(2)}(k_0 R)} e^{jn(\theta-\sigma)}, \tag{5.10}$$

where $H_n^{(2)}$ is the Hankel function of the second kind and R is the radius of the cylindrical geometry. In addition, the scattered field considering a plane wave impinging to the object can be expressed as

$$E_s(\sigma; \hat{\theta}_0) = \int_0^{2\pi} I(\theta_0 - \sigma_0) E_s(\sigma; \sigma_0) R d\sigma_0, \tag{5.11}$$

where $E_s(\sigma; \sigma_0)$ is the scattered field measured at an angle σ and produced by a incident wave coming from the direction σ_0.

Considering that both receiver and transmitter antennas are placed further than the farfield distance from the sample ($R >> \frac{2D^2}{\lambda}$), (5.10) can be approximated asymptotically by

$$I(\theta - \sigma) = -\sqrt{\frac{2k_0}{\pi R\omega^2\mu_0^2}} \delta(\theta - \sigma) e^{-j(k_0 R - \frac{\pi}{4})}, \tag{5.12}$$

where $\delta()$ is the Dirac delta function. Finally, by applying (5.12) and (5.11) to (5.9), the resulting expression is

$$\tilde{C}(k_0(\hat{\theta} - \hat{\theta}_0)) = \frac{2Re^{-jk_0 R}}{Z_0\pi} \int_0^{2\pi} \int_0^{2\pi} \delta(\theta - \sigma)\delta(\theta_0 - \sigma_0) E_s(\sigma; \sigma_0) d\sigma d\sigma_0, \tag{5.13}$$
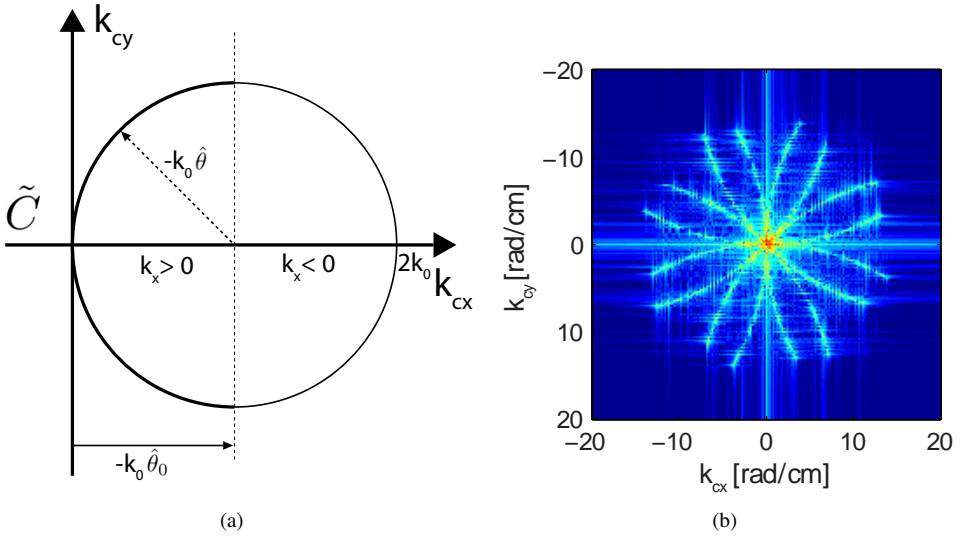
Figure 5.2: (a) Angular spectrum of the contrast function $C(\vec{r})$ for a fixed incidence angle θ_0. The black curve corresponds to the contrast profile given by the forward scattered field $(-90 < \theta < 90)$ deg. (b) Angular spectrum of a reconstructed image for $\theta_0 = 45n$ deg where $1 \leq n \leq 8$ and $-30 \leq \theta \leq 30$ deg.

where the final result after the integration is

$$\tilde{C}(k_0(\hat{\theta} - \hat{\theta}_0)) = \frac{2Re^{-jk_0R}}{Z_0\pi} E_s(\theta;\theta_0). \tag{5.14}$$

Figure 5.2(a) shows an schematic that illustrates how the measured field is translated to the angular spectrum of the sample image contrast. The electric field value $E_s(\theta;\theta_0)$, scattered by the sample in the direction θ_0 when an incident plane wave impinges from the direction θ, corresponds to the contrast spectrum value with angular coordinates $\vec{k}_c = k_0(\hat{\theta} - \hat{\theta}_0)$. It should be pointed out that the high frequency part of the spectrum is filled with the electric field values backscattered by the sample given by receiver antennas placed at $\theta \approx -\theta_0$ (reflection geometry), yielding a maximum frequency of $2k_0$. The low frequency part of the spectrum corresponds to forward scattered electric field and is measured when the receiver antennas are placed at $\theta \approx \theta_0$ (transmission geometry).

Figure 5.2(b) shows the spectrum of a retrieved image. It corresponds to a reconstruction of a measurement with $\theta_0 = 45n$ with $n = 1...8$ and $-30 < \theta < 30$ in steps of 1 deg. Note that the semi-circles are not well defined since the spectrum is convolved by the spectral response of the rectangular window applied due to the truncation of the reconstructed image.

5.2 Imaging scenario simulations

This section includes electromagnetic simulations that are used to foresee the behavior of the algorithm in the THz range for a certain scenario. The Finite Element Method (FEM)

simulator COMSOL Multiphysics [85] has been used to obtain the scattered fields for several incident and reception angles. In order to simplify the simulation and due to the high simulation frequency a two-dimensional geometry has been used. This geometry assumes uniformity in the z-axis, reducing the physical space where the electric field should be calculated. This simplification of the problem is crucial to enhance the acquisition speed in scenarios of several tens of wavelengths.

5.2.1   Simulation scenario

Figure 5.3 shows the geometry introduced into the simulator to retrieve the scattered fields. It consists on several cylindrical sections that represents different materials in a two-dimensional geometry. The main sample consists on a $12\,\mathrm{mm}$ diameter cylinder of Rohacell material ($\epsilon_r \approx 1.05$) where two inner-cylinders have been filled with two different materials Ph1 and Ph2. Both materials have the same real permittivity but different loss tangent $\epsilon_r = 1.7(1 - j \tan(\delta))$ given by Fig. 5.4. The loss tangent is zero for all the simulated frequency range except at $500\,\mathrm{GHz}$ and $600\,\mathrm{GHz}$ for the material Ph1 and Ph2 respectively. The objective of introducing this dependance of the loss tangent with the frequency is to model absorption resonances in the materials. The scenario includes an air section that ends in a Perfect Matched Layer (PML). The PML absorbs the scattered radiation avoiding undesired back-reflections, thus emulating a free-space environment.

As an excitation, a plane wave depending on the incidence angle θ_0 as

$$E_{iz}(\theta_0) = e^{-jk_0(x\cos(\theta_0) + y\sin(\theta_0))} \tag{5.15}$$

is included in the model. The currents induced by the plane wave in the outer part of the main cylinder are calculated by the solver. As a post-processing stage, the far-field radiated by the induced currents are evaluated and are given as a main output of the simulator. The algorithm presented in Section 5.1.1 is applied to the fields scattered by the object to reconstruct the image. The complete set of measurements are acquired in a three-dimensional matrix with indexes (f, θ_0, θ), where $f = 100, 200...800\,\mathrm{GHz}$; $\theta_0 = 0, 45, 90...315\,\mathrm{deg}$ and $\theta = 0, 0.5, 1, ...359.5\,\mathrm{deg}$ with a total number of 46080 electric field points.

5.2.2   Spectroscopic imaging

In order to test the algorithm with a canonical shape, a first set of images that not include the materials Ph1 and Ph2 have been reconstructed. In this case, the inner-cylinders have been filled with air instead. Figure 5.5 shows the retrieved images frequency by frequency from $100\,\mathrm{GHz}$ to $800\,\mathrm{GHz}$. The outer shape of the main cylinder is retrieved in all the images. However, the shape of the inner-cylinders change drastically with the frequency. As the frequency increases, the shape of the inner-cylinders is not well retrieved and for frequencies greater than $500\,\mathrm{GHz}$ there is no clear difference in the image that leads to the identification of the inner-cylinders. The image quality is reduced as the simulation frequency is increased since the Born approximation loses validity. As the frequency is increased, the scattered field is concentrated in values of θ close to the forward-scattering point (or pure transmission point). This causes that the high spatial frequencies of the image are not properly retrieved, translated into a poor reconstruction of the abrupt changes in the image.
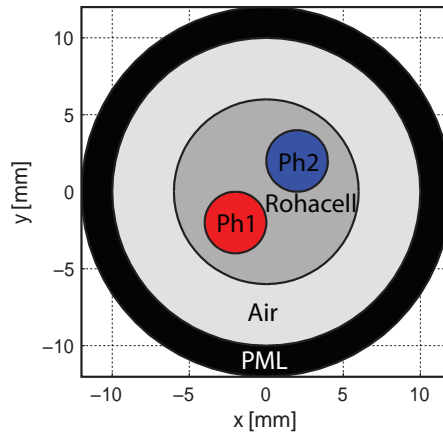
Figure 5.3: 2D simulation geometry consisting on a Rohacell cylinder containing two cylinders filled with two different compounds Ph1 and Ph2.
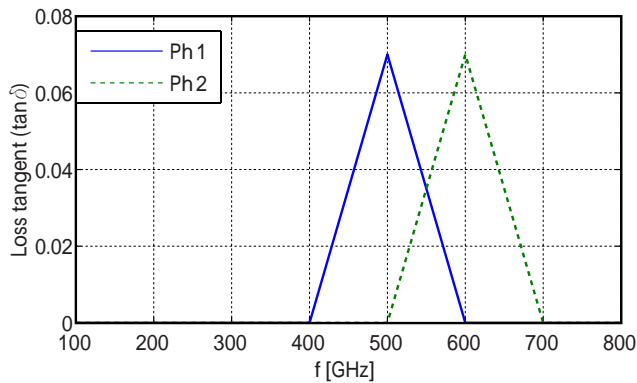

Figure 5.4: Loss tangent against the frequency of the compounds Ph1 and Ph2.

In a second simulation trial, the materials Ph1 and Ph2 have been introduced in the scenario in order to study the impact of the frequency-variable loss-tangent in the reconstruction. Figure 5.6 shows the retrieved images for each frequency. It should be pointed out a main difference with respect the reconstruction of the images appearing in Figure 5.5: the reception angle spans from -30 to $30\,\mathrm{deg}$ instead of covering the whole circumference. This restriction in the reception angle has been introduced to simulate the measurements capabilities of our system as will be described in Section 5.3.2. At first sight, it can be noted that the spatial resolution of the images strongly depends on the frequency. As the frequency increases the spatial resolution increases as well. This effect in the images is more noticeable in the images of Fig. 5.6 than in the ones appearing in Fig. 5.5 due to the restriction in the reception angle. Regarding the appearance of the materials Ph1 and Ph2 in the image, no change is observed depending on the frequency except at $500\,\mathrm{GHz}$ and $600\,\mathrm{GHz}$ where the absorption peaks of the materials are placed. The image retrieved at $500\,\mathrm{GHz}$ shows a clear attenuation
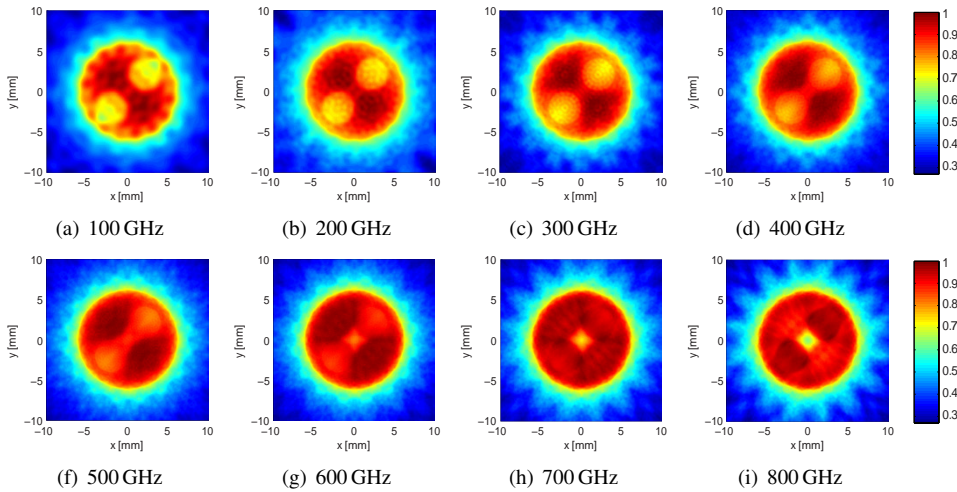
Figure 5.5: Reconstructed images from the tomographic simulation of the scene shown in Fig. 5.3, however in this simulation the pharmaceutical compounds have not been considered and the inner-cylinders are filled with a air. Each image corresponds to a reconstruction of the contrast at a single frequency: (a) 100 GHz, (b) 200 GHz, (c) 300 GHz, (d) 400 GHz, (f) 500 GHz, (g) 600 GHz, (h) 700 GHz, (i) 800 GHz.

Figure 5.6: Reconstructed images from the tomographic simulation of the scene shown in Fig. 5.3. In this case both compounds Ph1 and Ph2 have been considered in the reconstruction. Each image corresponds to a normalized contrast reconstruction at a single frequency: (a) 100 GHz,(b) 200 GHz, (c) 300 GHz, (d) 400 GHz, (f) 500 GHz, (g) 600 GHz, (h) 700 GHz, (i) 800 GHz.

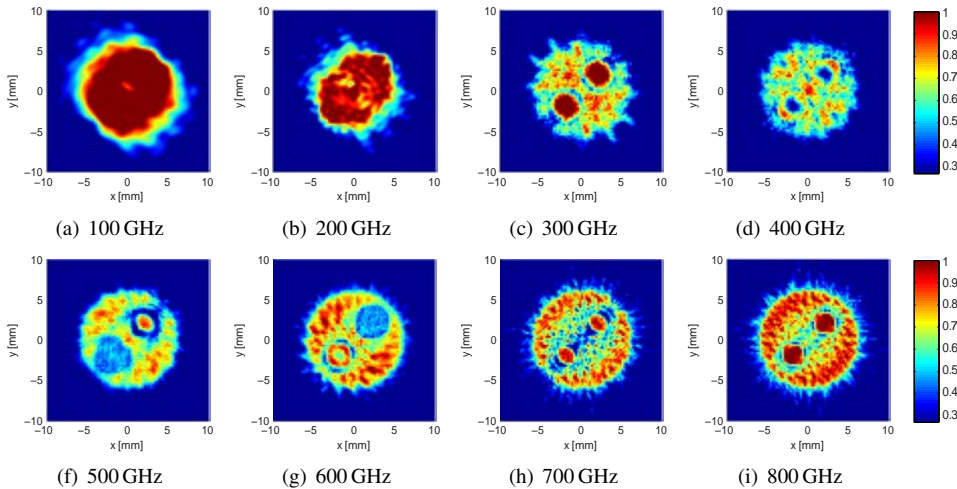in the zone where the material Ph1 is placed whereas at 600 GHz the attenuation is shown in the place where the material Ph2 is located. Hence, the variation in loss tangent has a clear effect on the images and can be foreseen that a material with a certain absorption peak can be
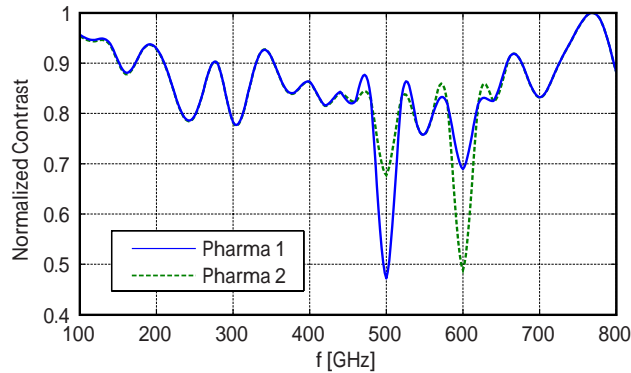
Figure 5.7: Reconstructed contrast depending on the frequency for both materials. The contrast has been integrated along the area defined in Fig. 5.3 by the material Ph1 and Ph2 for the blue (continuous) and green (dotted) lines respectively.
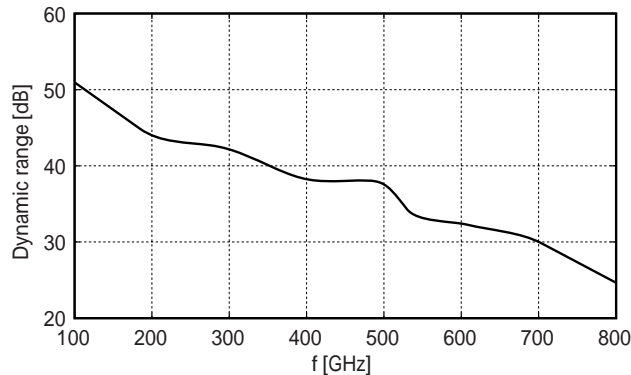
Figure 5.8: Dynamic range of the imaging setup based on the THz-CW system depending on the frequency.

identified in the image by using the proposed tomographic algorithm.

Additionally, the frequency response of the materials can be obtained by integrating the zone where it is located against the frequency. Figure 5.7 shows the dependence with the frequency of integrating the contrast zone where the materials Ph1 and Ph2 are located. The attenuation points agree with the loss tangent peaks in each material. Thus, the spectroscopic response of the materials can be extracted from the images. However, since the Born approximation is not fulfilled due to the high contrast of the materials Ph1 and Ph2 with the Rohacell, the images do not provide quantitative information. Therefore parameters such material concentration cannot be provided by the images and only qualitative information can be obtained.

An additional simulation has been performed introducing additive Gaussian noise to the simulated results in order to achieve the same dynamic range as the one provided by the measurement setup. Figure 5.8 shows the measured dynamic range of the imaging setup that

(a) 100 GHz   (b) 200 GHz   (c) 300 GHz   (d) 400 GHz

(f) 500 GHz   (g) 600 GHz   (h) 700 GHz   (i) 800 GHz
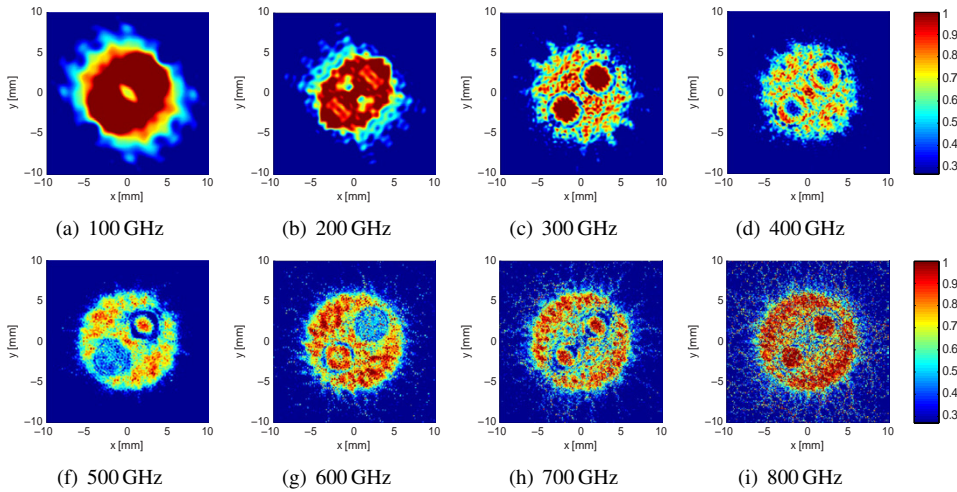
Figure 5.9: Reconstructed images from the tomographic simulation of the scene shown in Fig. 5.3 adding complex Gaussian noise to the simulation to achieve the dynamic range shown in Fig. 5.8. Both compounds Ph1 and Ph2 have been considered in the reconstruction. Each image corresponds to a normalized contrast reconstruction at a single frequency: (a) 100 GHz,(b) 200 GHz, (c) 300 GHz, (d) 400 GHz, (f) 500 GHz, (g) 600 GHz, (h) 700 GHz, (i) 800 GHz.
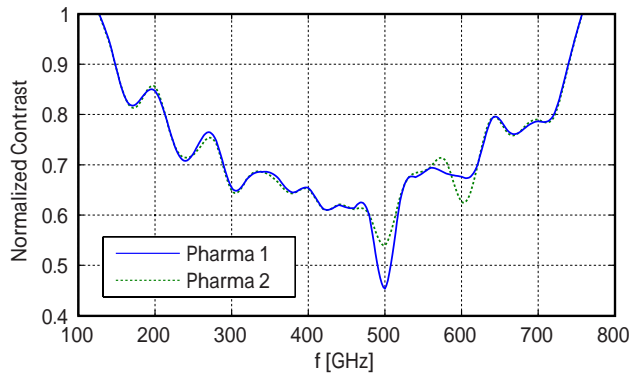
Figure 5.10: Reconstructed contrast depending on the frequency for both materials introducing additive Gaussian noise. The contrast has been integrated along the area defined in Fig. 5.3 by the material Ph1 and Ph2 for the blue (continuous) and green (dotted) lines respectively.

is described in Section 5.3.1. It can be shown that as the frequency increases the dynamic range decreases, starting from $50\,\mathrm{dB}$ at $100\,\mathrm{GHz}$ to $25\,\mathrm{dB}$ at $800\,\mathrm{GHz}$.

If an additive Gaussian noise is added to the simulated electric field used to obtain the images shown in Fig. 5.6, the resulting reconstructed images are presented in Fig. 5.9. It can be noted that the reconstruction of the high frequency simulations yield noisy images since the dynamic range is reduced to about $25\,\mathrm{dB}$. Nevertheless, the spectroscopic behavior of the samples is still perceived. This confirms the suitability of the measurement system, in terms

of dynamic range, to measure the samples equivalent to the simulated ones.

The result of integrating the zones where both materials are located is shown in Fig. 5.10. Despite the perception of the absorption characteristic of both materials is reduced, the peaks at $500\,\mathrm{GHz}$ and $600\,\mathrm{GHz}$ for Ph1 and Ph2 respectively can be noted. From these simulations can be concluded that, despite the reduction of dynamic range hinders the reconstruction of the spectral behavior of the sample by the algorithm, still the detection and identification of the materials can be performed.

5.3 Measurements

In order to validate the simulations and to study the performance of the algorithm with real data, a set of measurements of different samples has been performed. The data required to reconstruct the image has been measured using a THz-CW spectroscopy system whereas the spectroscopic characterization of the sample has been performed using a Terahertz Time-Domain Spectroscopy (THz-TDS). Since both equipments are available in our laboratory, the most suitable one has been chosen for each operation.

On the one hand the THz-TDS setup provides a better frequency accuracy than the THz-CW due to the high precision of the delay stage incorporated in the system [27]. In addition, the complete spectral response in amplitude and phase can be obtained from a sample using two measurements: a reference and sample measurements. As a result, a complete spectral information of the sample can be obtained in 15 minutes approximately and with high accuracy.

On the other hand the THz-CW system used in this thesis relies on thermal tuning of the optical frequency to shift the photomixed THz frequency [86]. The system software incorporates a calibration file that associates a certain laser temperature to an output optical frequency. The resulting THz radiation is given as a result of the photomixing of two laser frequencies with a separation equal to the THz frequency: $f_{\mathrm{THz}} = f_{l2} - f_{l1}$ where f_{THz} is the THz frequency whereas f_{l2} and f_{l1} are the frequency of each laser source. Hence, by using thermal tuning f_{l2} can be increased and f_{l1} can be decreased yielding a increment of f_{THz} or viceversa. Hence, the frequency accuracy relies on calibration quality of the system and on its repeatability throughout time. In addition, due to the inherent inertia of the thermal tuning, once a certain objective temperature is set in the laser controllers, around 15 minutes should be waited until the frequency is properly set. Therefore, it makes extremely slow the acquisition of multiple frequency point with complex data information.

Nevertheless, two main advantages makes this system a good choice for tomography: 1) the system is fiber-coupled, allowing a complete free movement of the photomixers as required by the tomographic algorithm; and 2) once a certain frequency is set, a complex data measurement lasts 1 second whereas in the THz-TDS the whole frequency spectrum should be retrieved, even when only one frequency is required.

The following sections describe the measurement methodology required to obtain the field scattered by the sample intended to be imaged. Additionally, several image reconstructions that validate the algorithm are shown.

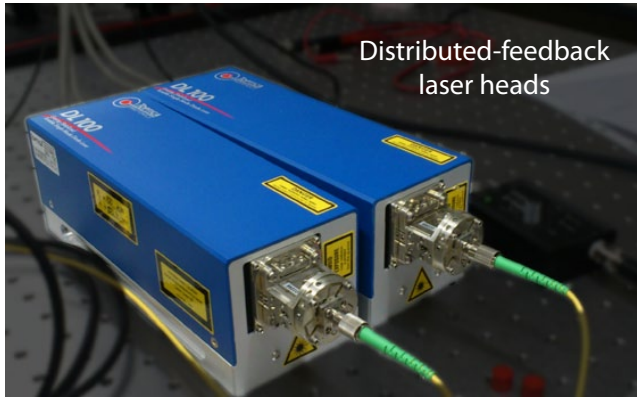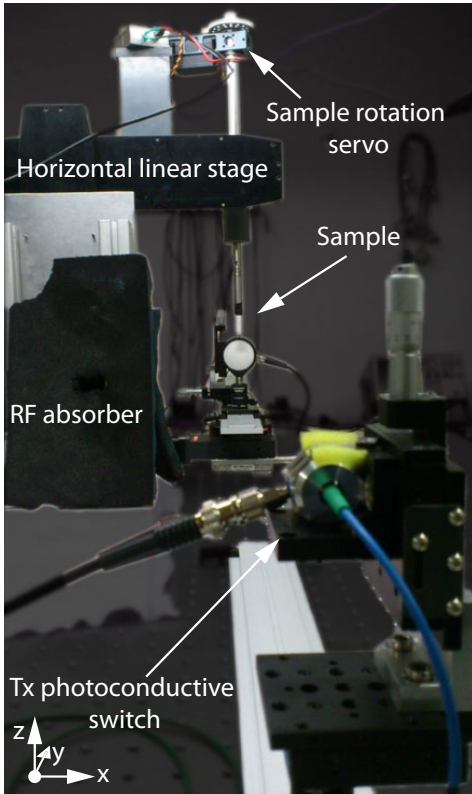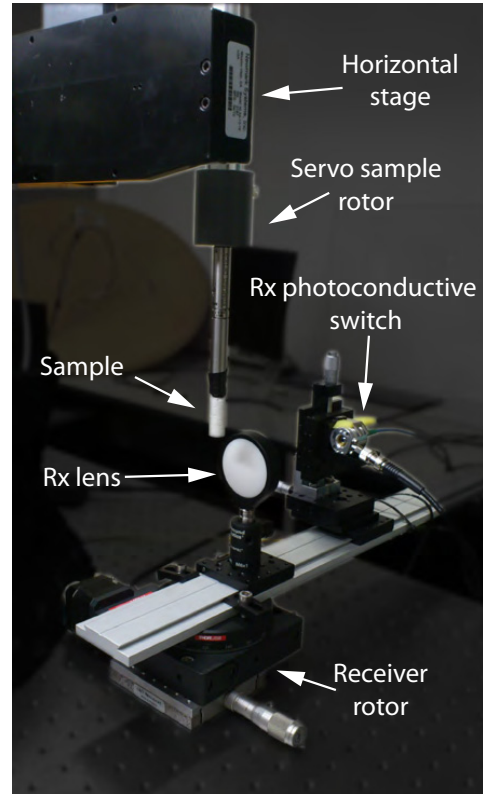**Figure 5.11:** Photograph of the THz-CW system laser heads.

(a)   (b)

Figure 5.12: Photographs of the tomographic measurement setup . The main components of the system are presented in the photographs.

5.3.1   Setup and sample preparation

The setup shown schematically in Fig. 5.1 has been implemented in the laboratory. As mentioned in the last section, a THz-CW system has been used to acquire the multiple field points required to reconstruct the image. The Distributed Feedback (DFB) lasers used to produce the two optical tones with frequency f_{l1} and f_{l2} are shown in Fig. 5.11. Both optical signals are coupled using a $2x2$ optical coupling matrix, whose two outputs are the combination of the two inputs signals, and driven to the receiver and transmitter PCS using fiber optics. Figure 5.12 shows photographs of the measurement setup describing the main components.

In Fig. 5.12(a), the transmitter photoconductive switch antenna. Note the fiber optics with blue protective cover that couples the laser power into the antenna. Also the coaxial cable in charge of biasing the antenna with a $13V$, $7\,kHz$ square signal is shown. The photoconductive switch is mounted on two micrometer stages that allow vertical (z-axis) and horizontal (x-axis) displacement of the antenna. Furthermore, the whole antenna mount is held on a rail that allows a continuous displacement in y-axis.

The sample is held by an optical post that is rotated by a winch servo. This servo, after a proper calibration, can be rotated $360\,°$ with an accuracy around $1\,°$. The control of the servo is made by using a commercial control board *Pololu Maestro 6-channel* than can be connected to a computed by a Universal Serial Bus (USB) port. A Polyvinyl Chloride (PVC) structure holds the servo to a two-dimensional $300x300\,mm^2$ horizontal linear stage used to translate the sample. During the measurement, the sample is translated to two different positions: 1) the measurement position, where the servo rotation axis and the receiver rotation axis match; and 2) the empty chamber position, where the sample is translated to a maximum x-axis and z-axis value to avoid any intrusion of the sample in the measurement. Note in the Fig. 5.12(a) that an absorber has been placed covering the two-dimensional stage, trying to avoid undesired reflection from the metal parts that compose and hold the stages. A special care with undesired reflections has been taken at low frequencies where the transmitted beam covers a wide area. As the frequency is increased, the divergence angle of the beam is decreased and the amount of undesired reflections decrease.

Figure 5.12(b) shows the receiver components of the setup placed on a rail. A Teflon plano-convex lens has been used to capture the plane wave scattered by the sample. The scattered radiation is then concentrated on the receiver photoconductive switch aperture. A fiber-optics is used, as in the transmitter PCS, to couple the laser in the receiver PCS. However, in the receiver antenna, the coaxial cable does not bias the antenna but collects the photo-induced current. The received current is amplified by a Transimpedance Amplifier (TIA) and driven to the input of the lock-in amplifier. Since the receiver components should be rotated around the sample, the rail is held on a rotation stage with the same rotation axis as the sample rotation servo. This rotation stage is controlled via a USB port with the computer.

In the electronics reception stage, a lock-in amplifier is in charge of demodulate the received voltage given by the TIA. The THz electric field has been previously modulated at $7\,kHz$ by the bias of the transmitter PCS, therefore the photo-induced current is as well modulated at the same frequency. The lock-in amplifier gets locked to the modulation frequency and retrieves the amplitude value of the signal. This technique is commonly used to improve the Signal to Noise Ratio (SNR) of the retrieved signal, that otherwise would be masked by
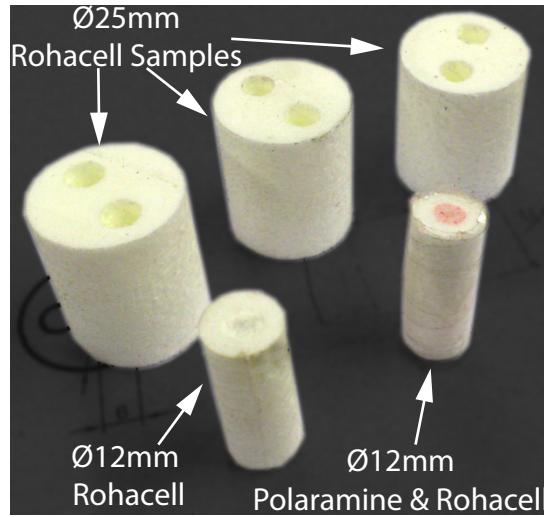
Figure 5.13: Photograph of the different Rohacell blocks used as a sample for image reconstruction.

Flicker or $1/f$ noise. This method displaces the spectrum of the received signal out of the influence of the Flicker noise achieving a better SNR in the reception.

In a final reception step, the signal at the output of the lock-in is introduced in a Analog-to-Digital Converter (ADC) that is connected via a USB port to the computer. Note that the whole measurement setup can be controlled with one computer allowing a fully automatic acquisition of the several samples needed for the image reconstruction.

Regarding the samples preparation, the material chosen to build the samples is Rohacell ($\epsilon_r = 1.05$). Figure 5.13 shows the different sample structures built to serve as a holder for the pharmaceutical compound in the spectroscopic imaging process. In the image three different structures are presented: 1) a $12\,\text{mm}$ diameter solid Rohacell cylinder; 2) a $12\,\text{mm}$ diameter Rohacell cylinder filled with Polaramine in a inner-cylinder of $6\,\text{mm}$ diameter; and 3) a $25\,\text{mm}$ diameter Rohacell cylinder with two empty inner-cylinders of $6\,\text{mm}$ diameter. Several images have been taken from the described samples, varying the position and the content in order to validate the reconstruction algorithm.

5.3.2   Complex data acquisition

The algorithm described in Section 5.1.1 requires complex information of each measured electric field point in order to reconstruct the image from the scene. However, the THz-CW system used to measure the field data does not provide direct information of amplitude and phase of the THz. The resulting parameter given by the system is a Direct-Current (DC) voltage signal V_m related with

$$V_m(A, \phi) = A \cos\left(k_{\text{FO}}\Delta l_{\text{FO}} + k_{\text{THz}} r_{\text{THz}} + \phi\right), \tag{5.16}$$

where A is the THz signal amplitude, k_{FO} is the wavenumber in the fiber optics, Δl_{FO} is the length difference of the section of fiber optics going from the 2x2 optical coupler to the PCS,
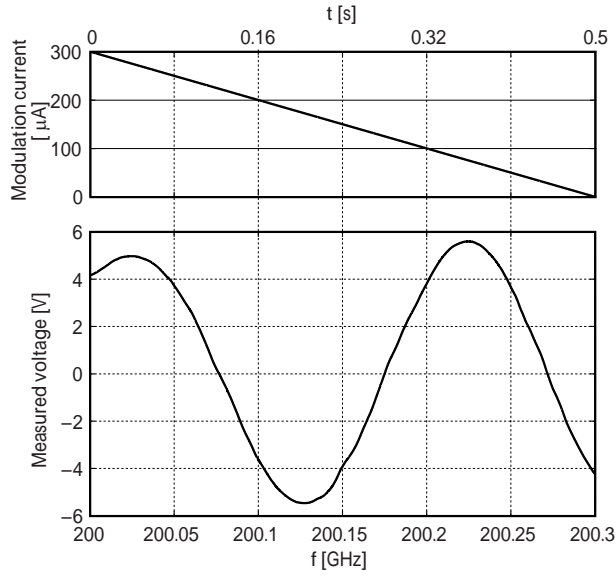
Figure 5.14: Acquisition trace from one trigger signal. The top Figure shows the laser modulating current ramp whereas the bottom Figure shows the variation on the THz frequency produced by the modulation.

k_{THz} is the wavenumber in the THz path (free-space), r_{THz} is the length of the THz path and ϕ is the phase of the THz electric field. Note that the spectral response of the system is no considered in (5.16).

With a single measurement, the value of A and ϕ cannot be retrieved. In practice three different techniques can be used to retrieve the amplitude and phase of the complex THz signal:

1. Either the receiver or transmitter PCS can be mounted on a mechanical delay stage that translates the antenna $90\,°$ at the working frequency. Hence, two measurements are done: 1) V_m^0 without delay; and 2) V_m^{90} with $90\,°$ of delay. Using both measurements, the complex information can be obtained as $A = \sqrt{(V_m^0)^2 + ((V_m^{90})^2}$, and $\phi = \arctan(\frac{V_m^{90}}{V_m^0})$. The main drawback of this method is the necessity of an extra linear stage to perform the delay, adding extra mechanical movements that may slow down the acquisition speed.

2. The frequency of the THz radiation is swept few megahertz by thermal tuning of the laser frequency. In this case a set of points of $V_m(k_{\text{THz}})$ for $k_{\text{THz}} = \{k_{\text{THz}}^0, k_{\text{THz}}^0 + \Delta k, ..., k_{\text{THz}}^0 + n\Delta k\}$, while the remaining parameters that govern V_m are considered constant. Hence the term $k_{\text{FO}}\Delta l_{\text{FO}}$ is added as a constant phase to ϕ, yielding $\phi_0 = \phi + k_{\text{FO}}\Delta l_{\text{FO}}$. In order to retrieve the value of A and ϕ_0, two different techniques have been tested: 1) a fitting of the cosine function is performed retrieving the value of amplitude and phase; and 2) a Fourier transform of the received signal is performed and amplitude and phase of the maximum returned value are considered. Note that

in both cases the sampling should fulfill Nyquist in order to avoid ambiguities in the estimation, since no information a priori of k_{THz} is known.

In practice this method does not give good results due to the uncertainty in the thermal tuning. The precision required in the tuning is on the order of few MHz, far beyond the precision given by the laser temperature controller. In addition, the thermal tuning is slow due to the inertia inherent to thermal systems.

3. As in the method described in the point 2, k_{THz} is swept but instead of using thermal tuning, a laser current modulation is used. The frequency of one of the lasers can be modulated by introducing a slight variation on its biasing current. This effect is directly translated to k_{THz}. In particular, the modulation ratio of the lasers of the THz-CW system is $1\,\mathrm{GHz/mA}$. Figure 5.14 shows the effect of a current modulation ramp of $300\mu A$ in the measured voltage.

After a set of tests of the methods explained in points 2 and 3, the latter has been chosen due to its precision and fast acquisition speed. This method yields a complex electric field measurement each $0.5\,\mathrm{s}$, and can be speeded up by reducing the period of the modulating ramp. However, in our case the maximum speed is limited by the minimum integration time of the lock-in amplifier and by the required noise level. A good tradeoff has been found setting the ramp period to $0.5\,\mathrm{s}$ and the time constant of the lock-in amplifier to $10\,\mathrm{ms}$. Once the whole voltage trace is acquired, the amplitude and phase of the signal is obtained by performing the Fourier transform of the data and selecting the point with maximum amplitude, as described in the point 2.

It has to be pointed out that the synchronization between the function generator used to create the current ramp and the ADC should be precise in order to maintain the repeatability of the phase measurements throughout time. The synchronization has been achieved by using a hardware trigger that creates a positive voltage edge at the beginning of each ramp starting a new acquisition of the ADC.

5.3.3   Data calibration

The tomographic algorithm requires, for each reconstruction frequency, a system with two rotation movements: the sample rotation with angle θ_0 and the receiver PCS rotation with angle θ. Both rotations share the rotation axis of the sample rotation servo. In the measurement process, the sample rotation angles have been set to $\theta_0 = \{0, 22.5, 45, ..., 337.5\}\,\mathrm{deg}$, yielding a number of 16 different sample angles. For each sample angle θ_0, 61 receiver angles are swept $\theta = \{-30, -29, ..., 0, ..., 29, 30\}\,\mathrm{deg}$. Considering the 9 different frequencies acquired $f = \{100, 200, 300, 400, 500, 534, 600, 700, 800\}\,\mathrm{GHz}$, the total number of acquisition is 9351 electric field points if the empty chamber and calibration points are considered.

Figure 5.15 shows the evolution of the phase of the system throughout time. A large phase drift is observed in the time of a complete acquisition for a certain frequency (90 minutes). The Fig. shows the necessity of phase calibration to reconstruct the measurement since the phase drift of the system would mask the phase variation caused by the sample. In order to calibrate the measurement, some calibration points should be taken. The following data acquisition sequence describe the acquisition order of the calibration points and the empty chamber:
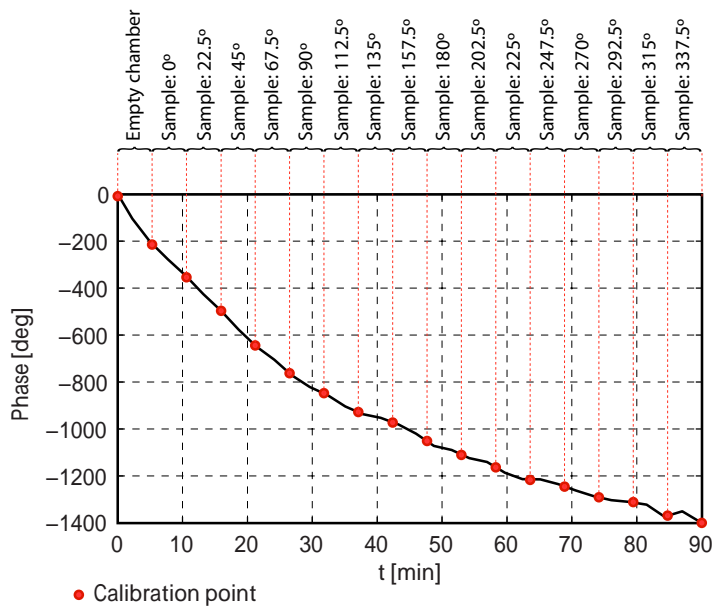
Figure 5.15: Calibration curve interpolated from the acquired calibration points. The measurement intervals depending on the sample position are also shown.

1. Set the desired frequency by thermal tuning.

2. Wait 50 minutes until the inertia of the system is residual and the phase of the signal is stable.

3. Translate the sample to a position where does not interfere in the electric field and measure a calibration point at $\theta = 0°$.

4. Measure the empty chamber by acquiring the 61 points of θ.

5. Measure a calibration point at $\theta = 0°$.

6. Move the sample to the measurement position, set $\theta_0 = 0°$ and perform the whole set of measurements of θ.

7. Repeat actions 3 and 6, increasing the value of θ_0 until $\theta_0 = 337.5°$.

8. Translate the sample to a position where does not interfere in the electric field and measure the final calibration point at $\theta = 0°$.

An schematic of the acquisition sequence is shown in Fig. 5.15 where the calibration points and the time slots where the acquisition points for different θ_0 are depicted. The phase drift curve of the system can be obtained by interpolating the calibration points. Since the acquisition time instant is stored for each electric field point, the phase can be compensated point by point by normalizing the electric field by the phase at a certain time instant. Several tests without phase calibration have been performed without success. In those cases
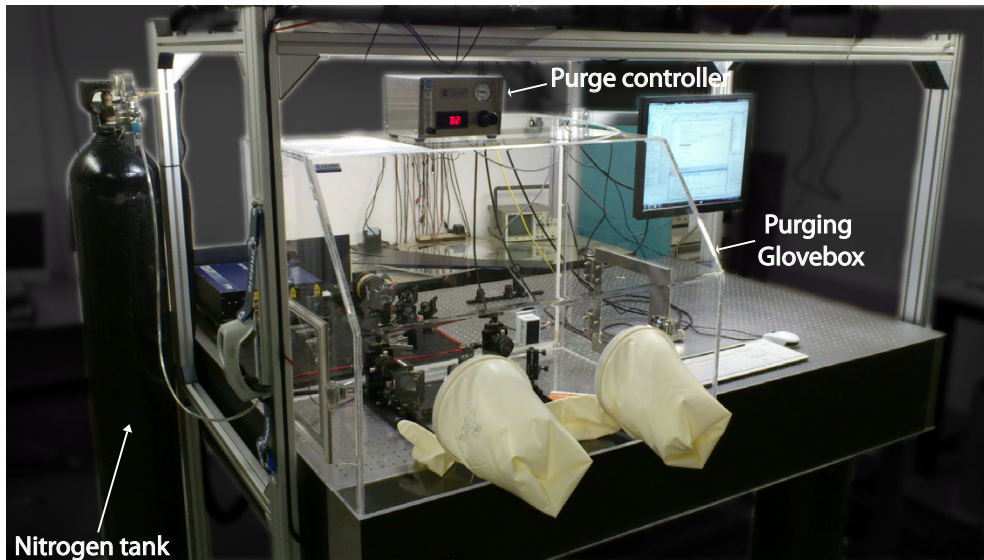
Figure 5.16: Photograph of the Time-Domain spectroscopy system placed on an optical table. The THz path is placed inside a hermetic sealed glovebox used to purge the environment to reduce the water vapor.

the reconstruction of the scenario yields an image consisting in pure noise. However, if a proper calibration is performed, the phase drift can be completely compensated with a residual phase noise estimated in $10\,^{\circ}$. The residual noise has a random behavior and can come from the phase noise of the lasers or caused by instabilities in the thermal control. In any case, this phase noise does not apparently distort the images as will be shown in Section 5.3.

5.3.4 Spectroscopic characterization

A pharmaceutical compound with commercial name Polaramine Repetabs has been chosen as a pharmacological sample to perform the spectroscopic imaging measurements. The active ingredient is Dexclorfeniramine Maleate, a histamine antagonist. The Polaramine has been chosen as a sample due to two reasons: 1) it can be obtained without medical prescription; and 2) it has a high content on $\alpha - lactose$ (main excipient). The molecular interaction of the $\alpha - lactose$ with the electromagnetic waves has been already studied in [87] resulting in a rotational mode at $0.525\,\mathrm{THz}$, two translation modes at $0.993\,\mathrm{THz}$ and $1.110\,\mathrm{THz}$, and a rotational mode at $1.32\,\mathrm{THz}$. Therefore the Polaramine is a good candidate for spectroscopic imaging since it has absorption peaks distributed along the THz frequency band. Nevertheless, we will center out attention in the absorption produced at $525\,\mathrm{GHz}$.

A THz-TDS system has been used to characterize the response of the pharmacological compound in the THz band. Figure 5.16 shows a photograph of the measurement system placed on an optical table. An hermetically sealed glovebox has been used to create an atmosphere with a controlled value of humidity. The air humidity in THz path should be as low as possible to avoid the effect of the multiple water vapor absorption peaks in the spectrom-
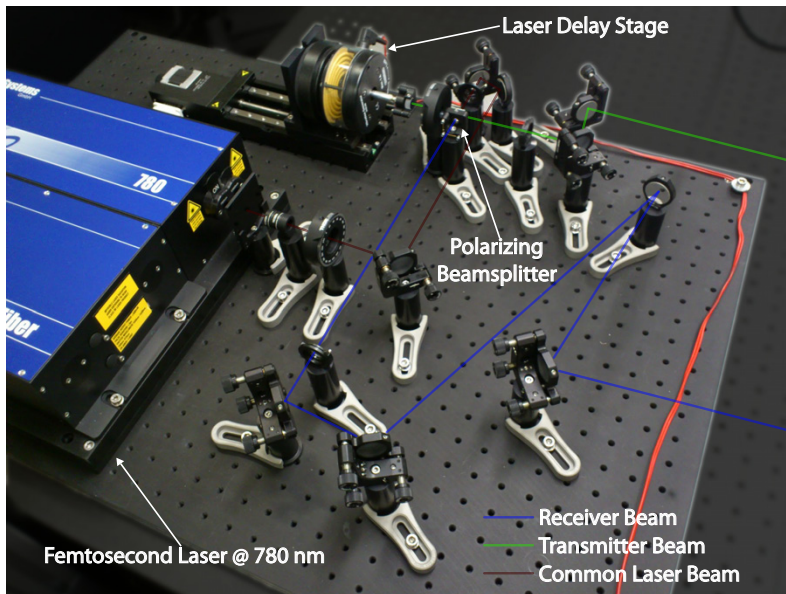
Figure 5.17: Optical path of the Time-Domain system. The femtosecond laser, the delay sage and the various optical components are shown in the image.
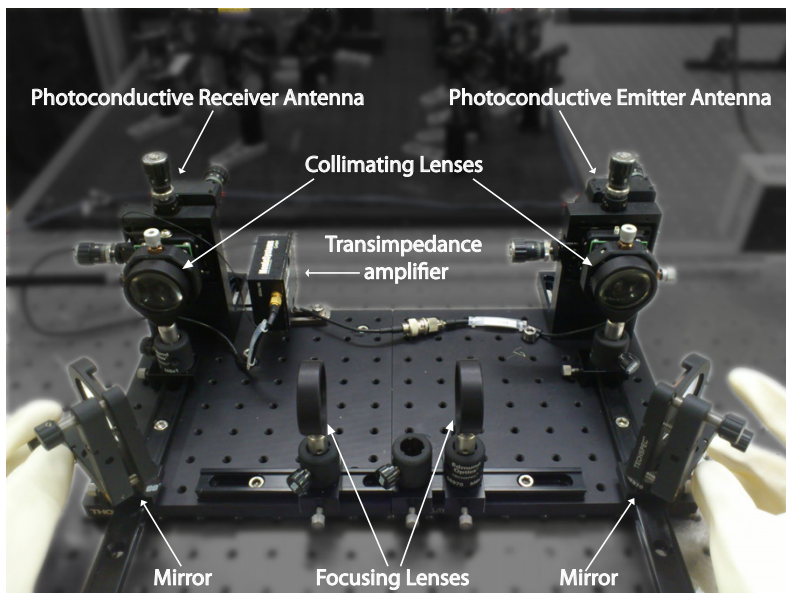

Figure 5.18: Terahertz path of the Time-Domain system. The image describes the main components of the THz path.

eter response. The control has been achieved by purging with nitrogen gas the water vapor contained in the ambient air. Note that the purging system composed by a nitrogen tank and a purge control unit are also shown in Fig. 5.16. Since only the THz path should be purged, the transmitter and receiver optical paths are kept outside of the glovebox, introducing the laser beams through the acrylic back panel.

The optical subsystem of the spectrometer is shown in Fig. 5.17. The femtosecond laser, the optical delay stage and the multiple optical mirrors and accessories composing the subsystem are shown in the photograph. In addition, the path of both receiver and transmitter laser beams are shown in blue and green respectively. At the right of the image, the beams are aimed directly to the photoconductive antennas placed inside the glovebox. The antennas are shown in Fig. 5.18 together with lenses in charge of collimating and focusing the THz beam, two mirrors that rotate the beam $90\,°$ and a TIA. The Polaramine powder is placed using a sample holder in between both focusing lenses in order to perform the measurement.

The technique used to measure the spectrum of the sample is the one usually used in a THz-TDS:

- The THz pulse is sampled by using the optical delay stage. The linear step of the stage Δx is translated to a temporal step in the sampled pulse of of $\Delta t = 2\Delta x/c$, where c is the speed of light.

- The voltage given by the TIA is processed by the lock-in amplifier and acquired using a ADC. For each step of the linear stage a voltage value is acquired, resulting in a total of N_p points.

- Once the complete pulse is retrieved, a Discrete Fourier Transform (DFT) is performed in order to obtain the frequency spectrum of the measurement.

The maximum frequency value and the frequency resolution are given by the properties of the DFT. Therefore, the maximum frequency value is: $f_{\max} = \frac{1}{2\Delta t}$; and the frequency resolution is given by the maximum time span: $\Delta f = \frac{1}{\Delta t N_p}$. Figure 5.19 shows the measured spectrum of the system without sample with two different humidity levels: 30% and 2%. In this measurement, $\Delta t = 0.125\,\text{ps}$ whereas the number of points is $N_p = 200$. The water vapor absorption peaks appear in the curve corresponding to the measurement with 30% of humidity. Note the drastic reduction of the peaks in the purged measurement. This Figure shows that a purged measurement should be performed when the expected absorptions of the sample are close to the water vapor absorptions, otherwise the measurement will be masked.

Figure 5.20 shows the measured absorption spectrum of a Polaramine sample. The measurement with the sample is normalized by the free-space measurement in order to eliminate the response of the system from the measurement. Moreover, the linear response of the scattering produced in the sample has been retrieved by using a linear regression and subtracted from the measurement. As expected, an absorption line appears at $525\,\text{GHz}$, confirming the pharmaceutical as a good candidate for spectroscopic imaging.

It has to be pointed out that the response expected at the frequency of $0.993\,\text{THz}$ is not noticeable since it is masked by noise. Despite the dynamic range of the system at $1\,\text{THz}$ is close to $50\,\text{dB}$, the high scattering produced by the pharmaceutical powder attenuates the signal around $45\,\text{dB}$ at $1\,\text{THz}$. This problem can be overcome by using a press to compact the powder.
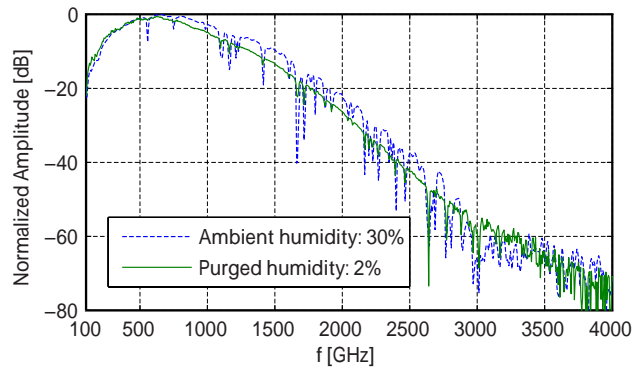
Figure 5.19: Characterization of the signal spectrum produced by the THz-TDS system available in the AntennaLab THz laboratory. The spectrum has been measured with two different humidity levels: 30 % and 2 %. The reduction in the level of the water vapor absorption peaks is clearly noticeable.
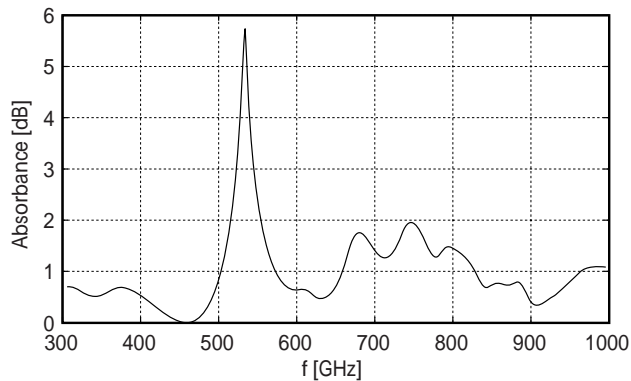
Figure 5.20: Absorption spectrum of the pharmacological compound with commercial denomination *Polaramine Repetabs*.

5.3.5 Tomographic imaging

Several measurements of different scenarios have been performed to test the imaging capabilities of the reconstruction algorithm in the THz frequency range. The difference among different scenarios resides in the type of sample and their disposition in the scene. The samples are based on a Rohacell structure as described Section 5.3.1 and may contain Polaramine depending on the test.

Figure 5.21 shows the image reconstruction of a scenario consisting in a solid cylinder of Rohacell material with 12 mm diameter displaced from the center of rotation. Since the algorithm is based on a cylindrical geometry, it tends to easily reconstruct cylindric shapes at the center of the image, even if the algorithm is not properly implemented in the computer. Therefore, a first test with a sample displaced from the center has been performed in order to validate the implementation of the reconstruction algorithm. The cylinder is retrieved

Figure 5.21: Reconstructed images from the measurements of a Rohacell cylinder of 12mm diameter displaced from the center of rotation. Each image corresponds to a reconstruction of the contrast at a single frequency: (a) 100 GHz, (b) 200 GHz, (c) 300 GHz, (d) 400 GHz, (f) 500 GHz, (g) 600 GHz, (h) 700 GHz, (i) 800 GHz.

properly from frequencies up to 600 GHz. In the following frequencies the SNR of the measurements decreases, being translated to the image as an increment of noise. In addition, the shape of the cylinder tends to be concentrated to the center of the image. This is c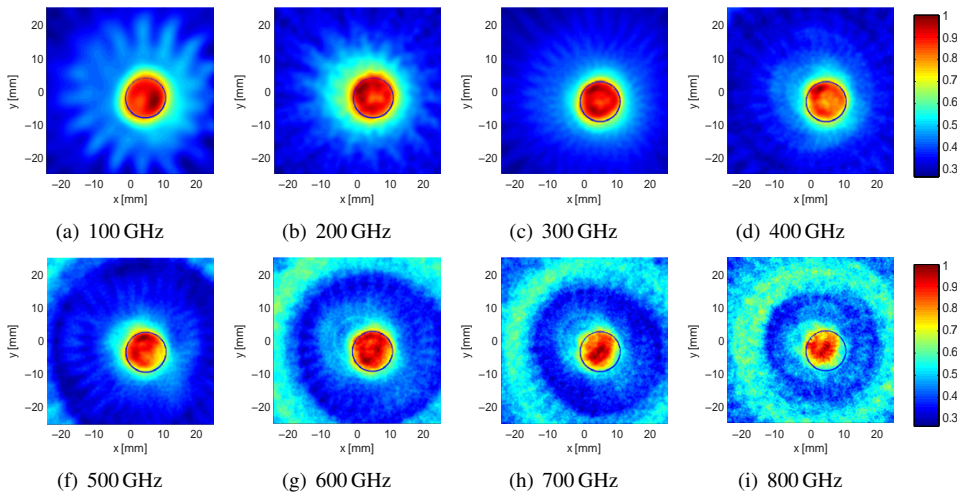aused by the narrowing of both the illumination and reception THz beams as the frequency is increased. At high frequencies the THz beams illuminate the sample partially, and therefore the reconstruction shape does not perfectly match with the original sample.

Additional tests have been performed without including the pharmaceutical compound in the sample. Figure 5.22 shows two reconstruction from different scenarios. In Fig. 5.22(a) a solid Rohacell block with triangular shape, and displaced from the center has been reconstructed. The shape obtained from the measurement does not completely match with the block shape. The main discrepancies occur at the edges that appear rounded instead of sharp. The main cause is the lack of spatial resolution to properly retrieve the edges. Either a higher frequency or a higher span of the reception angle θ should be used to improve the spatial resolution, and hence increase the reconstruction quality of the edges. A Rohacell cylinder of $12\,\mathrm{mm}$ diameter with an empty inner-cylinder of $6\,\mathrm{mm}$ diameter has been measured and the resulting image is shown in Fig. 5.22(b). The center hole is reconstructed with the proper dimensions, confirming the penetration capabilities of the THz radiation in the Rohacell material. Therefore, Rohacell is a proper material to be used as a sample holder to perform the spectroscopic imaging.

The test on spectroscopic imaging has been performed using a centered Rohacell cylinder with $12\,\mathrm{mm}$ diameter and inner-cylinder of $6\,\mathrm{mm}$ filled with Polaramine. Figure 5.23 shows the reconstructed images of the sample. The cylinder is centered at the main rotation axis and therefore it appears centered in the image. The dynamic range of the images is fixed and the results have been normalized by the frequency response of the system, therefore the images
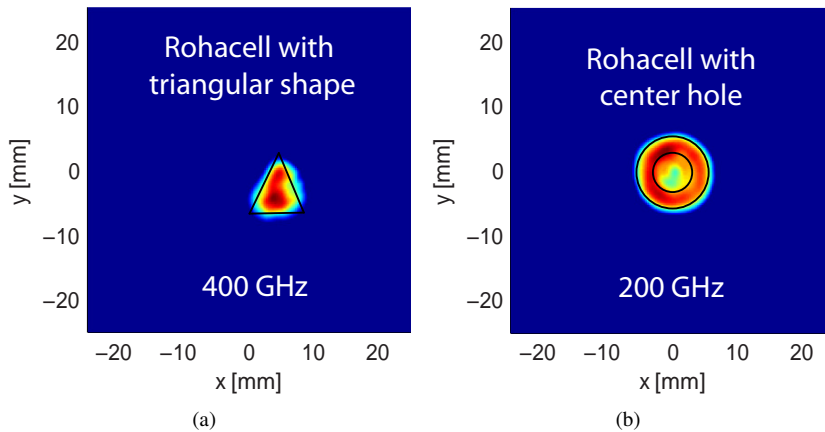
Figure 5.22: (a) Reconstructed image of a Rohacell block with triangular shape; and (b) reconstructed image of a Rohacell cylinder with a hole of 6 mm diameter.

can be compared among them. As in the images appearing in Fig. 5.21, as the frequency increases the level of noise in the images increases as well and reconstruction quality of the cylinder decreases. In general, only the outer shape of the cylinder is reconstructed and the polaramine contrast is not perceived. However in the images of Fig. 5.23(c) and 5.23(h), the contrast is slightly shown as a superposition of two circles. Note that the inner cylinder is not properly centered in the main cylinder, but a slight shifted to the positive x-axis. The main variation in the images appears in Fig. 5.23(f), where an attenuation in the zone of the image where the Polaramine is placed. However the zone corresponding to the Rohacell cylinder is still properly retrieved. It has to be pointed out that due to the slight shift in the frequency calibration of the THz-CW system, the attenuation occurs around 534 GHz instead of 525 GHz as measured with the THz-TDS system and presented in section 5.3.4. This attenuation zone appearing at the frequency where the Polaramine has an absorption line confirms the suitability of the algorithm to perform spectroscopic imaging since it is capable of showing in the image the attenuation of the materials that compose the scene, depending on the frequency.

In order to check the attenuation level produced in the zone, an integration of the retrieved image contrast values in the zone where the Polaramine is placed has been performed. A result of the integration depending on the frequency is shown in Fig. 5.24. A clear absorption peak appears at 534 GHz, however the rest of the plot is not as flat as expected. This effect can be produced by the fact that the scenario does not fulfill the Born condition, since the relative permittivity of the Polaramine is around 2. The results obtained from the Polaramine are compared with the ones obtained from the Rohacell sample shown in Fig. 5.21. The result obtained from the Rohacell presents no significant absorption peaks since the Rohacell does not have an spectral footprint in the studied frequency band. These results reveal that the algorithm is useful when qualitative images are required, and no quantitative information can be obtained since the main assumption of the reconstruction algorithm is not fulfilled. Therefore, no information about concentration of the chemical substance can be obtained. The algorithm is limited to detect and identify the pharmaceutical compound.
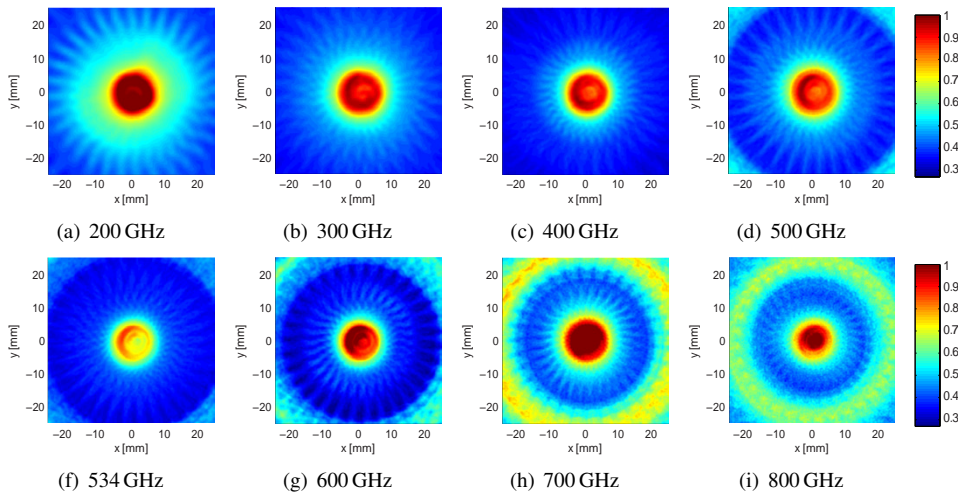
Figure 5.23: Reconstructed images from the measurements of a Rohacell cylinder of 12 mm diameter filled with Polaramine powder covering a diameter of 6 mm. Each image corresponds to a reconstruction of the contrast at a single frequency: (a) 200 GHz, (b) 300 GHz, (c) 400 GHz, (d) 500 GHz, (f) 534 GHz, (g) 600 GHz, (h) 700 GHz, (i) 800 GHz.
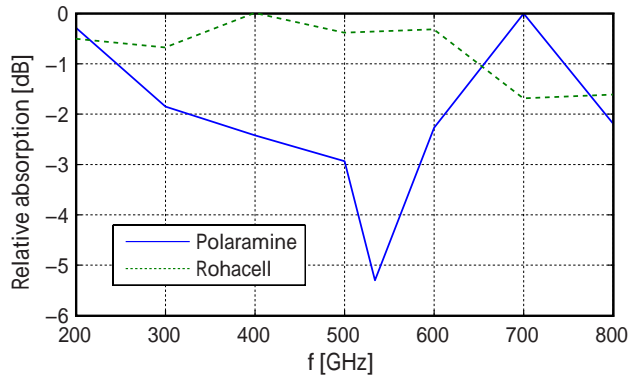
Figure 5.24: The blue curve shows the result of the integration of the image zone where the Polaramine is placed, depending on the frequency. The green curve shows the resulting integration of the zone where the Rohacell is placed from the set of images shown in Fig. 5.21.

5.4   Conclusions

A THz tomographic reconstruction technique has been presented in this chapter. The algorithm required to focus the measured scattered field from the sample has been described, and its suitability for imaging reconstruction at THz frequencies has been assessed. The spectroscopic capabilities of the algorithm have been validated at THz frequencies with a pharmaceutical compound having a molecular absorption resonance at 525 GHz.

A method to acquire complex electric field values with a THz-CW system has been developed. The method is based on modulating the laser current to shift the THz frequency and has been proven to be appropriate to measure the complex field values required to reconstruct the image. Acquisition speeds below $1\,s$ can be easily achieved by using this method. However, a main drawback of the THz-CW has been found consisting of the large phase drift throughout time. A calibration method consisting of acquiring several calibration points and interpolating a phase calibration curve has been required to properly retrieve the images. Each acquisition has been normalized by the phase drift value corresponding to its acquisition time. This method have provided positive results on the image reconstruction since different sample shapes and distributions have been tested and reconstructed successfully.

The spectroscopic capabilities of the algorithm have been validated by performing simulations and measurements. Only qualitative images can be obtained since the Born assumption of the algorithm is not fulfilled in the imaged scenarios. Therefore, the images do not provide information about concentration levels of the different materials and substances in the scene. Nevertheless, the detection and identification capabilities of the algorithm have been assessed yielding proper identification of the spectral footprint of the pharmaceutical compound under test.

Thesis Conclusions

Conclusions and discussion

THIS chapter describes the main contributions of this thesis in the areas of Millimeter-Wave (mmW) passive imaging and terahertz imaging. In addition, the CONSOLIDER project objectives that have been fulfilled thanks to the work presented in this thesis are also stated in the following lines. At the end of the chapter, the guidelines to continue with the work performed in the thesis are given.

6.1 Conclusions

The work presented in this document is related with a research line that pursues two main goals: 1) the development of a mmW camera for real-time acquisition of close-range images; and 2) the development of a terahertz imaging system for detection and identification of chemical compounds.

The author has encountered several problems when addressing the proposed goals. This has lead to a deep research on technology, techniques and methodology in the areas of mmW and terahertz imaging with the aim of solving the mentioned issues. The following list details the concluding remarks extracted in the pathway to the $94\,\mathrm{GHz}$ real-time camera development:

- The several tests performed with a single-receiver mechanically-scanned screener based on a total-power radiometer have provided practical experience to the author, permitting to extract several conclusions:

  1. Despite theoretically is feasible to obtain real-time ($t_s < 1$) images with a single-receiver screener with a proper radiometric resolution, the mechanical complexity that presents the antenna aiming system makes this screener practically unfeasible.

  2. In order to detect concealed objects in low-contrast scenarios, such as indoor environments, a radiometric resolution below $1\,\mathrm{K}$ is required. However, in outdoor

scenarios the reflection of the sky strongly improves the contrast of the scenario, reducing the performance requirements of the screener in terms of radiometric resolution.

3. If the acquisition speed is not important performance parameter of the application, a single-receiver screener is a good choice due to its simplicity and effectiveness.

- In order to decide which is the optimal radiometric geometry for close-range screening, a performance study of three different radiometers (Two-Dimensional Synthetic Aperture (2D-SA), One-Dimensional Synthetic Aperture (1D-SA) and Real-Aperture (RA)) has been performed taking into account the distortion produced by placing the scenario in the near-field distance of the receiver array. The following conclusions can be obtained from the results of the study:

  1. When compared with the same front end parameters, spatial resolution and imaging rate, 2D-SA, 1D-SA and RA radiometric sensitivity is equivalent and not a driver to select one of the options, however off-boresight radiometric resolution degrades as a function of $\xi^2 + \eta^2$ in the synthesized cases.

  2. The optimum performance is achieved when imaging at a fixed range and the Half-Power Beamwidth (HPBW) of each single antenna in the array matches the scene field of view. This condition is always feasible, in a first approach, independently of the imaging geometry and requirements.

  3. Due to the small array size, mmW operation also allows for very large predetection bandwidths and close range configurations to improve radiometric sensitivity while minimizing decorrelation effects and Noise Figure (NFI) distortion.

  4. An sparse 1D-SA radiometer can be used with a moving walkway to perform personnel screening avoiding mechanical movements with an optimum number of mmW receivers.

- From the latter conclusion presented in the previous point it can be extracted that the one-dimensional sparse interferometric radiometer achieves a good tradeoff between radiometric performance and number of receivers for close-range screening purposes. However, the acquisition of multiple correlations of large bandwidth signals required to retrieve the visibilities of the scene represents a major drawback in this radiometer. Hence, a method to overcome the problem of routing and correlating all the antenna signal pairs in an interferometric radiometer by upconverting the Radiofrequency (RF) signal to the optical domain has been developed in this thesis, yielding the following conclusions:

  1. A distribution and correlation of the mmW signals in the optical domain can strongly simplify the processing of the multiple correlations required in a interferometric radiometer.

  2. The method has been tested by performing measurements of several scenarios, confirming the suitability of the method.

  3. The receiver temperature of the system is not critically degraded by converting the signal to the optical domain since the LNA placed at the front-end fixes the noise figure for the whole receiver chain.

   4. For systems with high number of receivers a Single-Sideband (SSB) modulation
      should be used in order to achieve real-time imaging with bandwidths in the order
      of the GHz.

   In the research of a THz tomographic imaging system for chemical compound detection
and identification, a reconstruction algorithm based on a Born approximation has been used.
The following conclusions are extracted from the work performed in this topic:

   1. The cylindrical diffraction tomography algorithm shows the capability of retrieving
      spectral information of the objects appearing in the reconstructed image.

   2. Even though the Terahertz Continuous Wave (THz-CW) system does not provide direct
      complex signal information, amplitude and phase of the signal can be retrieved by
      sweeping the THz signal by modulating the laser current with a ramp.

   3. The images cannot be reconstructed if the phase drift along time of the system is not
      calibrated.

   4. Only qualitative results can be obtained from the images, since the Born approximation
      is not valid for the studied cases.

6.2   Future Research

The following lines describe the work that can be performed as a continuation of the research
presented in this thesis:

   1. Develop the optical distribution part of the optical correlation system in order to vali-
      date the suitability of the method with multiple receivers.

   2. Build an industrial prototype of a close-range screener based on a linear interferometric
      radiometer with the optical cros-correlator method developed in this thesis.

   3. Test the tomographic algorithm by measuring samples containing multiple chemical
      compounds to ensure the suitability of the method.

   4. Design tomographic cylindrical array in order to perform THz spectroscopic imaging
      in real-time using the algorithm described in this document.

Close-Range Millimeter-Wave Passive Images

Several images have been acquired using the Total-Power Radiometer (TPR) described in chapter 2. This appendix includes some of these radiometric images taken from the PhD students of the AntennaLab group of the Signal Theory and Communications Department (TSC) department. The images have been acquired in an outdoor environment with a metallic rear panel that reflects the sky temperature towards the radiometer. This improves the contrast of the person with respect the background. The approximate spatial resolution is around $3\,\mathrm{cm}$ in each axis whereas the radiometric sensitivity of the image is around $2\,\mathrm{K}$.

The images have been taken in different measurement trials and the format does not match among all of them. Figure A.1 shows images with $60\mathrm{x}100\,\mathrm{cm}^2$ dimensions. In those images the body can be seen from the neck to the knees. The upper part of the body reflects the temperature of the sky and is seen as a cold surface whereas the bottom part is seen as a hot surface since reflects the heat from the floor. Figure A.2 presents images with $50\mathrm{x}70\,\mathrm{cm}^2$ dimensions. In this case only the center body is seen with exception of Fig. A.2(b) where the entire head is shown.

(a) Subject S.C. (Male)   (b) Subject M.A. (Female)   (c) Subject E.N. (Male)
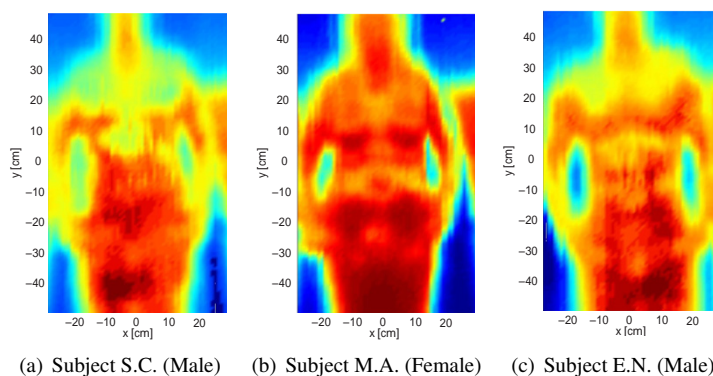
Figure A.1: Outdoor images with $60\mathrm{x}100\,\mathrm{cm}^2$ dimensions.

(a) Subject J.R. (Male)   (b) Subject A.A (Male)   (c) Subject D.R. (Male)

(d) Subject G.R. (Female)   (e) Subject M.I. (Male)
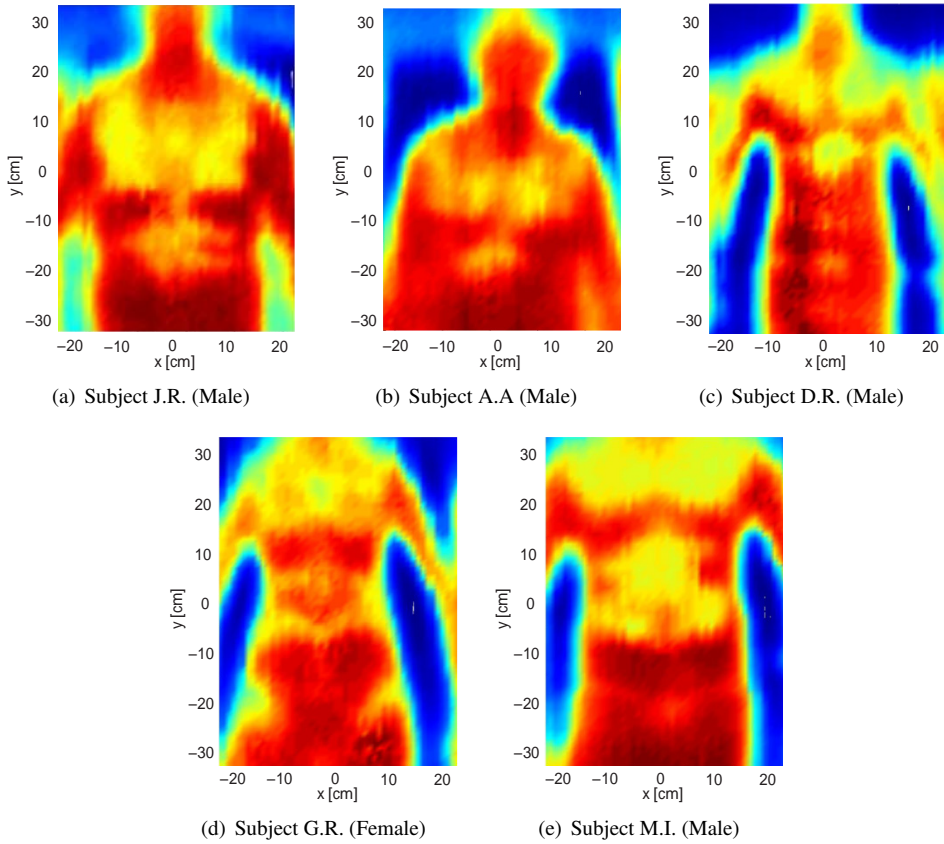
Figure A.2: Outdoor images with $50\text{x}70\,\text{cm}^2$ dimensions.

Acronyms

16QAM	16-state Quadrature Amplitude Modulation
1D-SA	One-Dimensional Synthetic Aperture
2D-SA	Two-Dimensional Synthetic Aperture
ADC	Analog to Digital Converter
ADC	Analog-to-Digital Converter
ALMA	Atacama Large Millimeter/Submillimeter Array
ASK	Amplitude Shift Keying
CMOS	Complementary Metal-Oxide Semiconductor
CMOS	Complementary Metal-Oxide-Semiconductor
CT	Computed Tomography
CW	Continuous Wave
DC	Direct-Current
DFB	Distributed Feedback
DFT	Discrete Fourier Transform
DSB	Double-Sideband
EFoV	Effective Field of View
FEM	Finite Element Method
FF	Far Field
FFT	Fast Fourier Transform
FMCW	Frequency-Modulated Continuous-Wave

FoV	Field of View
FPGA	Field Programmable Gate Array
FT	Fourier Transform
HDTV	High Definition Television
HPBW	Half-Power Beamwidth
iFFT	inverse Fast Fourier Transform
IF	Intermediate Frequency
IFoV	Instantaneous Field of View
iFT	inverse Fourier Transform
JPL	Jet Propulsion Laboratory
LNA	Low-Noise Amplifier
LO	Local Oscillator
MIRAS	Microwave Imaging Radiometer using Aperture Synthesis
MMIC	Monolithic Microwave Integrated Circuit
mmW	Millimeter-Wave
MoM	Method of Moments
NASA	National Aeronautics and Space Administration
NFI	Noise Figure
NF	Near Field
NTT	Nippon Telegraph and Telephone Corporation
PCA	Photoconductive Antenna
PCS	Photoconductive Switch
PID	Proportional-Integral-Derivative
PLO	Phase-Locked Oscillator
PML	Perfect Matched Layer
PO	Physical Optics
PVC	Polyvinyl Chloride
QCL	Quantum Cascaded Laser

RA	Real-Aperture
RF	Radiofrequency
RMS	Root-Mean-Square
SA	Synthetic Aperture
SMOS	Soil Moisture and Ocean Salinity
SNR	Signal to Noise Ratio
SSB	Single-Sideband
THz-CW	Terahertz Continuous Wave
THz-TDS	Terahertz Time-Domain Spectroscopy
TIA	Transimpedance Amplifier
TPR	Total-Power Radiometer
TSC	Signal Theory and Communications Department
UPC	Polytechnic University of Catalonia
USB	Universal Serial Bus
UTC-PD	Uni-travelling Carrier Photodiode
VNA	Vectorial Network Analyzer
WLAN	Wireless Local Area Network
WPAN	Wireless Personal Area Network

Bibliography

[1] C. Park and T. Rappaport, "Short-Range Wireless Communications for Next-Generation Networks: UWB, 60 GHz Millimeter-Wave WPAN, And ZigBee," *Wireless Communications, IEEE*, vol. 14, no. 4, pp. 70 –78, august 2007.

[2] R. Ott and J. Thompson, M., "Characteristics of a radio link in the 55 to 65 GHz range," *Antennas and Propagation, IEEE Transactions on*, vol. 24, no. 6, pp. 873 – 877, nov 1976.

[3] H. Ito, T. Furuta, T. Ito, Y. Muramoto, K. Tsuzuki, K. Yoshino, and T. Ishibashi, "W-band uni-travelling-carrier photodiode module for high-power photonic millimetre-wave generation," *Electronics Letters*, vol. 38, no. 22, pp. 1376 – 1377, oct 2002.

[4] A. Hirata, M. Harada, and T. Nagatsuma, "120-GHz wireless link using photonic techniques for generation, modulation, and emission of millimeter-wave signals," *Lightwave Technology, Journal of*, vol. 21, no. 10, pp. 2145 – 2153, oct. 2003.

[5] M. Russell, A. Crain, A. Curran, R. Campbell, C. Drubin, and W. Miccioli, "Millimeter-wave radar sensor for automotive intelligent cruise control (icc)," *Microwave Theory and Techniques, IEEE Transactions on*, vol. 45, no. 12, pp. 2444 –2453, dec 1997.

[6] J. Hasch, E. Topak, R. Schnabel, T. Zwick, R. Weigel, and C. Waldschmidt, "Millimeter-wave technology for automotive radar sensors in the 77 GHz frequency band," *Microwave Theory and Techniques, IEEE Transactions on*, vol. 60, no. 3, pp. 845 –860, march 2012.

[7] J. Lee, Y.-A. Li, M.-H. Hung, and S.-J. Huang, "A fully-integrated 77-GHz fmcw radar transceiver in 65-nm cmos technology," *Solid-State Circuits, IEEE Journal of*, vol. 45, no. 12, pp. 2746 –2756, dec. 2010.

[8] D. Sheen, D. McMakin, and T. Hall, "Three-dimensional millimeter-wave imaging for concealed weapon detection," *Microwave Theory and Techniques, IEEE Transactions on*, vol. 49, no. 9, pp. 1581 –1592, sep 2001.

[9] A. Pazmany, R. McIntosh, R. Kelly, and G. Vali, "An airborne 95 GHz dual-polarized radar for cloud studies," *Geoscience and Remote Sensing, IEEE Transactions on*, vol. 32, no. 4, pp. 731 –739, jul 1994.

[10] J. Mead, A. Pazmany, S. Sekelsky, and R. McIntosh, "Millimeter-wave radars for remotely sensing clouds and precipitation," *Proceedings of the IEEE*, vol. 82, no. 12, pp. 1891 –1906, dec 1994.

[11] A. Wootten and A. Thompson, "The atacama large millimeter/submillimeter array," *Proceedings of the IEEE*, vol. 97, no. 8, pp. 1463 –1471, aug. 2009.

[12] H. Rudolf, M. Carter, and A. Baryshev, "The alma front end optics-system aspects and european measurement results," *Antennas and Propagation, IEEE Transactions on*, vol. 55, no. 11, pp. 2966 –2973, nov. 2007.

[13] D. Doyle, G. Pilbratt, and J. Tauber, "The Herschel and Planck space telescopes," *Proceedings of the IEEE*, vol. 97, no. 8, pp. 1403 –1411, aug. 2009.

[14] D. Cimini, E. Westwater, and A. Gasiewski, "Temperature and humidity profiling in the arctic using ground-based millimeter-wave radiometry and 1DVAR," *Geoscience and Remote Sensing, IEEE Transactions on*, vol. 48, no. 3, pp. 1381 –1388, march 2010.

[15] D. G. Mackrides, C. A. Schuetz, R. D. Martin, T. E. Dillon, P. Yao, and D. W. Prather, "Progress toward a video-rate, passive millimeter-wave imager for brownout mitigation," vol. 8022, no. 1, p. 802203, 2011.

[16] C. Mann, "A compact real time passive terahertz imager," R. Appleby and D. A. Wikner, Eds., vol. 6211, no. 1.   SPIE, 2006, p. 62110E.

[17] R. N. Anderton, R. Appleby, J. E. Beale, P. R. Coward, and S. Price, "Security scanning at 94GHz," R. Appleby and D. A. Wikner, Eds., vol. 6211, no. 1.   SPIE, 2006, p. 62110C.

[18] C. A. Martin and V. G. Kolinko, "Concealed weapons detection with an improved passive millimeter-wave imager," R. Trebits, J. L. Kurtz, R. Appleby, N. A. Salmon, and D. A. Wikner, Eds., vol. 5410, no. 1.   SPIE, 2004, pp. 252–259.

[19] D. M. Sheen, D. L. McMakin, and T. E. Hall, "Combined illumination cylindrical millimeter-wave imaging technique for concealed weapon detection," R. M. Smith and R. Appleby, Eds., vol. 4032, no. 1.   SPIE, 2000, pp. 52–60.

[20] P. Corredoura, Z. Baharav, B. Taber, and G. Lee, "Millimeter-wave imaging system for personnel screening: scanning 10^7 points a second and using no moving parts," R. Appleby and D. A. Wikner, Eds., vol. 6211, no. 1.   SPIE, 2006, p. 62110B.

[21] G. Chattopadhyay, E. Schlecht, J. Ward, J. Gill, H. Javadi, F. Maiwald, and I. Mehdi, "An all-solid-state broad-band frequency multiplier chain at 1500 GHz," *Microwave Theory and Techniques, IEEE Transactions on*, vol. 52, no. 5, pp. 1538 – 1547, may 2004.

[22] R. Yano, H. Gotoh, Y. Hirayama, S. Miyashita, Y. Kadoya, and T. Hattori, "Terahertz wave detection performance of photoconductive antennas: Role of antenna structure and gate pulse intensity," *Journal of Applied Physics*, vol. 97, no. 10, pp. 103 103 –103 103–6, may 2005.

[23] M. van Exter, C. Fattinger, and D. Grischkowsky, "Terahertz time-domain spectroscopy of water vapor," *Opt. Lett.*, vol. 14, no. 20, pp. 1128–1130, Oct 1989.

[24] J. Y. Suen, W. Li, Z. D. Taylor, and E. R. Brown, "Characterization and modeling of a terahertz photoconductive switch," *Applied Physics Letters*, vol. 96, no. 14, pp. 141 103 –141 103–3, apr 2010.

[25] Z. Ma, H. Ma, C. Yang, and K. Feng, "Modeling of terahertz pulse generation from lt-gaas ultrafast photoconductive switches," *Systems Engineering and Electronics, Journal of*, vol. 22, no. 3, pp. 373 –380, june 2011.

[26] B. S. Williams, S. Kumar, H. Callebaut, Q. Hu, and J. L. Reno, "Terahertz quantum-cascade laser at $\lambda \approx 100\,\mu m$ using metal waveguide for mode confinement," *Applied Physics Letters*, vol. 83, no. 11, pp. 2124 –2126, sep 2003.

[27] I. Hosako, N. Sekine, M. Patrashin, S. Saito, K. Fukunaga, Y. Kasai, P. Baron, T. Seta, J. Mendrok, S. Ochiai, and H. Yasuda, "At the dawn of a new era in terahertz technology," vol. 95, no. 8, pp. 1611–1623, 2007.

[28] R. Piesiewicz, T. Kleine-Ostmann, N. Krumbholz, D. Mittleman, M. Koch, J. Schoebel, and T. Kurner, "Short-range ultra-broadband terahertz communications: Concepts and perspectives," *Antennas and Propagation Magazine, IEEE*, vol. 49, no. 6, pp. 24 –39, dec. 2007.

[29] H.-J. Song and T. Nagatsuma, "Present and future of terahertz communications," *Terahertz Science and Technology, IEEE Transactions on*, vol. 1, no. 1, pp. 256 –263, sept. 2011.

[30] P. Goldsmith and D. Lis, "Early science results from the heterodyne instrument for the far infrared (HIFI) on the Herschel space observatory," *Terahertz Science and Technology, IEEE Transactions on*, vol. 2, no. 4, pp. 383 –392, july 2012.

[31] L. Rolo, M. Paquay, R. Daddato, J. Parian, D. Doyle, and P. de Maagt, "Terahertz antenna technology and verification: Herschel and Planck - a review," *Microwave Theory and Techniques, IEEE Transactions on*, vol. 58, no. 7, pp. 2046 –2063, july 2010.

[32] K. Cooper, R. Dengler, N. Llombart, T. Bryllert, G. Chattopadhyay, E. Schlecht, J. Gill, C. Lee, A. Skalare, I. Mehdi, and P. Siegel, "Penetrating 3-d imaging at 4- and 25-m range using a submillimeter-wave radar," *Microwave Theory and Techniques, IEEE Transactions on*, vol. 56, no. 12, pp. 2771 –2778, dec. 2008.

[33] N. Llombart, R. J. Dengler, and K. B. Cooper, "Terahertz antenna system for a near-video-rate radar imager [antenna applications]," vol. 52, no. 5, pp. 251–259, 2010.

[34] H. bo Liu, H. Zhong, N. Karpowicz, Y. Chen, and X.-C. Zhang, "Terahertz spectroscopy and imaging for defense and security applications," *Proceedings of the IEEE*, vol. 95, no. 8, pp. 1514 –1527, aug. 2007.

[35] P. Bolivar, M. Brucherseifer, J. Rivas, R. Gonzalo, I. Ederra, A. Reynolds, M. Holker, and P. de Maagt, "Measurement of the dielectric constant and loss tangent of high dielectric-constant materials at terahertz frequencies," *Microwave Theory and Techniques, IEEE Transactions on*, vol. 51, no. 4, pp. 1062 – 1066, apr 2003.

[36] R. Al Hadi, H. Sherry, J. Grzyb, N. Baktash, Y. Zhao, E. Ojefors, A. Kaiser, A. Cathelin, and U. Pfeiffer, "A broadband 0.6 to 1 THz cmos imaging detector with an integrated lens," in *Microwave Symposium Digest (MTT), 2011 IEEE MTT-S International*, june 2011, pp. 1 –4.

[37] H. Sherry, J. Grzyb, Y. Zhao, R. Al Hadi, A. Cathelin, A. Kaiser, and U. Pfeiffer, "A 1kpixel cmos camera chip for 25fps real-time terahertz imaging applications," in *Solid-State Circuits Conference Digest of Technical Papers (ISSCC), 2012 IEEE International*, feb. 2012, pp. 252 –254.

[38] R. Al Hadi, H. Sherry, J. Grzyb, Y. Zhao, W. Forster, H. M. Keller, A. Cathelin, A. Kaiser, and U. R. Pfeiffer, "A 1 k-pixel video camera for 0.7–1.1 terahertz imaging applications in 65-nm cmos," *Solid-State Circuits, IEEE Journal of*, vol. 47, no. 12, pp. 2999 –3012, dec. 2012.

[39] H.-T. Chen, R. Kersting, and G. C. Cho, "Terahertz imaging with nanometer resolution," *Applied Physics Letters*, vol. 83, no. 15, pp. 3009 –3011, oct 2003.

[40] Y. chun Shen and P. Taday, "Development and application of terahertz pulsed imaging for nondestructive inspection of pharmaceutical tablet," *Selected Topics in Quantum Electronics, IEEE Journal of*, vol. 14, no. 2, pp. 407 –415, march-april 2008.

[41] Y. Hua and H. Zhang, "Qualitative and quantitative detection of pesticides with terahertz timedomain spectroscopy," *Microwave Theory and Techniques, IEEE Transactions on*, vol. 58, no. 7, pp. 2064 –2070, july 2010.

[42] J. Bolomey, A. Izadnegahdar, L. Jofre, C. Pichot, G. Peronnet, and M. Solaimani, "Microwave diffraction tomography for biomedical applications," *Microwave Theory and Techniques, IEEE Transactions on*, vol. 30, no. 11, pp. 1998 –2000, nov. 1982.

[43] R. Lewitt and S. Matej, "Overview of methods for image reconstruction from projections in emission computed tomography," *Proceedings of the IEEE*, vol. 91, no. 10, pp. 1588 – 1611, oct. 2003.

[44] T.-H. Chu and K.-Y. Lee, "Wide-band microwave diffraction tomography under born approximation," *Antennas and Propagation, IEEE Transactions on*, vol. 37, no. 4, pp. 515 –519, apr 1989.

[45] M. Soumekh, "An improvement to the rytov approximation in diffraction tomography," *Ultrasonics, Ferroelectrics and Frequency Control, IEEE Transactions on*, vol. 33, no. 4, pp. 394 –401, july 1986.

[46] Y. C. Shen, T. Lo, P. F. Taday, B. E. Cole, W. R. Tribe, and M. C. Kemp, "Detection and identification of explosives using terahertz pulsed spectroscopic imaging," *Applied Physics Letters*, vol. 86, no. 24, pp. 241 116 –241 116–3, jun 2005.

[47] K. Ajito, H.-J. Song, A. Hirata, A. Wakatsuki, Y. Muramoto, N. Shigekawa, T. Kumashiro, D. Asa, T. Nagatsuma, N. Kukutsu, and Y. Kado, "Continuous-wave terahertz spectroscopic imaging at over 1 THz for pharmaceutical applications," in *Infrared Millimeter and Terahertz Waves (IRMMW-THz), 2010 35th International Conference on*, sept. 2010, pp. 1 –2.

[48] Y. Kerr, P. Waldteufel, J.-P. Wigneron, S. Delwart, F. Cabot, J. Boutin, M.-J. Escorihuela, J. Font, N. Reul, C. Gruhier, S. Juglea, M. Drinkwater, A. Hahne, M. Martín-Neira, and S. Mecklenburg, "The SMOS Mission: New Tool for Monitoring Key Elements of the Global Water Cycle," *Proceedings of the IEEE*, vol. 98, no. 5, pp. 666 –687, May 2010.

[49] R. Miles, X. Zhang, H. Eisele, and A. Krotkus, *Terahertz Frequency Detection and Identification of Materials and Objects*, ser. NATO security through science series. B, Physics and biophysics. Springer, 2007.

[50] R. H. Dicke, "The Measurement of Thermal Radiation at Microwave Frequencies," *Review of Scientific Instruments*, vol. 17, no. 7, pp. 268–275, 1946.

[51] R. Meredith, F. L. Warner, Q. V. Davis, and J. L. Clarke, "Superheterodyne radiometers for short millimetre wavelengths," *Proceedings of the Institution of Electrical Engineers*, vol. 111, no. 2, pp. 241–256, 1964.

[52] E. J. Wollack and M. W. Pospieszalski, "Characteristics of broadband InP millimeter-wave amplifiers for radiometry," in *Proc. IEEE MTT-S Int. Microwave Symp. Digest*, vol. 2, 1998, pp. 669–672.

[53] B. Kane, S. Weinreb, E. Fischer, and N. Byer, "High-sensitivity W-band MMIC radiometer modules," in *Proc. Microwave and Millimeter-Wave Monolithic Circuits Symp. Digest of Papers. IEEE 1995*, 1995, pp. 59–62.

[54] I. Corbella, N. Duffo, M. Vall-llossera, A. Camps, and F. Torres, "The visibility function in interferometric aperture synthesis radiometry," *Geoscience and Remote Sensing, IEEE Transactions on*, vol. 42, no. 8, pp. 1677 – 1682, aug. 2004.

[55] P. Moreno-Galbis, J. Kainulainen, and M. Martin-Neira, "Experimental demonstration of the corbella equation for aperture synthesis microwave radiometry," *Geoscience and Remote Sensing, IEEE Transactions on*, vol. 45, no. 4, pp. 945 –957, april 2007.

[56] A. Camps, J. Bará, F. Torres, and I. Corbella, "Extension of the clean technique to the microwave imaging of continuous thermal sources by means of aperture synthesis radiometers," *Progress In Electromagnetics Research*, vol. 18, pp. 67–83, 1998.

[57] C. Ruf, C. Swift, A. Tanner, and D. Le Vine, "Interferometric synthetic aperture microwave radiometry for the remote sensing of the earth," *Geoscience and Remote Sensing, IEEE Transactions on*, vol. 26, no. 5, pp. 597 –611, sep 1988.

[58] M. Peichl, H. Suess, M. Suess, and S. Kern, "Microwave imaging of the brightness temperature distribution of extended areas in the near and far field using two-dimensional aperture synthesis with high spatial resolution," *Radio Science*, vol. 33, no. 3, pp. 791–801, 1998.

[59] C. A. Balanis, *Antenna Theory: Analysis and Design*. Wiley-Interscience, 2005.

[60] A. Thompson, J. Moran, and J. George W. Swenson, *Interferometry and Synthesis in Radio Astronomy*. John Wiley & Sons, 2008.

[61] A. Camps, I. Corbella, J. Bará, and F. Torres, "Radiometric sensitivity computation in aperture synthesis interferometric radiometry," *Geoscience and Remote Sensing, IEEE Transactions on*, no. 2, mar 1998.

[62] I. Corbella, F. Torres, N. Duffo, V. González-Gambau, M. Pablos, I. Duran, and M. Martín-Neira, "MIRAS Calibration and Performance: Results From the SMOS In-Orbit Commissioning Phase," *Geoscience and Remote Sensing, IEEE Transactions on*, vol. PP, no. 99, pp. 1 –9, 2011.

[63] C. A. Balanis, *Advanced engineering electromagnetics*.   John Wiley & Sons, 1989.

[64] A. Tanner, B. Lambrigsten, T. Gaier, and F. Torres, "Near field characterization of the GeoSTAR demonstrator," in *Proc. IEEE Int. Conf. Geoscience and Remote Sensing Symp. IGARSS 2006*, 2006, pp. 2529–2532.

[65] F. Torres, J. Abril, E. Nova, A. Broquetas, and L. Jofre, "Far field condition in passive interferometry for security screening applications," in *Antennas and Propagation (EuCAP), 2010 Proceedings of the Fourth European Conference on*, april 2010, pp. 1 –4.

[66] D. M. Le Vine, "The sensitivity of synthetic aperture radiometers for remote sensing applications from space," *RADIO SCIENCE*, vol. 25, no. 4, pp. 441–453, 1990.

[67] A. Camps, A. Cardama, and D. Infantes, "Synthesis of large low-redundancy linear arrays," *Antennas and Propagation, IEEE Transactions on*, vol. 49, no. 12, pp. 1881 –1883, dec 2001.

[68] S. Weinreb, *A Digital Spectral Analysis Technique and Its Application to Radio Astronomy*, ser. Massachusetts Institute of Technology. Research Laboratory of Electronics. Technical report 412. Massachusetts Institute of Technology, Research Laboratory of Electronics, 1963.

[69] S. Padin, T. Clark, M. Ewing, R. Finch, R. Lawrence, J. Navarro, S. Scott, N. Scoville, C. Seelinger, and T. Seling, "A high-speed digital correlator for radio astronomy," *Instrumentation and Measurement, IEEE Transactions on*, vol. 42, no. 4, pp. 793 –798, aug 1993.

[70] E. Wooten, K. Kissa, A. Yi-Yan, E. Murphy, D. Lafaw, P. Hallemeier, D. Maack, D. Attanasio, D. Fritz, G. McBrien, and D. Bossi, "A review of lithium niobate modulators for fiber-optic communications systems," *Selected Topics in Quantum Electronics, IEEE Journal of*, vol. 6, no. 1, pp. 69 –82, jan/feb 2000.

[71] S. Kaneko, M. Noda, Y. Miyazaki, H. Watanabe, K. Kasahara, and T. Tajime, "An electroabsorption modulator module for digital and analog applications," *Lightwave Technology, Journal of*, vol. 17, no. 4, pp. 669 –676, apr 1999.

[72] S. Kobayashi, Y. Yamamoto, M. Ito, and T. Kimura, "Direct frequency modulation in algaas semiconductor lasers," *Quantum Electronics, IEEE Journal of*, vol. 18, no. 4, pp. 582 – 595, apr 1982.

[73] G. Li and P. Yu, "Optical intensity modulators for digital and analog applications," *Lightwave Technology, Journal of*, vol. 21, no. 9, pp. 2010 – 2030, sept. 2003.

[74] N. Abramson, "Bandwidth and spectra of phase-and-frequency-modulated waves," *Communications Systems, IEEE Transactions on*, vol. 11, no. 4, pp. 407 –414, december 1963.

[75] D. Middleton, I. C. Society, and I. I. T. Society, *An introduction to statistical communication theory: David Middleton ; IEEE Communications Society, sponsor, IEEE Information Theory Society, sponsor*.   IEEE Press, 1996.

[76] S. Shimotsu, S. Oikawa, T. Saitou, N. Mitsugi, K. Kubodera, T. Kawanishi, and M. Izutsu, "Single side-band modulation performance of a LiNbO3 integrated modulator consisting of four-phase modulator waveguides," *Photonics Technology Letters, IEEE*, vol. 13, no. 4, pp. 364 –366, april 2001.

[77] M. Ryle, "A new radio interferometer and its application to the observation of weak radio stars," *Proceedings of the Royal Society of London. Series A. Mathematical and Physical Sciences*, vol. 211, no. 1106, pp. 351–375, 1952.

[78] J. Macario, P. Yao, R. Shireen, C. Schuetz, S. Shi, and D. Prather, "Development of electro-optic phase modulator for 94 GHz imaging system," *Lightwave Technology, Journal of*, vol. 27, no. 24, pp. 5698 –5703, dec.15, 2009.

[79] M. Lipson, "Guiding, modulating, and emitting light on silicon-challenges and opportunities," *Lightwave Technology, Journal of*, vol. 23, no. 12, pp. 4222 – 4238, dec. 2005.

[80] R. Soref, "The past, present, and future of silicon photonics," *Selected Topics in Quantum Electronics, IEEE Journal of*, vol. 12, no. 6, pp. 1678 –1687, nov.-dec. 2006.

[81] O. Batz, U. Kraft, W. Lindemer, and H. Reichel, "Design and implementation of the miras digital correlator," in *Geoscience and Remote Sensing Symposium, 1996. IGARSS '96. 'Remote Sensing for a Sustainable Future.', International*, vol. 2, may 1996, pp. 872 –874 vol.2.

[82] A. Baudry and J. Webber, "The alma 64-antenna correlator: Main technical features and science modes," in *General Assembly and Scientific Symposium, 2011 XXXth URSI*, aug. 2011, pp. 1 –4.

[83] M. Born and P. Jordan, "Zur quantenmechanik," *European Physical Journal*, vol. 34, no. 1, pp. 858–888, 1925.

[84] A. T. de Hoop, "A reciprocity theorem for the electromagnetic field scattered by an obstacle," *Applied Scientific Research, Section B*, vol. 8, no. 1, pp. 135–140, 1960.

[85] *COMSOL Multiphysics - RF Module User's Guide*, v. 4.3 ed.

[86] S. Verghese, K. A. McIntosh, S. Calawa, W. F. DiNatale, E. Duerr, and K. A. Molvar, "Generation and detection of coherent terahertz waves using two photomixers," *Applied Physics Letters*, vol. 73, no. 26, pp. 3824–3826, 1998.

[87] S. Saito, T. M. Inerbaev, H. Mizuseki, N. Igarashi, R. Note, and Y. Kawazoe, "First principles calculation of terahertz vibrational modes of a disaccharide monohydrate crystal of lactose," *Japanese Journal of Applied Physics*, vol. 45, no. 43, pp. L1156–L1158, 2006.

Author Publications and Patents

Journal articles

[J1] **Nova, E.**, J. Romeu, S. Capdevila, F. Torres, and L. Jofre, "Optical Signal Processor for Millimeter Wave Interferometric Radiometry," *Geoscience and Remote Sensing, IEEE Transactions on*, vol. In press.

[J2] **Nova, E.**, J. Romeu, F. Torres, M. Pablos, J. Riera, A. Broquetas, and L. Jofre, "Radiometric and Spatial Resolution Constraints in Millimeter-Wave Close-Range Passive Screener Systems," *Geoscience and Remote Sensing, IEEE Transactions on*, vol. 51, no. 4, pp. 2327–2336, 2013.

Conference articles

[C1] **Nova, E.**, G. Roqueta, J. Romeu, and L. Jofre, "Characterization of Pharmaceuticals using Terahertz Time Domain Spectral-Tomography," in *Antennas and Propagation (EUCAP), 2013 7th European Conference on*, 2013.

[C2] **Nova, E.**, D. Rodrigo, J. Romeu, and L. Jofre, "94 GHz cassegrain reflector antenna performance characterization," in *Antennas and Propagation (EUCAP), 2012 6th European Conference on*, march 2012, pp. 3442 –3445.

[C3] **Nova, E.**, J. Romeu, F. Torres, A. Broquetas, and L. Jofre, "Optical Cross-Correlation of Millimeter Wave Signals Applied to Interferometric Radiometry," in *Infrared, Millimeter and Terahertz Waves (IRMMW-THz), 2012 37th International Conference on*, 2012.

[C4] **Nova, E.**, J. Romeu, A. Broquetas, F. Torres, and L. Jofre, "Optical Cross-Correlation of W-band Radiometric Signals," in *XXVII Simposium Nacional de la Unión Científca Internacional de Radio (URSI 2012)*, 2012.

[C5] M. Alonso, C. Guerra, **Nova, E.**, J. Abril, J. Romeu, N. Llombart, and L. Jofre, "100 GHz retina for THz tomographic imaging," in *Infrared, Millimeter and Terahertz Waves (IRMMW-THz), 2011 36th International Conference on*, oct. 2011, pp. 1 –2.

[C6] **Nova, E.**, J. Abril, J. Romeu, A. Broquetas, F. Torres, and L. Jofre, "Characterization of a 94 GHz radiometric imager with mechanical beam-scanning," in *Microwave Workshop Series on Millimeter Wave Integration Technologies (IMWS), 2011 IEEE MTT-S International*, sept. 2011, pp. 164 –167.

[C7] J. Abril, **Nova, E.**, A. Broquetas, A. Aguasca, J. Romeu, and L. Jofre, "Deforming and relief interferometric sar imaging at W-band," in *Infrared, Millimeter and Terahertz Waves (IRMMW-THz), 2011 36th International Conference on*, oct. 2011, pp. 1 –2.

[C8] **Nova, E.**, J. Abril, J. Romeu, A. Broquetas, F. Torres, and L. Jofre, "Imaging performance of a 94 GHz radiometer," in *XXVI Simposium Nacional de la Unión Científca Internacional de Radio (URSI 2011)*, 2011.

[C9] J. Abril, **Nova, E.**, A. Broquetas, A. Aguasca, J. Romeu, and L. Jofre, "Micrometric Deformation Imaging Assessement for W-band FMCW Radar," in *XXVI Simposium Nacional de la Unión Científca Internacional de Radio (URSI 2011)*, 2011.

[C10] J. Abril, **Nova, E.**, A. Broquetas, A. Aguasca, J. Romeu, and L. Jofre, "Micrometric deformation imaging at W-band," in *Microwave Workshop Series on Millimeter Wave Integration Technologies (IMWS), 2011 IEEE MTT-S International*, 2011.

[C11] L. Jofre, J. Romeu, S. Capdevila, J. Abril, **Nova, E.**, and M. Alonso, "The challenging world of Terahertz radiation and imaging," in *Antennas and Propagation (EUCAP), Proceedings of the 5th European Conference on*, april 2011, pp. 3470 –3475.

[C12] **Nova, E.**, J. Abril, J. Romeu, A. Broquetas, F. Torres, and L. Jofre, "W-band radiometric imager with mechanical beam-scanning," in *Infrared, Millimeter and Terahertz Waves (IRMMW-THz), 2011 36th International Conference on*, oct. 2011, pp. 1 –2.

[C13] **Nova, E.**, J. Abril, A. Broquetas, F. Torres, J. Romeu, and L. Jofre, "94 GHz short-range passive imaging systems," in *XXV Simposium Nacional de la Unión Científca Internacional de Radio (URSI 2010)*, 2010.

[C14] J. Abril, **Nova, E.**, S. Capdevila, A. Broquetas, F. Torres, and L. Jofre, "Active and passive THz systems for short-range imaging applications," in *Proc. Fourth European Conf. Antennas and Propagation (EuCAP)*, 2010, pp. 1–4.

[C15] J. Abril, **Nova, E.**, A. Broquetas, J. Romeu, L. Jofre, G. Pérez, J. A. Encinar, M. Barba, D. Sánchez, and M. Ferrando, "Active Short-Range Imaging Systems Working at 94 GHz," in *XXV Simposium Nacional de la Unión Científca Internacional de Radio (URSI 2010)*, 2010.

[C16] J. Abril, **Nova, E.**, A. Broquetas, F. Torres, J. Romeu, and L. Jofre, "Combined passive and active millimeter-wave imaging system for concealed objects detection," in *Proc. 35th Int Infrared Millimeter and Terahertz Waves (IRMMW-THz) Conf*, 2010, pp. 1–2.

[C17] F. Torres, J. Abril, **Nova, E.**, A. Broquetas, and L. Jofre, "Far field condition in passive interferometry for security screening applications," in *Proc. Fourth European Conf. Antennas and Propagation (EuCAP)*, 2010, pp. 1–4.

[C18] J. Abril, **Nova, E.**, A. Broquetas, A. Aguasca, J. Romeu, B. Jofre, L. Mencía, J. Grajal, J. P. Pascual, T. Fernández, and A. Tazón, "mmW FM-CW Ground-based SAR," in *XXV Simposium Nacional de la Unión Científca Internacional de Radio (URSI 2010)*, 2010.

[C19] **Nova, E.**, J. Abril, A. Broquetas, J. Romeu, and L. Jofre, "Terahertz Spectroscopic Material Characterization and Imaging," in *XXV Simposium Nacional de la Unión Científca Internacional de Radio (URSI 2010)*, 2010.

[C20] **Nova, E.**, J. Abril, M. Guardiola, S. Capdevila, A. Broquetas, J. Romeu, and L. Jofre, "Terahertz subsurface imaging system," in *Proc. Fourth European Conf. Antennas and Propagation (EuCAP)*, 2010, pp. 1–5.

[C21] **Nova, E.**, J. Abril, M. Guardiola, S. Capdevila, A. Broquetas, J. Romeu, and L. Jofre, "Terahertz tomographic imaging technologies," in *XXIV Simposium Nacional de la Unión Científca Internacional de Radio (URSI 2009)*, 2009.

Patents

[P1] **Nova, E.** and J. Romeu, "Correlador para múltiples receptores de señal de radiofrecuencia implementado con tecnología óptica," Spanish application Patent P201 231 599, 2012.

[P2] J. Encinar, G. Pérez, M. Barba, X. Quintana, M. Geday, J. Otón, A. Broquetas, J. Abril, and **Nova, E.**, "Antena reflectarray de haz reconfigurable basada en celdas multi-capa de cristal líquido," International application Patent PCT/ES2011/000 350, 2010.